Multi-physical modeling of thermographic inspection methods and fast imaging

Almpion Ratsakou

Thèse de doctorat

NNT : 2020UPASS002

université PARIS-SACLAY

Multi-physical modeling of thermographic inspection methods and fast imaging

Thèse de doctorat de l'université Paris-Saclay

École doctorale n°580, Sciences et Technologies de l'Information et de la Communication (STIC)
Spécialité de doctorat : Traitement du Signal et des Images
Unité de recherche : Université Paris-Saclay, CEA, Département Imagerie et Simulation pour le Contrôle, 91191, Gif-sur-Yvette, France
Référent : Faculté des sciences d'Orsay

Thèse présentée et soutenue à Gif-sur-Yvette, le 8 Janvier 2020, par

Almpion RATSAKOU

Composition du Jury

Jean-Christophe BATSALE Professeur, Arts et Métiers Paris Tech Bordeaux	Président & Rapporteur
Theodoros THEODOULIDIS Professeur, University of Western Macedonia	Rapporteur & Examinateur
Marc LAMBERT Chargé de Recherche, CNRS	Examinateur
Shejuan XIE Professeure associée, Xi'an Jiaotong University	Examinatrice
Anastasios SKARLATOS Ingénieur de recherche, CEA LIST	Examinateur
Dominique LESSELIER Directeur de recherche Emérite, CNRS	Directeur de thèse

Dedicated to my family.

Résumé

Le contrôle et l'évaluation non destructifs (CND) est un ensemble de techniques utilisées pour évaluer les propriétés d'un matériau sans modifier les propriétés d'origine ni lui causer de dommages. Les techniques d'essais non destructifs offrent un moyen rentable de tester un échantillon pour détecter les dommages pendant la production et après celle-ci.

Parmi les nombreuses méthodes existantes, le contrôle non destructif thermique ou infrarouge (T/INDT) est l'une des plus prometteuses pour l'inspection des matériaux et des structures. La détection des irrégularités est basée sur le principe que tous les corps émettent un rayonnement infrarouge. Ce rayonnement infrarouge émis peut être mesuré par des caméras infrarouges et les images analysées pour la détection et la caractérisation des défauts. Les irrégularités du matériau affectent le taux de diffusion de la chaleur, ce qui entraîne un contraste thermique à la surface de la pièce homogène. En analysant les altérations ou le contraste de la configuration thermique à la surface du matériau, on peut obtenir des informations sur les défauts enfouis. Outre la modélisation de l'évolution de la distribution de la température à l'intérieur de la pièce testée, la modélisation d'appareils de mesure tels que les caméras thermiques d'imagerie devrait être nécessaire, impliquant des concepts supplémentaires de rayonnement infrarouge.

Selon la présence ou l'absence d'une source d'excitation thermique, la technique est généralement divisée en deux ensembles principaux, passifs et actifs, respectivement. La thermographie active, qui est objet d'investigation ici, utilise une source thermique pour déposer de la chaleur dans le matériau cible, créant un flux thermique transitoire et, en cas de défauts, un contraste thermique. Selon la position relative de l'excitation et de la caméra, il ex-

iste deux configurations : le mode réflexion, où la source d'excitation et la caméra IR sont situées du même côté du milieu testé, et le mode transmission, où la source d'excitation et la caméra IR sont situées du côté opposé. Les sources thermiques les plus couramment utilisées en thermographie active sont l'excitation optique, l'excitation électromagnétique, l'excitation acoustique et l'excitation sous contrainte.

La solution d'un problème dédié à la caractérisation thermophysique des matériaux ou aux essais thermiques non destructifs peut être divisée en trois étapes : un problème direct, qui décrit mathématiquement l'évolution spatio-temporelle du champ de température, un problème de mesure, afin de donner le signal de sortie le plus précis et le moins bruyant, et un problème inverse, qui permet d'estimer des paramètres comme des propriétés thermophysiques constantes ou conditions aux limites des interfaces.

Puisque la physique est le fondement de chaque technique de CND, si les matériaux à l'essai sont différents, la physique et les techniques de CND seront également différentes. Les concepts de base de l'inspection thermographique sont, en général, bien établis, mais pas dans tous les cas. Cependant, l'analyse et l'inversion des données thermographiques ont tendance à être difficiles.

Cette thèse entend fournir des contributions originales sur le développement d'un modèle tridimensionnel rapide afin de simuler le contrôle thermographique non destructif de pièces planes présentant des défauts intégrés et une stratégie d'inversion robuste basée sur un modèle pour la détection et la caractérisation des défauts.

La simulation des procédures TNDT implique dans un premier temps la résolution du problème de conduction thermique dans la pièce considérée, avec et sans défauts, pour obtenir la distribution de température aux interfaces de la pièce, qui constitue la mesure. La solution complète de ce problème peut être obtenue en utilisant des techniques numériques telles que la méthode des éléments finis (FEM), méthode des différences finies (FDM), tech-

nique d'intégration finie (FIT), qui sont, en général, capables de modéliser des géométries générales et complexes.

Leur généralité est obtenue par une description discrète de l'espace, ce qui les rend dépendants du maillage. Ce point est problématique lorsque l'outil de simulation est développé à l'intention d'utilisateurs industriels, experts en CND mais ayant une connaissance limitée de l'analyse numérique en général et des stratégies de maillage en particulier. Un autre inconvénient de ces méthodes est le temps de calcul, qui peut être très élevé lorsque l'on considère de gros problèmes, même si leur complexité en termes de géométrie est faible. D'autre part, les solutions analytiques au problème thermique sont bien formulées mais leur mise en œuvre numérique n'est pas toujours aisée.

Néanmoins, dans la pratique, il est souvent utile de renoncer aux informations détaillées des solutions complètes en faveur d'approximations analytiques ou semi-analytiques rapides, qui constituent l'essence du comportement du flux thermique. Des outils de simulation basés sur des modèles semi-analytiques ont été proposés dans la littérature pour traiter des cas plus simples. Ces outils se sont avérés très rapides par rapport aux outils numériques, mais ils reposent sur des hypothèses solides qui limitent leur domaine d'application.

Cette thèse propose des solveurs hybrides combinant des solutions numériques et semi-analytiques, pour atteindre à un moment donné la généralité sans payer le prix d'un maillage tridimensionnel et d'un temps de calcul élevé.

Un modèle semi-analytique basé sur la méthode TREE (Truncated region eigenfunction expansion) est proposé pour la simulation de l'inspection thermographique. Le problème est résolu dans le domaine de Laplace en ce qui concerne le temps, et la distribution de la température est approchée par son expansion sur la base d'un produit tensoriel. Les configurations visées par ce modèle sont des pièces planes stratifiées affectées de minces défauts de délamination.

Les sources considérées sont des lampes fournissant une excitation ther-

mique à la surface de la pièce inspectée. L'excitation thermique à la surface du milieu stratifié est assurée par une lampe flash qui est utilisée dans une large gamme d'applications.

La description des défauts de délamination comme de minces espaces d'air entre les couches de pièces s'avère équivalente à l'introduction d'une résistance de surface au flux thermique, permettant ainsi leur traitement par l'approche modale appliquée sans discrétisation supplémentaire. Une validation numérique du modèle TREE développé à l'aide d'un logiciel de modélisation commercial basé sur FEM a été effectuée. Une grande concordance des résultats numériques obtenus avec le modèle TREE et avec un modèle FEM est montrée. De plus, l'accélération du modèle semi-analytique développé est décrite en détail. Les résultats numériques proposés indiquent que le modèle direct développé peut produire des signaux thermiques rapides et précis.

Parlant de la partie imagerie de cette thèse, la détection des défauts dans la pièce, à travers des signaux bruités enregistrés ou synthétiques, et leur caractérisation sont visées. Le traitement du signal, en général, est un moyen crucial pour extraire des informations utiles des données brutes capturées à partir de capteurs. De plus en plus d'algorithmes de traitement du signal incluant la reconstruction du signal thermographique (TSR), l'analyse en composantes principales (PCA), l'analyse en composantes indépendantes (ICA), la transformation en ondelettes, la décomposition de Tucker, la machine à vecteur de support (SVM) et la reconnaissance de formes sont utilisés en thermographie des composites. L'utilisation de l'une ou l'autre de ces techniques dépend de la physique du problème et leurs résultats sont généralement qualitatifs, en signifiant par cela que les défauts ne sont pas entièrement caractérisés. Selon l'application, la détection et la reconstruction de la forme des défauts peuvent être un succès. Dans certaines applications, des informations plus quantitatives sur les défauts sont nécessaires sur les paramètres que l'on essaie d'estimer.

Le processus de caractérisation des défauts de type délaminage dans les

milieux plans a été divisé en deux étapes. La première étape concerne le débruitage des signaux bruts et la détection d'éventuels défauts, et la seconde la caractérisation des défauts détectés. La première étape est réalisée en utilisant la technique TSR et l'algorithme de Canny qui sont présentés en détail. Pour la seconde étape, des techniques d'optimisation sont utilisées pour la caractérisation des défauts en utilisant les informations a priori de la partie prétraitement.

L'objectif principal de la partie imagerie est la parfaite conjonction des techniques pour avoir une procédure entièrement automatisée pour l'inspection. De nombreux résultats numériques sur la détection et la caractérisation des défauts sont fournis. Les signaux de température, dépendants du temps, obtenus avec le modèle semi-analytique ont été corrompus par différents niveaux de bruit et ont été utilisés comme signaux bruts. En appliquant la méthode TSR et l'algorithme de Canny, les défauts candidats ont été localisés avec une grande précision dans le plan transverse. Leur forme et leurs dimensions ont été utilisées pour la régularisation d'un schéma de moindres carrés afin de caractériser leur épaisseur et leur profondeur. La robustesse du schéma d'inversion a été testée dans différentes configurations difficiles. Les résultats numériques de la procédure proposée pour la détection et la caractérisation des défauts indiquent que cette procédure est rapide et précise.

Contents

List of Figures

List of Tables

Page

Chapter 1

Introduction

The service life of a structure is determined by its design, construction, ageing and maintenance during use. Damage in structures or materials can arise during material processing, fabrication of the components or in-service activities. The most common damages are cracks, delaminations, disbonds, corrosion, porosity. A wide variety of techniques are used today for condition evaluation of structures, samples or whole materials. These techniques are capable of identifying damages of a different level depending on a variety of factors. The evaluation and inspection process of materials or components for characterization or finding defects and flaws in comparison with some standards has to be done without affecting the integrity of the object being tested.

Non-destructive testing and evaluation (NDT-NDE) is a group of techniques used to evaluate the properties of a material without modifying the original properties or causing any damage to it [1]. It was the need to improve the production quality, especially after World War II, which led to the development of those methods and techniques. These techniques involve the identification and characterization of damages on the surface or interior of materials. NDT techniques provide cost-effective means of testing a sample for damages during the production and after it. In many cases, the strategy of finding a flaw may require a combination of different NDT methods. The

deep understanding of the capabilities and limitations of an NDT method is vital for the success of the evaluation of a material or a sample. Some of the most commonly used NDT methods are acoustic emission testing, eddy current testing, infrared and thermal testing, leak testing magnetic flux leakage, magnetic particle testing, liquid penetration, radiographic testing, ultrasonic testing and visual testing. The choice of the applied NDT method depends on many factors, which among others are the physical properties of the materials and the accessibility of the sample's surfaces which are of great importance.

Among the many existing methods, as stated, thermal or infrared non-destructive testing (T/INDT) is one of the most promising for inspection of materials and structures [2]. TNDT is well used in many different industrial contexts, like welding monitoring in metallurgy, in inspection of composites in aeronautics, power lines inspections in the sector of energy. The detection of irregularities is based on the principle that all bodies emit infrared radiation. This emitted infrared radiation can be measured by infrared cameras and the images analysed for the detection and characterization of flaws. Subsurface irregularities will affect the heat diffusion rate, leading to a thermal contrast on the surface of the homogeneous work-piece. By analysing alterations or the contrast in the thermal pattern of the material surface, one can obtain information about subsurface flaws. In many cases, the inspection technique exploits multi-physical phenomena, as eddy current for inductive thermography or ultrasound for thermography. As a consequence, the conversion of energy from electromagnetic or elasticity to heat is far from being trivial. In addition to modelling the evolution of temperature distribution inside the tested piece, the modelling of measurement devices like thermal imaging camera should be required, involving additional concepts of infrared radiations.

1.1 History

Even though the infrared technology started in 1800 with William Herschel and an experiment that revealed the existence of the infrared radiation spectrum [3, 4], the first use of infrared thermography, as a non-destructive testing technique, dates back to the middle of the last century in the works published by Beller and Green [5, 6]. Moreover, the heat equation, which describes the heat flow in a body, was first developed and solved by Joseph Fourier, during the same time, in 1822 [7]. Ideas of infrared applications can be tracked even before Beller and Green when Parker [8] received a patent for detecting icebergs in 1914 and Barker in 1934 proposed using infrared sensors for monitoring forest fires [9]. The pioneer of the idea of single-sided material thermophysical properties measurements is Vernotte with his published work in 1937 [10]. The first implementation of Vernottte's idea is recorded in 1956 where Hardy measured the effusivity of the skin of a patient [11]. As the milestone work can be considered the publication of Parker where the contactless, double-sided, rear-face measurement of thermal diffusivity by active infrared pulsed radiometry has been reported [12].

By the end of the 1970s, application of INDT remained qualitative thus limiting competition with other NDT techniques. Initially, INDT suffered from puzzlement and incomprehension mainly because of difficulties in the interpretation of thermograms. The heat conduction theory, which was well summarized in the books of Carslaw and Jaeger [13] and Luikov [14] improved the understanding of thermal, infrared NDT processes. The wider use of elements of the heat conduction theory paved the way to the development of a thermophysical approach to TNDT the next years by Carlomagno and Berardi [15], Vavilov and Taylor [16], Balageas *et al.* [17], Mandelis *et al.* [18] and many other authors who introduced also multi-dimensional models of defect or different detection techniques [19, 20, 21].

The use of thermography for non-destructive testing applications had received growing attention in the last years. This is mainly because infrared (IR) cameras have recently improved significantly in both sensitivity and spatial resolution. The technique has been particularly adapted to many applications [22] and especially to composites' inspection which is being used in the aerospace [23], renewable energy [24], civil and architecture [25, 26], and other industries, due to their excellent advantages. Unlike other direct imaging techniques, depending on the thermal source, it can be fast, high resolution, contactless, quantitative and low-cost technique.

1.2 Classifications of TNDT

There are many ways one could classify the different techniques of thermography. According to the presence or absence of a thermal excitation source, the technique is generally divided into two main streams, passive and active, respectively.

Passive thermography is defined as measuring the temperature difference between the target material and its surroundings under different ambient temperature conditions. Passive thermography is widely used in industrial condition monitoring [27], in building efficiency studies [28], in medical applications [29] and even for the damage characterization of Glass Fiber-Reinforced Polymer composite materials (GFRP) [30]. In general, passive thermography is more application-oriented, mostly because of the heat source, and a general analysis of it would be misleading.

Active thermography [31], on the other hand, uses a thermal source to deposit heat in the target material creating a transient heat flow and, when finding defects, thermal contrast. This can be classified by heating function, by excitation sources or by the relative position of excitation and camera. In the latter case, there are two configurations:

(a) *reflection mode*, where excitation source and IR camera are located on the same side of the tested media, and

(b) *transmission mode*, where excitation source and IR camera are located on the opposite side.

The common types of active thermography according to heating function are pulsed thermography (PT) or square pulse thermography (SPT) [32], stepped thermography (ST) [33], lock-in thermography (LT) [22], pulsed phase thermography (PPT) [21], and frequency modulated thermography (FMT) [34]. These functions are depicted in Fig. 1.2.1.

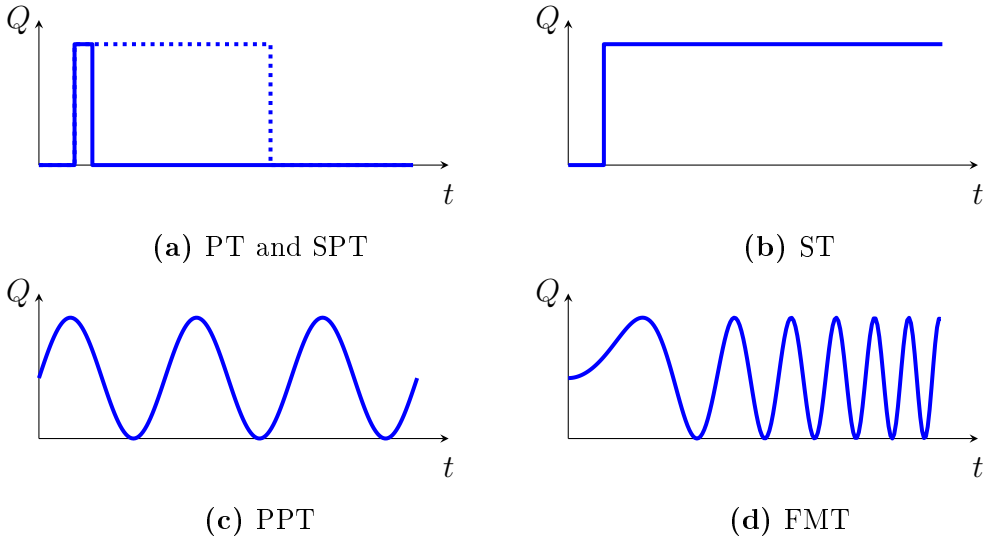

(a) PT and SPT **(b)** ST

(c) PPT **(d)** FMT

Figure 1.2.1: Excitation functions.

The most commonly used thermal sources in active thermography are optical excitation, electromagnetic excitation, acoustic excitation and stress excitation. Thermography can be classified according to excitation sources as:

1. *Optical thermography* using optical excitation such as flash lamps [35] or lasers [36, 37] that heat part of the piece surface and the resulting temperature is observed with a thermal camera. This technique is also known as pulsed thermography [38] and has been extensively used as inspection

technology for composite and layered structures. The detection can be on the same side as the heat source or the opposite side, depending on the type of access to the sample. These techniques of depositing heat on the materials have potential disadvantages, *e.g.* the reflected heat from the material can interfere with the measured signals, causing signal-to-noise-ratio (SNR) problems. For instance, many materials when used in industry are coated or painted.

2. *Eddy current thermography* (ECT) or induction thermography which uses induced eddy current to heat the sample [39, 40, 41]. In this case, the defect detection is based on the changes of the induced eddy current flow revealed by the thermal visualization captured by an IR camera and it is widely used for detection of cracks [42, 43] and corrosion [44].

3. *Magnetic induction thermography*, which is used in ferromagnetic materials to introduce heat through the magnetic field and offers several advantages over the conventional active thermography techniques like fast direct heating, no frequency optimization, no dependence on the surface absorption coefficient and penetration depth [45, 46].

4. *Microwave thermography* uses microwave as heating source for dielectric materials and gas received growing interest due to many advantages of it including strong penetrability, selective heating, volumetric heating, significant energy savings, uniform heating, and good thermal efficiency [47].

5. *Ultrasound thermography* or vibrothermography uses mechanical variations through a welding horn to heat the workpiece [48]. In this case, however, contact between the workpiece and the ultrasonic welding horn it is required, which can complicate its practical use and cause a loss of energy transmission.

Some comparison works were published by other authors where the capabilities

of different approaches have been tested [49, 50].

1.3 General context

Physics is the foundation of every NDT technique. If the materials under test are different, the physics and NDT techniques will also be different. Conventional NDT techniques are mainly developed for homogeneous metal components and its alloys. However, thermophysical behaviour of composites structures is different from planar, homogeneous materials, in general. Layered structures, for example, may include different materials. Therefore, physics and NDT techniques may be different.

The basic concepts to thermographic inspection are, in general, well established but not in every case. However, analysis and inversion of thermography data tend to be challenging because, in thermography, the underlying heat conduction phenomenon is a diffusion process. As heat diffuses in time and space, temperature differences blur, the source of the heat becomes harder and harder to resolve and the contrast created by the flaws is lower. Inversion of thermography data to identify a heat source or boundary location is, therefore, an uncertain process potentially requiring substantial assumptions.

The solution of a problem dedicated to the thermophysical characterization of materials or thermal non-destructive testing could be divided into three stages: a *forward problem*, a *metrology problem* and an *inverse problem*.

A forward problem mathematically describes the space-time evolution of the temperature field as accurately and simply as possible given a knowledge of the medium and illuminating source.

A metrology problem gives the most accurate and least noisy output signal. A priori information can complete the information given by this signal [51, 52, 53].

An inverse problem permits estimation of parameters (constant thermophysical properties or boundary interface conditions uniform in space and changing with time or temperature). This task is accomplished by seeking reversible operators or optimization techniques to get a minimum deviation between the measured data and the forward problem. In some applications, signal or image processing techniques can provide the sought parameters.

1.3.1 Simulation and modelling

Simulation of TNDT procedures involves at a first step the solution of the heat conduction problem in the considered work-piece, with and without defects, in order to obtain the temperature distribution at the piece interfaces, which constitutes the measurement. The full solution to this problem can be obtained using numerical techniques such as finite element method (FEM) [54, 55], finite difference method (FDM) [56, 57, 58], finite integration technique (FIT) [59] which are, in general, able to model complex geometries. Nonetheless, their multi-dimensional implementation usually is computationally costly.

On the other hand, analytical solutions for the thermal problem are well formulated and summarised in some classical books [60, 61, 62] but their numerical implementation is not always an easy task. Nevertheless, in practical situations, it is often meaningful to renounce the detailed information of complete solutions in favour of fast analytical or semi-analytical approximations, which hold the essence of the thermal flow behaviour.

One-dimensional approaches for the analytic solution of the thermal problem can be found for three-layer [63] and multi-layer [64] composite slab. A semi-analytical solution for multilayer diffusion in a composite medium consisting of a large number of layers was given by Carr [65], based on the Laplace transform and orthogonal eigenfunction expansion.

Analytical solutions for multi-dimensional time-dependent heat conduction in media consisting of several layers have been given using different approaches.

The orthogonal expansion technique derived by Padovan [66] Salt [67, 68] and Mikhailov and Özışık [69] analyses two- and three-dimensional generalized version of the classical Sturm-Liouville procedure [70], however, no numerical results was provided. The Green function solution method developed by Beck was applied to a three-dimensional two-layer isotropic-composite [71] and orthotropic-composite [72] slab with an internal heat source. The Laplace transform approach used by Levine [73], and Kozlov and Mandrix [74, 75] in a two-dimensional approach in a spherical surface object and a cylinder, respectively, were used, but also here, no numerical results provided. An analytical solution obtained by solving the transient three-dimensional heat conduction equation using the Laplace transform for a unit impulse in a finite domain by the method of separation of variables was presented with numerical results by Araya and Gutierrez [76]. A very popular, well-established approach is the so-called thermal quadrupoles method, where the original three-dimensional problem is approximated as a multilayer one-dimensional problem (by ignoring the heat flow in the lateral layers directions) and modelled as a cascade of "quadrupoles" in analogy with electrical network theory [77].

1.3.2 Signal processing algorithms and inversion techniques

Signal processing (SP) is a crucial mean to extract useful information from raw data captured from sensors. More and more signal processing algorithms including thermographic signal reconstruction (TSR) [78, 79], principal components analysis (PCA) [80], independent components analysis (ICA) [81, 82], wavelet transform [83] , Tucker decomposition [84, 85], support vector machine (SVM) [86], and pattern recognition [87] are being used in thermography for composites. The use of any of the aforementioned techniques depends on the physics of the problem and their results are usually qualitative, saying that

the defects are not fully characterised. Depending on the application, the detection and the shape reconstruction of the defects may be a success. In some applications, more quantitative information about the defects is required on the parameters ones tries to estimate.

On the other hand, using model-based techniques, the depth profile reconstruction of a work-piece has been tried. In the frequency domain a stepwise least-squares fit has been used to reconstruct a polygon best approximation to the conductivity profile [88, 89, 90], a neural network approach to find the best fit [91], an inverse procedure to find the Taylor expansion parameters of the conductivity profiles [92], an inverse Green's function technique to localize sources in inverse heat conduction [93, 94], a Hamilton/Jacobi based model for weak scattering [18, 95] and a thermal wave impedance-based model [96]. In the spatial domain the inverse scattering technique has been used to reconstruct both thermal conductivity and heat capacity depth profiles [97] and the conjugate gradient technique has been used to optimise the fit. In the time domain, the effusivity depth profile has been reconstructed [17, 98] and the neural network approach has been used to find the best fit [99].

In his book [100], Beck provides a summary of his work on inverse heat conduction problems. Exact solutions of the inverse heat conduction problems and estimation procedures with application to engineering problems are provided. Özışık and Orlande in their book [101] present in detail the basic steps of four techniques of solution of inverse heat transfer problem, as a parameter estimation approach and as a function estimation approach. A range of applications of such techniques to the solution of inverse heat transfer problem of practical engineering interest, involving conduction, convection and radiation has been presented. The authors introduce a formulation based on generalised coordinates for the solution of inverse heat conduction problems in two-dimensional regions.

1.4 Object of the thesis

This thesis aims to provide original contributions on both aspects of thermography that are the forward modelling and the inverse one: The first consists of computing the excitation terms, the thermal diffusion phenomenon and the measurement of the temperature distribution at the observed surface. The second, in which information about the work-piece is retrieved from thermographic measurement and the knowledge of the forward process on one side, and some a priori information on the other side.

Concerning the forward modelling, many numerical solvers already exist for the solution of the heat equation in two or three dimensions. Their generality is obtained through a discretized description of space, which makes them case dependent from the meshing point of view. This point is a problematic one when the simulation tool is developed toward industrial users, who are experts in NDT techniques but have limited knowledge of numerical analysis in general and meshing strategies in particular. Another disadvantage of such methods is computation time, which can be very high when considering large problems, even if their complexity in terms of geometry is low.

Simulation tools based on semi-analytical models have been proposed in the literature to address simpler cases. These tools are proven to be very fast in comparison to numerical ones, but make some strong assumptions that limits their domain of application. This thesis aims at proposing hybrid solvers combining numerical and semi-analytical solutions, to achieve at some point generality without paying the price of a three-dimensional meshing and high computational time. Besides, the adaptation of modal methods that have been proven to be very efficient in low-frequency electromagnetics will constitute an original contribution to the community of thermography simulation.

Speaking of the imaging part, the detection of the flaws in the work-piece, through recorded or synthetic noisy signals, and their characterization is aimed

at. Signal techniques will be used to denoise the temperature time-dependent signals and compress them. The detection of the flaws will be conducted with image processing techniques. Last, optimization techniques will be used for the characterization of the flaws using a priori information from the preprocessing part. The main goal of the imaging part is the perfect conjunction of the techniques to have a fully automated procedure for the inspection.

1.5 Thesis outlines

The thesis is divided into five chapters. The first one introduces the research framework and the contributions of this thesis. The theoretical background of modelling in thermography non-destructive testing is introduced in Chapter 2 where a semi-analytical model based on the so-called truncated region eigenfunction expansion method is proposed. The general theory of the strategy used for defect characterization is introduced in Chapter 3. The used techniques and methods for the detection and the characterization of abnormalities in planar media are presented in detail. The numerical implementation of the derived semi-analytical model, its numerical evaluation and its computational performance are discussed in detail in Chapter 4. This discussion is followed by numerical results of the forward model as well as results for delamination detection and characterization in planar layered media. Chapter 5 summarizes the achieved work and sets forth some perspectives. Appendices provide supplementary materials, including the published and submitted contributions.

Chapter 2

Modelling in TNDT

2.1 The differential heat conduction equation for homogeneous isotropic solid

The starting point is the heat equation, also called the heat conduction equation for a stationary, homogeneous, isotropic solid with heat generation within the body:

$$\nabla^2 T(\boldsymbol{r},t) - \frac{1}{\alpha}\frac{\partial}{\partial t}T(\boldsymbol{r},t) = -\frac{1}{k}g(\boldsymbol{r},t) \tag{2.1.1}$$

which describes how the distribution of heat evolves over time in a body. The *temperature* T, [K] is a function of *space* $\boldsymbol{r} \in \mathbb{R}^3$, [m] and *time* [s]. The constant α is a material-specific quantity called by Kelvin *thermal diffusivity* of the substance [$\mathrm{m^2 s^{-1}}$] and is defined as:

$$\alpha = \frac{k}{\rho c_p}. \tag{2.1.2}$$

The parameter k is the *thermal conductivity* [$\mathrm{Wm^{-1}K^{-1}}$] of the region of space where the Eq. (2.1.1) holds. In general the thermal conductivity may be a function of temperature and therefore may vary with position in the body.

The parameter ρ is the *mass density* [kgm^{-3}] and c_p the *specific heat capacity* at constant pressure [$\mathrm{Jkg}^{-1}\mathrm{K}^{-1}$]. In general the density and the specific heat capacity are functions of temperature but small fluctuations of temperature do not affect significantly their values.

On the right-hand side of Eq. (2.1.1), the term $g(\boldsymbol{r}, t)$ is the *thermal source volumetric density* which expresses the energy generation throughout the volume of the body and its unit is [Wm^{-3}]. It is distinguished from energy that enters the body through its boundaries. The energy generation is in the general case a function of the position in the body and it may vary with time.

The differential equation of heat conduction is a consequence of the energy conservation law and Fourier's law of conduction, which in its differential form states that the local heat flux density $\boldsymbol{J}$ is equal to the product of thermal conductivity k and the negative local temperature gradient, $-\nabla T$

$$\boldsymbol{J} = -k\nabla T. \tag{2.1.3}$$

In the Cartesian coordinate system, for an isotropic body, the heat flux vector can be decomposed as:

$$J_x = -k\frac{\partial T}{\partial x}, \qquad J_y = -k\frac{\partial T}{\partial y}, \qquad J_z = -k\frac{\partial T}{\partial z}. \tag{2.1.4}$$

2.1.1 Boundary and initial conditions

This thesis is concerned with solutions to the heat conduction equation as they apply to problems in engineering and physics. The mathematical form of the solutions is determined by the boundary conditions, that is, the value of the temperature or its derivative at the boundaries of the heat conducting body. The combination of the heat conduction equation, the specific boundary conditions, and the initial condition is called a boundary value problem. This

thesis is concerned with orthogonal bodies, whose boundaries coincides with one constant coordinate. The number of boundary conditions for a boundary value problem depends on the form of the heat conduction equation and the geometry of the system under consideration.

Six different boundary conditions are given here, which covers a wide range of possible situations one could face.

I. The *first* kind of boundary condition is the prescribed temperature at boundary i,

$$T(\boldsymbol{r}_i, t) = f_i(\boldsymbol{r}_i, t) \tag{2.1.5}$$

where $f_i(\boldsymbol{r}_i, t)$ is the space- and time-dependent surface temperature.

II. The *second* kind of boundary condition is prescribed heat flux,

$$k \left.\frac{\partial T}{\partial n_i}\right|_{\boldsymbol{r}_i} = f_i(\boldsymbol{r}_i, t) \tag{2.1.6}$$

where n_i is an outward pointing normal.

III. The *third* kind is a convective boundary condition,

$$k \left.\frac{\partial T}{\partial n_i}\right|_{\boldsymbol{r}_i} + h_i \, T|_{\boldsymbol{r}_i} = f_i(\boldsymbol{r}_i, t) \tag{2.1.7}$$

where h_i is the heat transfer coefficient and $f_i(\boldsymbol{r}_i, t)$ being usually equal to $h_i T_\infty$ with T_∞ being the ambient temperature. This does not exclude the case of $f_i(\boldsymbol{r}_i, t)$ including a prescribed heat flux.

IV. The *fourth* kind is for a thin film at a surface with a prescribed heat flux $f_i(\cdot)$,

$$k \left.\frac{\partial T}{\partial n_i}\right|_{\boldsymbol{r}_i} = f_i(\boldsymbol{r}_i, t) - (\rho c_p d)_i \left.\frac{\partial T}{\partial t}\right|_{\boldsymbol{r}_i} \tag{2.1.8}$$

where $(\rho c_p d)_i$ if for the thin film and d is its thickness at the ith surface.

V. The *fifth* kind of boundary condition is for a thin film permitting losses from the film convection,

$$k \left.\frac{\partial T}{\partial n_i}\right|_{\boldsymbol{r}_i} + h_i \, T|_{\boldsymbol{r}_i} = f_i(\boldsymbol{r}_i, t) - (\rho c_p d)_i \left.\frac{\partial T}{\partial t}\right|_{\boldsymbol{r}_i} \tag{2.1.9}$$

This boundary condition is physically identical to the fourth kind boundary condition except that instead of a specified heat flux on the thin film at the surface there is a specified heat transfer coefficient h.

VI. Another important case is the *zeroth* kind, the so-called natural boundary condition or the absorbing boundary condition. It is for conditions for which there is no physical boundary but for computational purposes boundary condition has to be imposed to the problem. It includes several cases, one of which is when a boundary extends to infinity.

When a system consists of a composite body, interface conditions are applied in a manner similar to the boundary conditions at the interfaces of the body's parts. Suppose here a system of two different media with different thermal properties. Let $T^{(1)}$ be the temperature in the first media and $T^{(2)}$ in the second one, with $k^{(1)}$ and $k^{(2)}$ being the corresponding conductivities. Two types of interface conditions can be defined here.

A. *Perfect contact*

$$T^{(1)}\big|_{\boldsymbol{r}_i} = T^{(2)}\big|_{\boldsymbol{r}_i} \tag{2.1.10a}$$

$$-\, k^{(1)} \left.\frac{\partial T^{(1)}}{\partial n_i}\right|_{\boldsymbol{r}_i} = -\, k^{(2)} \left.\frac{\partial T^{(2)}}{\partial n_i}\right|_{\boldsymbol{r}_i} . \tag{2.1.10b}$$

These conditions apply in the case of close contact between the two media. The first equation sets continuity of the temperature and the second equation sets continuity of the heat flux through the interface.

B. *Interface heat source*

$$T^{(1)}\big|_{\boldsymbol{r}_i} = T^{(2)}\big|_{\boldsymbol{r}_i} \tag{2.1.11a}$$

$$-k^{(1)}\frac{\partial T^{(1)}}{\partial n_i}\bigg|_{\boldsymbol{r}_i} = -k^{(2)}\frac{\partial T^{(2)}}{\partial n_i}\bigg|_{\boldsymbol{r}_i} + f_i(\boldsymbol{r}_i, t). \tag{2.1.11b}$$

These conditions correspond to heat production or absorption at the location of the interface . In this way, a heating film *i.e. Joule effect* between the two media can be treated. The film is considered to have high thermal conductivity and low thermal capacity.

In the transient regime, in order to complete the formulation of the problem, an initial temperature distribution has to be set. Expressed in general coordinates this equation is

$$T(\boldsymbol{r}, 0) = F(\boldsymbol{r}) \tag{2.1.12}$$

and for an one-dimensional case with x being the coordinate, $T(x, 0) = F(x)$. Often, instead of $F(\cdot)$ the notation T_0 is used to denote the initial condition where the space variable has been omitted and the subscript zero states the initial time, $t = 0$.

Without loss of generality and since it is mathematically convenient one can choose the zero of the temperature scale as an initial condition. This is allowed by the gauge invariance of the temperature which implies that the solution for the temperature does not depend on the choice of the initial temperature or its scale.

2.2 Heat equation in planar layered media in time domain

The geometry of the developed models in this thesis concerns three-dimensional, planar, multi-layered structures with respect to the z-direction. For simplicity, our model consists of two thin layers of different solids, infinite in the x and y-directions, above and below them semi-infinite, in the z-direction, layers of air completing the physical configuration depicted in Fig. 2.2.1. The heat diffusion phenomena can be described in each layer by Eq. (2.2.1a) with $T^{(j)}$ being the temperature in the jth layer of the media.

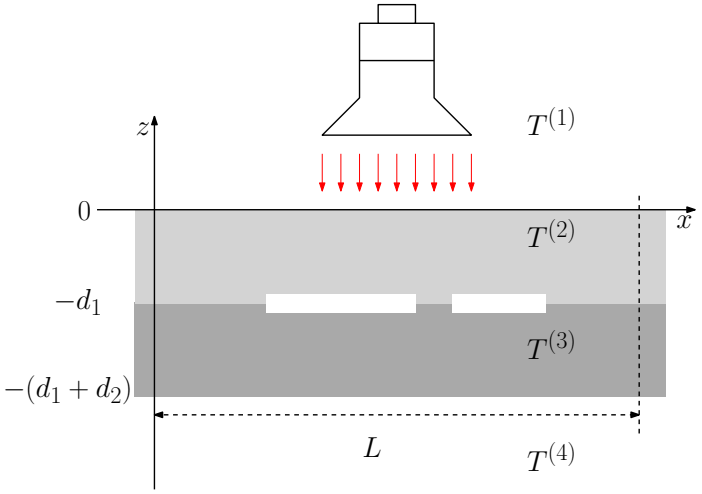

Figure 2.2.1: Two-dimensional illustration of a typical thermographic inspection consisting of a double-layered piece of two different materials illuminated by a flash lamp with two insertions.

Equations (2.2.1f) and (2.2.1g) describe the temperature and the heat flux continuity, respectively, at the interface ($z = z_i$) where perfect contact between the layer (j) and ($j + 1$) has been assumed.

The system is thermally excited by a flash lamp set above the second layer. The impact of the excitation can be modelled in terms of an additional thermal flux at the interface between the first and second layers of the model and perpendicular to this interface. The continuity conditions at this interface are

described by Eq. (2.1.11) where the function f_i has been replaced now by the term J_e [Wm^{-2}], see Eq. (2.2.1c).

Regions of imperfect contact, *i.e.*, flaws, between the second and third layer can be introduced into the model. The flaws will be modelled as very thin insertions between the second and third layers. By modelling the flaws as very thin with respect to the z-direction, they can be represented by a thermal resistance $R(x, y)$ between the two layers. The effect of the flaws can be introduced into the mathematical model by modifying the temperature continuity relation at that interface, which leads to Eq. (2.2.1d).

With the first and last layers being semi-infinite, it is physically correct to assume that the temperature far away from the source will remain at its initial ambient temperature T_0. Mathematically, the problem depicted in Fig. 2.2.1 can be expressed by the system Eq. (2.2.1).

$$\nabla^2 T^{(j)}(\boldsymbol{r}, t) - \frac{1}{\alpha^{(j)}} \frac{\partial}{\partial t} T^{(j)}(\boldsymbol{r}, t) = 0 \tag{2.2.1a}$$

$$T^{(1)}\big|_{z_1} = T^{(2)}\big|_{z_1} \tag{2.2.1b}$$

$$-k^{(1)} \frac{\partial T^{(1)}}{\partial z}\bigg|_{z_1} = -k^{(2)} \frac{\partial T^{(2)}}{\partial z}\bigg|_{z_1} + J_e(x, y) \cdot \delta(t) \tag{2.2.1c}$$

$$T^{(2)}\big|_{z_2} - T^{(3)}\big|_{z_2} = -R(x, y) \cdot k^{(2)} \left.\frac{\partial T^{(2)}}{\partial z}\right|_{z_2} \tag{2.2.1d}$$

$$-k^{(2)} \frac{\partial T^{(2)}}{\partial z}\bigg|_{z_2} = -k^{(3)} \frac{\partial T^{(3)}}{\partial z}\bigg|_{z_2} \tag{2.2.1e}$$

$$T^{(3)}\big|_{z_3} = T^{(4)}\big|_{z_3} \tag{2.2.1f}$$

$$-k^{(3)} \frac{\partial T^{(3)}}{\partial z}\bigg|_{z_3} = -k^{(4)} \frac{\partial T^{(4)}}{\partial z}\bigg|_{z_3} \tag{2.2.1g}$$

$$\lim_{z\to-\infty} T^{(1)} = T_0 \tag{2.2.1h}$$

$$\lim_{z\to-\infty} T^{(4)} = T_0 \tag{2.2.1i}$$

$$T^{(j)}(\boldsymbol{r}, 0) = T_0 \tag{2.2.1j}$$

2.3 Transformation of the problem in Laplace domain

The boundary value problem described by Eq. (2.2.1) will be solved in the Laplace domain with respect to time. Assuming that the temporal one-side Laplace transform of $T(\boldsymbol{r}, t)$ exists,

$$\mathcal{L}\{T(\boldsymbol{r}, t)\} \equiv \widehat{T}(\boldsymbol{r}, s) = \int_0^\infty T(\boldsymbol{r}, t) e^{-st}\, \mathrm{d}t \tag{2.3.1}$$

where s is the Laplace variable, the system defined by Eq. (2.2.1) can be transformed to the Laplace domain. The governing equation (2.2.1a) becomes

$$\nabla^2 \widehat{T}^{(j)}(\boldsymbol{r}, s) - \frac{s}{\alpha^{(j)}} \widehat{T}(\boldsymbol{r}, s) + T(\boldsymbol{r}, 0^-) = 0 \tag{2.3.2}$$

where $T(\boldsymbol{r}, 0^-)$ refers to the temperature before the initial time and from now on will be assumed to be zero, $T(\boldsymbol{r}, 0^-) = 0$. The boundary value problem in the Laplace domain becomes

$$\nabla^2 \widehat{T}^{(j)}(\boldsymbol{r}, s) - \frac{s}{\alpha^{(j)}} \widehat{T}(\boldsymbol{r}, s) = 0 \tag{2.3.3a}$$

$$\widehat{T}^{(1)}\Big|_{z_1} = \widehat{T}^{(2)}\Big|_{z_1} \tag{2.3.3b}$$

$$-k^{(1)} \frac{\partial \widehat{T}^{(1)}}{\partial z}\bigg|_{z_1} = -k^{(2)} \frac{\partial \widehat{T}^{(2)}}{\partial z}\bigg|_{z_1} + J_e(x, y) \tag{2.3.3c}$$

$$\widehat{T}^{(2)}\Big|_{z_2} - \widehat{T}^{(3)}\Big|_{z_2} = -R(x,y)\cdot k^{(2)}\left.\frac{\partial \widehat{T}^{(2)}}{\partial z}\right|_{z_2} \tag{2.3.3d}$$

$$-k^{(2)}\frac{\partial \widehat{T}^{(2)}}{\partial z}\Big|_{z_2} = -k^{(3)}\frac{\partial \widehat{T}^{(3)}}{\partial z}\Big|_{z_2} \tag{2.3.3e}$$

$$\widehat{T}^{(3)}\Big|_{z_3} = \widehat{T}^{(4)}\Big|_{z_3} \tag{2.3.3f}$$

$$-k^{(3)}\frac{\partial \widehat{T}^{(3)}}{\partial z}\Big|_{z_3} = -k^{(4)}\frac{\partial \widehat{T}^{(4)}}{\partial z}\Big|_{z_3} \tag{2.3.3g}$$

$$\lim_{z\to-\infty}\widehat{T}^{(1)} = \widehat{T}_0 \tag{2.3.3h}$$

$$\lim_{z\to-\infty}\widehat{T}^{(4)} = \widehat{T}_0 \tag{2.3.3i}$$

2.4 The TREE method

A classical analytical solution of a thermal problem is given by, perhaps the most powerful analytical method, separation of variables. This aspect of analytical solutions has been explored in depth. In this thesis, a semi-analytical solution of the (translated in the Laplace domain with respect to time) thermal diffusion problems which are based on Truncated Region Eigenfunction Expansion (TREE) method is proposed. This method was historically introduced to solve low-frequency electromagnetic problems [102]. As in the classical approach, the method uses separation of variables to express the temperature field in the various regions of the problem in analytical form. The solution domain is subject to truncation to limit the range of a coordinate that would otherwise have an infinite span. As a result, the solution on that coordinate is expressed in a series form, instead of an integral form, which has numerous advantages.

The main advantage of the domain truncation is the satisfaction of the field continuity at various interfaces simultaneously after a selection of the discrete eigenvalues and the corresponding eigenfunctions. This expands the class of problems which can be treated by the method. The matching of the field expressions at interfaces is done either in a term by term basis or by mode-matching where the testing functions are the same as the expansion ones. The later allows the TREE method to contain a mesh-less Galerkin type procedure. This advantage may arise, for example, in layered media, when one of the layers is much narrower than the other layers or when the thermal properties change radically between the media's layers. In such cases, the accuracy of the solution is independent of the meshing of the computational domain. This is in contrast with numerical methods where refinement of the mesh may be required in parts of the computational domain.

The method is shown to provide easily calculated accurate solutions. In general, the series-form nature of these solutions makes their numerical implementation easy in a machine using any low-level programming language or even commercial mathematical packages. Moreover, they are extremely fast and more memory efficient compared to numerical methods. Due to their accuracy they can easily be used for analysis, parametric studies or calibration of test systems. These models provide an inexpensive alternative to experimental verification of numerical methods. Thus, they can be widely used for validation of solutions from more complex numerical methods.

2.4.1 The TREE formulation of the problem

The boundary value problem described by Eq. (2.3.3) is solved in the Laplace domain with respect to time. The solution of the problem with the TREE method requires the truncation of the solution domain. That is done with respect to x-coordinate and y-coordinate. This is an accurate enough approximation when these limits are at a distance large enough so as the heat flaw

in the region of interest is not affected by their presence.

To truncate the solution domain one has to impose boundary conditions at $x = 0$, $x = L_x$ and $y = 0$, $y = L_y$. The method gives freedom in the choice of the boundary conditions. Dirichlet boundary conditions can be used, where the field values on the boundary are specified, Neumann boundary conditions, where the normal derivatives of the field on the boundaries are specified, or even mixed boundary conditions, where field values are known on part of the boundary while normal derivatives are known from the remaining part of the boundary. If the geometry of the problem, as due to symmetry for example, does not imply any boundary conditions the most mathematically convenient choice should be used.

In our case, Dirichlet boundary conditions

$$\widehat{T}^{(j)}\Big|_{x=0} = \widehat{T}^{(j)}\Big|_{x=L_x} = 0 \tag{2.4.1a}$$

$$\widehat{T}^{(j)}\Big|_{y=0} = \widehat{T}^{(j)}\Big|_{y=L_y} = 0 \tag{2.4.1b}$$

will be applied in both x and y-directions.

The first step of the method is the application of the separation of variables. One assumes that the unknown function $\widehat{T}$ which satisfies the heat equation

$$\nabla^2\widehat{T}(x,y,z;s) - \frac{s}{\alpha}\widehat{T}(x,y,z;s) = 0 \tag{2.4.2}$$

is a product of three one-variable functions as follows:

$$\widehat{T}(x,y,z;s) = X(x)Y(y)Z(z). \tag{2.4.3}$$

In equation (2.4.2), $\widehat{T}(x,y,z;s)$ is considered to be only a function of the spatial variables (x,y,z) and the Laplace frequency (s) is considered to be a parameter. Substituting Eq. (2.4.3) in Eq. (2.4.2) one obtains the following

differential equation:

$$YZ\frac{\mathrm{d}^2X}{\mathrm{d}x^2} + XZ\frac{\mathrm{d}^2Y}{\mathrm{d}y^2} + XY\frac{\mathrm{d}^2Z}{\mathrm{d}z^2} - \frac{s}{\alpha}XYZ = 0. \tag{2.4.4}$$

Dividing Eq. (2.4.4) by the product XYZ, which is not zero, yields:

$$\frac{1}{X}\frac{\mathrm{d}^2X}{\mathrm{d}x^2} + \frac{1}{Y}\frac{\mathrm{d}^2Y}{\mathrm{d}y^2} + \frac{1}{Z}\frac{\mathrm{d}^2Z}{\mathrm{d}z^2} = \frac{s}{\alpha}. \tag{2.4.5}$$

Each term in Eq. (2.4.5) is a function of one variable only, and therefore, each term must be equal to a constant, in order for Eq. (2.4.3) to be satisfied for arbitrary values of the three independent variables (x, y, z). This means that the following equations should hold:

$$\frac{1}{X}\frac{\mathrm{d}^2X}{\mathrm{d}x^2} = -\kappa^2 \tag{2.4.6a}$$

$$\frac{1}{Y}\frac{\mathrm{d}^2Y}{\mathrm{d}y^2} = -\lambda^2 \tag{2.4.6b}$$

$$\frac{1}{Z}\frac{\mathrm{d}^2Z}{\mathrm{d}z^2} = \mu^2. \tag{2.4.6c}$$

Considering the differential equations (2.4.6), the general solution can be written as

$$\begin{aligned}\widehat{T}^{(j)}(x, y, z; s) = &\left[A_1^{(j)}\sin(\kappa x) + A_2^{(j)}\cos(\kappa x)\right] \\ &\times \left[B_1^{(j)}\sin(\lambda y) + B_2^{(j)}\cos(\lambda y)\right] \\ &\times \left[C_1^{(j)}\exp(-\mu^{(j)}z) + C_2^{(j)}\exp(\mu^{(j)}z)\right]\end{aligned} \tag{2.4.7}$$

for each (j) layer. The constants $A_1, A_2, B_1, B_2, C_1, C_2$ are to be determined by satisfying the boundary and interface conditions. The separation constants are linked together through the dispersion equation:

$$\mu^{(j)} = \sqrt{\kappa^2 + \lambda^2 + \frac{s}{\alpha^{(j)}}}. \tag{2.4.8}$$

If the region of interest was infinite one would have to integrate over κ and λ from 0 to ∞ to get the general solution. Since the solution region is finite, due to truncation, κ and λ assume discrete values and to get the solution one has to sum the modes up to ∞.

The Dirichlet boundary conditions, Eq. (2.4.1), should be satisfied in x- and y-direction from which the discrete eigenvalues κ_m and λ_n are to be determined as

$$\sin(\kappa_m L_x) = 0, \qquad \kappa_m = \frac{m\pi}{L_x}, \qquad m \in \mathbb{Z}^* \tag{2.4.9a}$$

$$\sin(\lambda_n L_y) = 0, \qquad \lambda_n = \frac{n\pi}{L_y}, \qquad n \in \mathbb{Z}^* \tag{2.4.9b}$$

respectively. Thus, the dispersion equation (2.4.8) which links the discrete eigenvalues can be written as

$$\mu_{mn}^{(j)} = \sqrt{\kappa_m^2 + \lambda_n^2 + \frac{s}{\alpha^{(j)}}}, \quad m, n \in \mathbb{Z}. \tag{2.4.10}$$

The general solution, Eq. (2.4.7), should respect the applied Dirichlet boundary conditions, Eq. (2.4.1), that have been set due to truncation of the region in the x- and y-directions. Thus, equation (2.4.7) can be written as

$$\begin{aligned} \widehat{T}_{mn}^{(j)}(x, y, z; s) = {} & A_{1;m}^{(j)} \sin(\kappa_m x) \\ & \times B_{1;n}^{(j)} \sin(\lambda_n y) \\ & \times \left[C_{1;mn}^{(j)} \exp(-\mu_{mn}^{(j)} z) + C_{2;mn}^{(j)} \exp(\mu_{mn}^{(j)} z) \right] \end{aligned} \tag{2.4.11}$$

for each (j) layer. The solution in the x- and y-directions is expressed only by $\sin(\cdot)$ because of the Dirichlet boundary conditions where the terms of $\cos(\cdot)$ in the general solution have to be dismissed. The constants A_1, B_1 can be absorbed by the constants C_1, C_2 where we write them now as C and D, respectively, in order to simplify the notation. The general solution, for each

m and n, can be written as

$$\widehat{T}^{(j)}_{mn}(x,y,z;s) = \sin(\kappa_m x) \times \sin(\lambda_n y) \times \left[C^{(j)}_{mn}\exp(-\mu^{(j)}_{mn}z) + D^{(j)}_{mn}\exp(\mu^{(j)}_{mn}z)\right]. \tag{2.4.12}$$

By setting the truncation limits M and N in the x- and y-directions, respectively, the temperature field in the Laplace domain for each (j) layer is given by

$$\widehat{T}^{(j)}(x,y,z;s) = \sum_{m=1}^{M}\sum_{n=1}^{N}\left[C^{(j)}_{mn}\exp(-\mu^{(j)}_{mn}z) + D^{(j)}_{mn}\exp(\mu^{(j)}_{mn}z)\right]\sin(\kappa_m x)\sin(\lambda_n y). \tag{2.4.13}$$

Given the condition

$$\lim_{z\to\pm 0}\widehat{T}(x,y,z;s) = 0$$

an expression can be given for each layer of the considered configuration

$$\widehat{T}^{(1)}(x,y,z;s) = \sum_{m=1}^{M}\sum_{n=1}^{N} C^{(1)}_{mn}e^{-\mu^{(1)}_{mn}z}\sin(\kappa_m x)\sin(\lambda_n y) \tag{2.4.14a}$$

$$\widehat{T}^{(2)}(x,y,z;s) = \sum_{m=1}^{M}\sum_{n=1}^{N}\left[C^{(2)}_{mn}e^{-\mu^{(2)}_{mn}(z+d_1)} + D^{(2)}_{mn}e^{\mu^{(2)}_{mn}z}\right]\sin(\kappa_m x)\sin(\lambda_n y) \tag{2.4.14b}$$

$$\widehat{T}^{(3)}(x,y,z;s) = \sum_{m=1}^{M}\sum_{n=1}^{N}\left[C^{(3)}_{mn}e^{-\mu^{(3)}_{mn}(z+d_1+d_2)} + D^{(3)}_{mn}e^{\mu^{(3)}_{mn}(z+d_1)}\right]\sin(\kappa_m x)\sin(\lambda_n y) \tag{2.4.14c}$$

$$\widehat{T}^{(4)}(x,y,z;s) = \sum_{m=1}^{M}\sum_{n=1}^{N} D^{(4)}_{mn}e^{\mu^{(4)}_{mn}(z+d_1+d_2)}\sin(\kappa_m x)\sin(\lambda_n y). \tag{2.4.14d}$$

The excitation term has been introduced in the model as a thermal flux $J_e(x,y)$ at the interface between the first layer and the second layer located at

the altitude $z = 0$. From Fourier's law one has

$$J_e(x, y) = -k^{(1)} \frac{\partial \widehat{T}^{(e)}}{\partial z} \tag{2.4.15}$$

and by using Eq. (2.4.15) and the expression for the temperature field from Eq. (2.4.14b) one has

$$J_e(x, y) = -k^{(1)} \sum_{m=1}^{M} \sum_{n=1}^{N} \mu_{mn}^{(21} C_{mn}^{(e)} \sin(\kappa_m x) \sin(\lambda_n y). \tag{2.4.16}$$

The coefficients of the excitation term can be calculated by projecting Eq. (2.4.16) into the orthogonal basis in the x- and y-directions. The orthogonality of the basis implies

$$\int_0^{L_x} \sin(\kappa_m x) \sin(\kappa_{m'} x) \, \mathrm{d}x = \begin{cases} \frac{L_x}{2}, & \text{if } m = m' \\ 0, & \text{if } m \neq m' \end{cases} \tag{2.4.17}$$

$$\int_0^{L_y} \sin(\lambda_n y) \sin(\lambda_{n'} x) \, \mathrm{d}x = \begin{cases} \frac{L_y}{2}, & \text{if } n = n' \\ 0, & \text{if } n \neq n' \end{cases}. \tag{2.4.18}$$

Assuming that $J_e(x, y)$ is non-zero and constant only inside a rectangular patch extending from x_1 to x_2 and from y_1 to y_2 with $0 < x_1 < x_2 < L_x$ and $0 < y_1 < y_2 < L_y$ the coefficients for the excitation term can be calculated explicitly according to

$$C_{mn}^{(e)} = -\frac{Q}{k^{(1)} \mu_{mn}^{(1)}} \frac{4}{L_x L_y} \int_{y_1}^{y_2} \int_{x_1}^{x_2} \sin(\kappa_m x) \sin(\lambda_n y) \, \mathrm{d}x \, \mathrm{d}y \tag{2.4.19}$$

where Q is the constant intensity of the source in its domain of support. In the case of a more general source which is a function of space, the coefficients

for the source term can be calculated by

$$C_{mn}^{(e)} = -\frac{1}{k^{(1)}\mu_{mn}^{(1)}}\frac{4}{L_x L_y}\int_{y_1}^{y_2}\int_{x_1}^{x_2} J_e(x,y)\sin(\kappa_m x)\sin(\lambda_n y)\,\mathrm{d}x\,\mathrm{d}y. \quad (2.4.20)$$

The contact between the second layer and the third layer in the geometry shown in Fig. 2.2.1 is imperfect in a sub-domain of their interface. As declared previously, this kind of imperfect contact between the two layers can model a very thin delamination. In this case, the effect of the delamination can be taken into account by only modifying locally the temperature continuity relation between the two layers Eq. (2.3.3d). To be more specific, let us consider a very thin defect between two planar media as shown in Fig. 2.4.1 where $\mathcal{D}$ is the region of the delamination, Δz is the size of this area in the z direction, S_a and S_b are two fictitious surfaces parallel to the interface between the two layers at a distance $\Delta z/2$ from them.

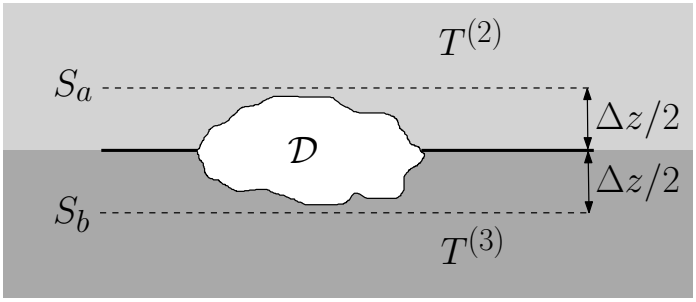

Figure 2.4.1: Modelling the delamination

By applying Fourier's law between the fictitious surfaces S_a and S_b one has

$$J_z = -k_d \nabla \widehat{T} \quad (2.4.21)$$

$$J_z = -k_d \frac{\widehat{T}^{(2)} - \widehat{T}^{(3)}}{\Delta z} \quad (2.4.22)$$

which leads to

$$\widehat{T}^{(2)} - \widehat{T}^{(3)} = -R(x,y)J_z \quad (2.4.23)$$

where J_z is the heat flux in the z direction and $R(x, y)$ represents the thermal resistance between the two layers defined as

$$R(x, y) = \frac{\Delta_z}{k_d}, \quad (x, y) \in \mathcal{D} \tag{2.4.24}$$

inside the defect domain $\mathcal{D} \in (0, L_x) \times (0, L_y)$ and zero elsewhere. Here Δz is the size of the defect in the z direction and k_d is the thermal conductivity of the defect.

At this step, the temperature and the thermal flux have to be replaced by their series expressions, Eq. (2.4.14), in all continuity conditions. The set of continuity relations is then written as a linear system of equations after the application of the Galerkin variant of the Method of Moments [103]. The result can be written in matrix form as

$$[\mathbf{A}][\mathbf{X}] = [\mathbf{B}] \tag{2.4.25}$$

where $\mathbf{X}$ contains the unknown coefficients $C_{mn}^{(j)}$ and $D_{mn}^{(j)}$. The matrix $\mathbf{A}$ has to be numerically inverted in order to calculate the unknown coefficients. The inversion of this matrix is what makes the TREE method a semi-analytical one and not analytical. The matrix in the right-hand side of the system, $\mathbf{B}$, is quite sparse as it differs from zero only in the lines which correspond to interfaces where sources may be found, excitations or delamination. By calculating the matrix $\mathbf{X}$ the solution of the problem can be numerically evaluated in the discretised space domain of interest using Eq. (2.4.14). This result is the solution of the problem in the Laplace domain. The temperatures can be calculated in the time domain, with numerical inversion of the obtained solution.

For the inverse Laplace transformation the Stehfest algorithm [104, 105] has been used, which is an improved variant of Gaver's method [106]. The methods is described in detail in appendix B.

2.5 Validation of the assumption made on the delamination thickness

In this section, the validity domain of the approximation for the flaw, which was assumed to be very thin, will be investigated. For the needs of this investigation, a set of different configurations has been modelled. For comparison, these configurations have been modelled using the developed TREE model and a numerical model based on the finite integral technique (FIT) [59, 107, 108]. The general configuration concerns double-layer metallic plate models with an embedded flaw, infinite in the x– and y–directions and parallel to the surface of the plate. Two different materials has been taken into account, namely aluminium as a high diffusive metal, corresponding to Fig. 2.5.1 and Fig. 2.5.2, and steel as a low diffusive metal, corresponding to Fig. 2.5.3 and Fig. 2.5.4. The temperature field has been simulated in reflection and transmission. The relative error of the simulated signals has been calculated and is shown in the following figures. The relative error is displayed as a function of the plate and flaw thicknesses. The flaw thickness is given as a percentage of the plate thickness and its depth as well. The values used for the configurations are given in Table 2.5.1. In the following figures, relative error contours are shown corresponding to the four different flaws' depths in each sub-figure.

Plate thickness [mm]	1.0, 1.5, 2.0, 2.5, 3.0, 3.5, 4.0, 5.0, 6.0
Defect thickness	1% to 10% of the plate thickness
Defect depth	10%, 30%, 50%, 70% of the plate thickness

Table 2.5.1: Parameters used for the investigation of the validity domain of the assumption made on the delamination thickness.

The four contour plots shown in Fig. 2.5.1 correspond to the case where an aluminium plate and signals in reflection are used. The error depends on the plate thickness and the flaw depth. The error is increasing as the depth of the flaw is increasing wherein the bottom right sub-figure the error is the largest one. However, there is no link between the error and the flaw thickness.

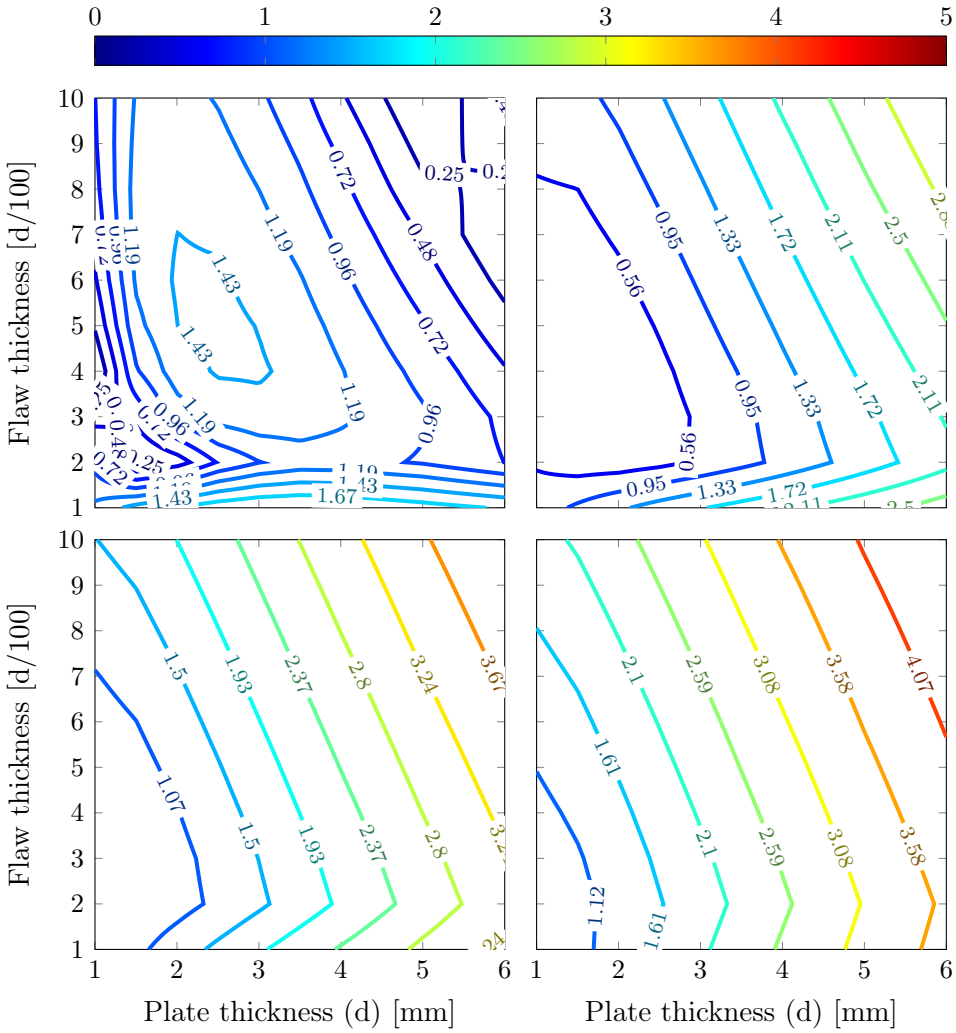

Figure 2.5.1: Relative error [%] of the approximation for recorded signals in reflection as a function of plate thickness and flaw thickness. Aluminium plate with embedded delamination at different depth: *Top left:* 10%(d), *Top right:* 30%(d), *Bottom left:* 50%(d), *Bottom right:* 70%(d).

Considering the relative error for the same configuration but using sim-

ulated signals in transmission, results are shown in Fig. 2.5.2. The relative error, in this case, is consistent with the flaw's depth and plate's thickness. Its maximum is much lower than previously and its dependence is only on the flaw thickness.

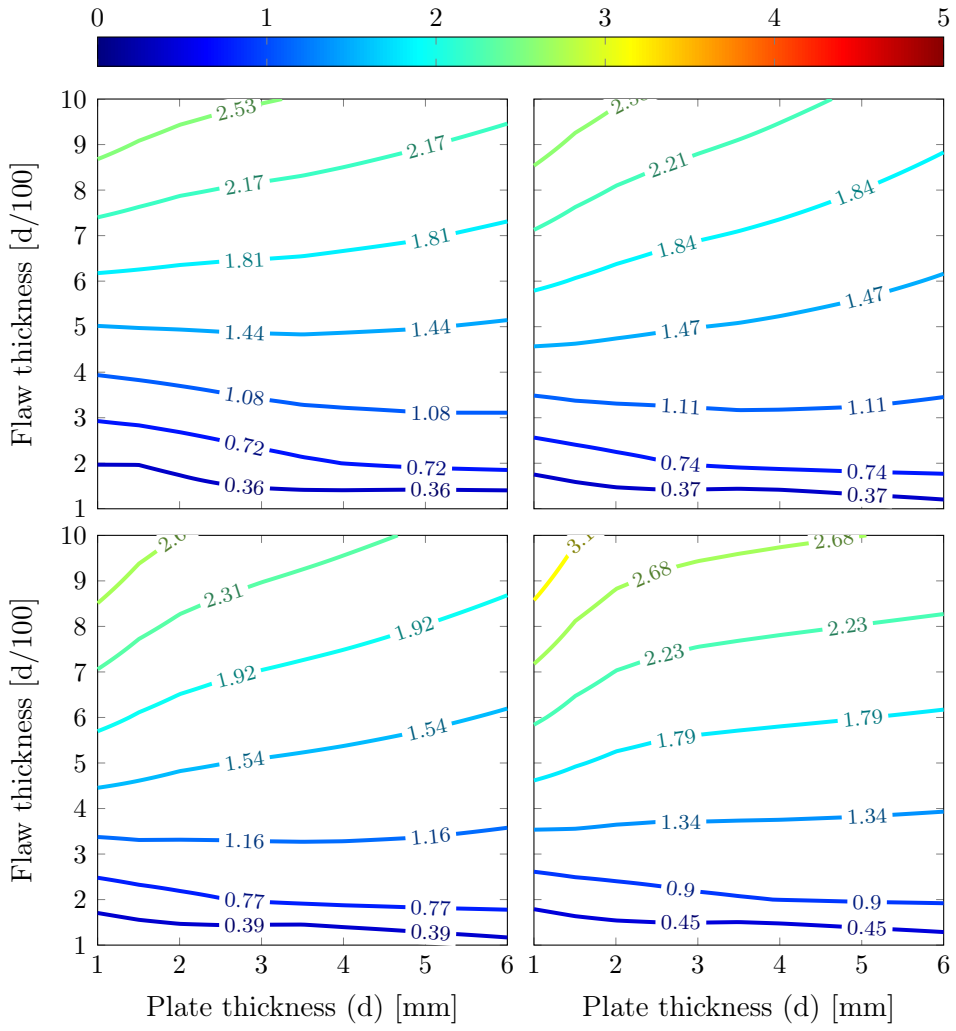

Figure 2.5.2: Relative error [%] of the approximation for recorded signals in transmission as a function of plate thickness and flaw thickness. Aluminium plate with embedded delamination at different depth: *Top left:* 10%(d), *Top right:* 30%(d), *Bottom left:* 50%(d), *Bottom right:* 70%(d).

Using signals in reflection for a steel plate, Fig. 2.5.3, one can see that the relative error increases with the plate thickness and the flaw depth as well.

This result agrees also with Fig. 2.5.1 where an aluminium plate was used. The difference here is that the error is slightly larger, yet, practically acceptable. In the cases where the flaw thickness is less than 2% of the plate thickness,

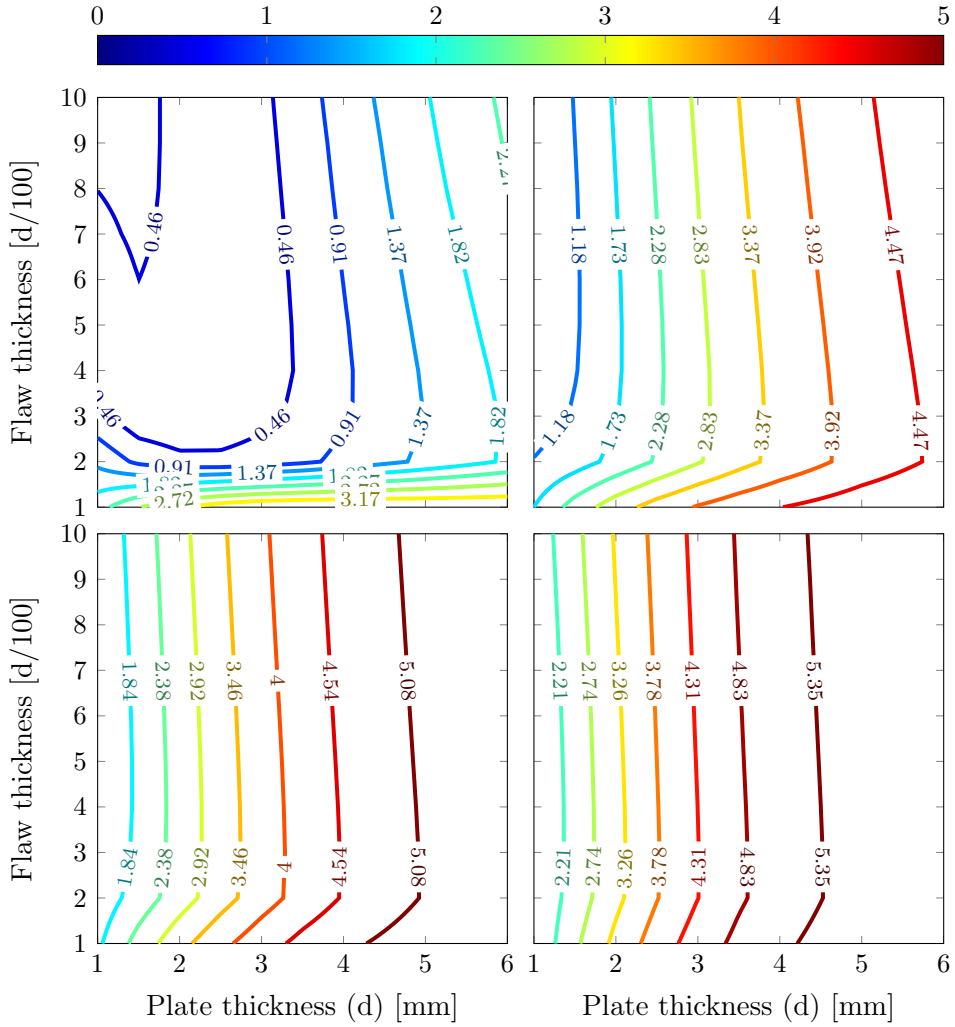

Figure 2.5.3: Relative error [%] of the approximation for recorded signals in reflection as a function of plate thickness and flaw thickness. Steel plate with embedded delamination at different depth: *Top left:* 10%(d), *Top right:* 30%(d), *Bottom left:* 50%(d), *Bottom right:* 70%(d).

the discrepancy between the results obtained from the two methods does not follow the trend of the error when the plate thickness is greater than 2% of the plate thickness. This may be due to discretization issues on the FIT model

and seems to be independent from the material.

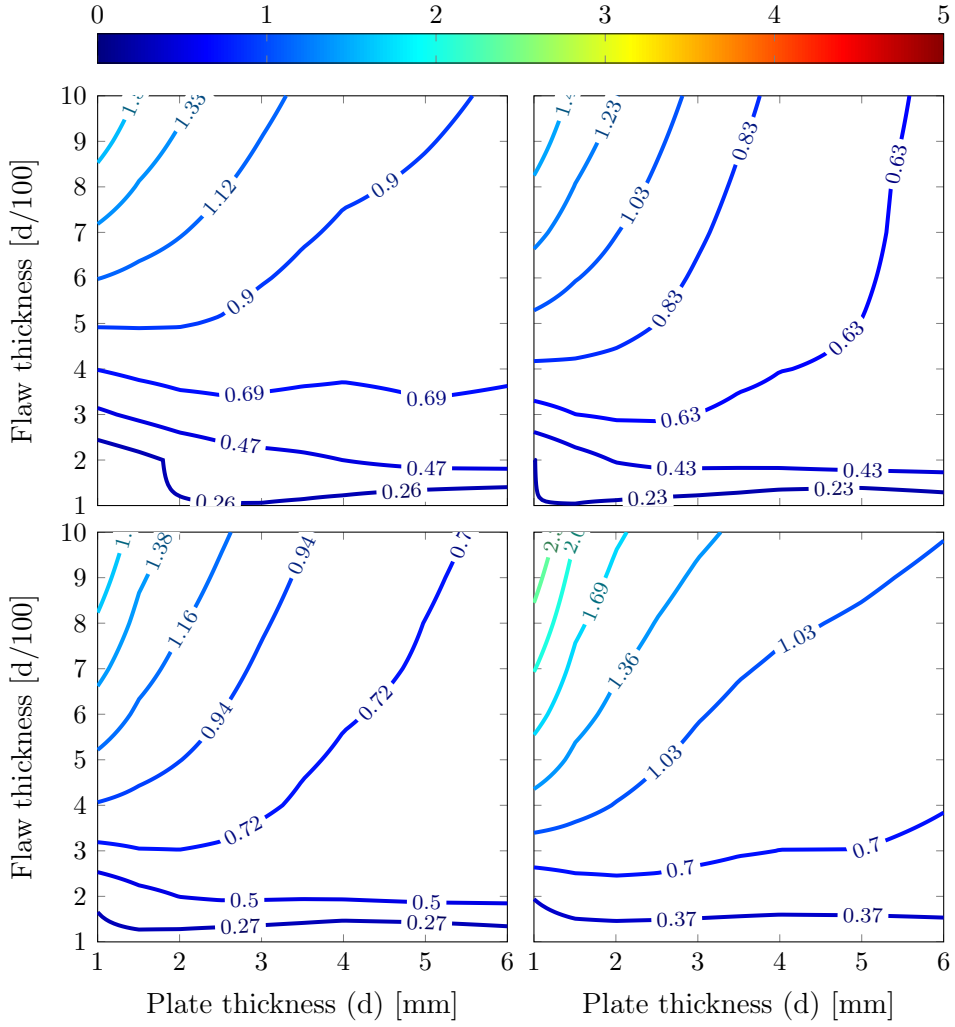

Figure 2.5.4: Relative error [%] of the approximation for recorded signals in transmission as a function of plate thickness and flaw thickness. Steel plate with embedded delamination at different depth: *Top left:* 10%(d), *Top right:* 30%(d), *Bottom left:* 50%(d), *Bottom right:* 70%(d).

The relative error in the simulated signals in transmission, in the case of the steel plate, appears to be very low as shown in Fig. 2.5.4. Its dependence on the flaw's thickness is not clear any more. However, its relation with the plate's thickness and flaw's depth agrees with the results shown for the aluminium plate.

In conclusion, the model produces accurate results despite the assumption made on the delamination thickness. The relative error is consistent in the tested cases and acceptable in the field of application.

2.6 Summary

In this chapter, a semi-analytical model based on the so-called truncated region eigenfunction expansion method, for the simulation of the thermographic inspection was proposed. The problem was solved in the Laplace domain with respect to time, and the temperature distribution was approximated by its expansion on a tensor product basis. Configurations addressed by this model were stratified planar pieces affected by thin delamination flaws. Considered sources are lamps providing a thermal excitation at the surface of the inspected piece. The thermal excitation at the surface of the layered media was provided by a flash lamp which is used in a wide range of applications. The description of the delamination defects as thin air gaps between the piece layers proves to be equivalent with the introduction of surface resistance to the heat flow, thus allowing their treatment via the applied modal approach without additional discretisation.

Chapter 3

Defect detection and characterisation

A typical thermal non-destructive thermographic (TNDT) procedure results in a sequence of infrared (IR) images, obtained via an infrared camera, which reflects the evolution of temperature in time. Mathematically, such a sequence can be regarded as a three-dimensional matrix of temperature, with the dimension being space and time. This recorded thermal response, usually, is degraded because of several factors. Uneven heating, variations of emissivity on the observed surface, optical distortions and noises of multiple nature significantly decrease the quality of the obtained thermal images. These factors limit the potential sensitivity of any method. The goal of data processing in TNDT is to reduce the amount of noise in thermal images and local storage requirements while improving discontinuity visibility.

Data processing algorithms in TNDT are either one-dimensional, being applied to pixel-based temperature evolutions in time, or two-dimensional, being applied to single images (snapshots). Single IR images are normally filtered or segmented to reduce random noise or to analyse geometrical features of the areas of interest. Much more information about defect parameters can be obtained by analysing the evolution of temperature in time. Therefore,

most TNDT processing algorithms use pixel-based functions.

In this chapter techniques and methods used for the detection and the characterisation of abnormalities in planar media will be presented.

3.1 Thermographic signal reconstruction.

Since its introduction [109], the thermographic signal reconstruction (TSR) method has emerged as one of the most widely used methods for enhancement, analysis and compression of raw thermographic sequences. The technique was originally developed for pulse thermography to improve contrast results. The process separates temporal and spatial noise components in the image sequence and significantly reduces temporal noise. The technique consists of two basic steps. First step is the fitting of the experimental thermogram in the log-log space by a logarithmic polynomial of degree n. This step provides a significant compression of the raw data. In a later step, the reconstruction of the temperature signals in the logarithmic domain using the polynomial has to be performed, providing noise-reduced replica of each pixel time history. The enhancement of the images is provided by the computation of the 1st and 2nd logarithmic time derivatives of the thermograms. Fitting to the thermograms highly depends on the time window chosen. Thus, the choice of the time window has to be defined with the objective to consider only the part of the thermograms influenced by the physical phenomena to characterize. Even though TSR is a pixel-based technique, unlike other techniques, it does not require any reference pixel.

In the literature there are many variations of the TSR method, with the "classic" one selecting the best, under some criteria, derivative images associated with every given depth range. These images are used either to qualitatively detect the defects or to quantitatively evaluate their depths from characteristic times. In Fig. 3.1.1 the basic stages of the TSR method for the

two most used variations are shown.

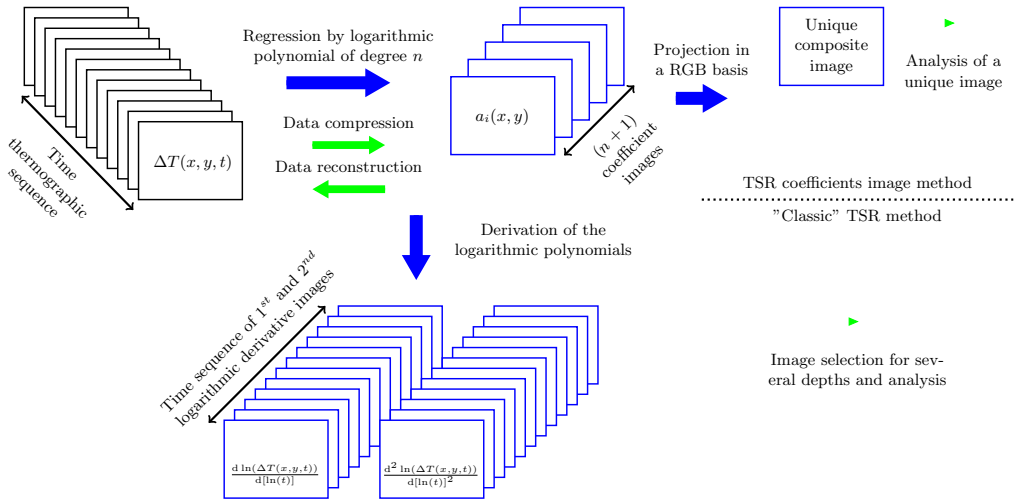

Figure 3.1.1: Defect detection by the TSR method.

3.1.1 Classic TSR

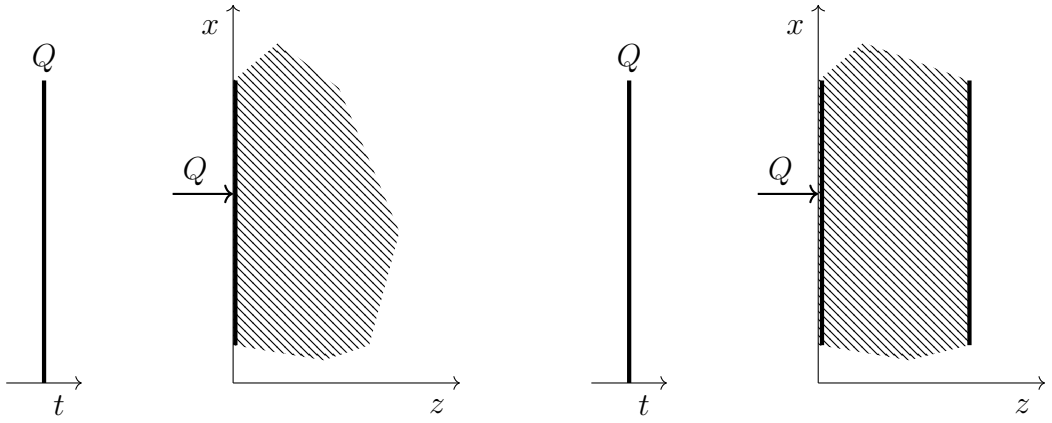

(a) Dirac pulse heating of an adiabatic semi-infinite body.

(b) Dirac pulse heating of an adiabatic plate.

Figure 3.1.2: One-dimensional heat diffusion.

In principle, the method exploits the well-known observation that in a semi-infinite flawless sample, or in a very thick slab, Fig. 3.1.2a, the surface temperature response to instantaneous uniform heating is described by the

one-dimensional heat diffusion equation:

$$\frac{\partial T}{\partial t} = \alpha \frac{\partial^2 T}{\partial z^2} \tag{3.1.1}$$

where $\alpha = \frac{\kappa}{\rho c}$ is the thermal diffusivity of the material with the solution

$$T(z,t) = \frac{Q}{\epsilon\sqrt{\pi t}} e^{\frac{z^2}{4\alpha t}} \tag{3.1.2}$$

at distance z from its surface, where $\epsilon = \sqrt{\kappa\rho c}$ is the heat effusivity and Q is the energy supplied to the surface. From Eq. (3.1.2) one has the temperature increase ΔT (thermogram) as a function of time t at the surface:

$$\Delta T(t) = \frac{Q}{\epsilon\sqrt{\pi t}}. \tag{3.1.3}$$

The one-dimensional approximation of Eq. (3.1.3) assumes that the lateral diffusion components more or less cancel in a defect-free sample. However, in the presence of an adiabatic subsurface boundary such as a void or a wall, Fig. 3.1.2b, the incident heat flow from the sample surface is impeded, and this description no longer applies locally. The effect of a wall is shown in Fig. 3.1.3a where the surface temperature for a semi-infinite sample is compared with the case of the presence of an adiabatic wall at three different depths.

The defect's identification lies in the fact that the one-dimensional assumption is not valid any more if a defect is present. In general, the separation of the temperature response at the surface of a solid between a sound area and a defected area, during the cooling process, should be simple when these defects are large or very close to the surface, as shown in Fig. 3.1.3b. However, when one attempts to detect small buried defects, the effects of IR camera noise as well as the randomness or the complexity found in many samples, complicate and limit the ability to discriminate between sound areas and boundaries.

Additional insight into the surface temperature response to pulsed heating

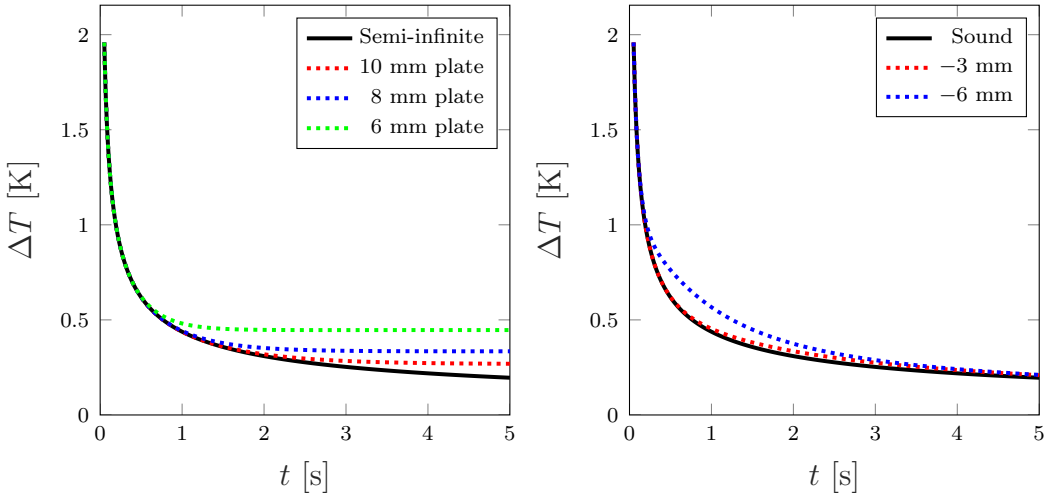

(a) Comparison of temperature time plot of a semi-infinite sample with three adiabatic samples of different thickness.

(b) Comparison of temperature time plot of a sound sample with two defected samples at different depth.

Figure 3.1.3: Surface temperature decay curves for a single point of a steel plate.

is gained by considering the time evolution of the surface temperature in the logarithmic domain. Equation (3.1.3) can be written in the logarithmic scale as

$$\ln(\Delta T) = \ln\left(\frac{Q}{\epsilon\sqrt{\pi}}\right) - \frac{1}{2}\ln(t)\,. \tag{3.1.4}$$

This representation is very significant from many aspects. The time dependence has been separated from the input energy and material properties. Only the offset of the response will change as the sample material and the input energy vary.

For a semi-infinite solid, Eq. (3.1.4) describes a straight line with slope equal to $-1/2$, as pictured in Fig. 3.1.4a. In the case of a plate, the response deviates from the straight line at a particular time. This particular time is correlated to the thickness of the plate. In the presence of a subsurface defect in a plate, or in a semi-infinite solid, the time evolution plot of the temperature corresponding to those pixels depart from that behaviour in a particular time

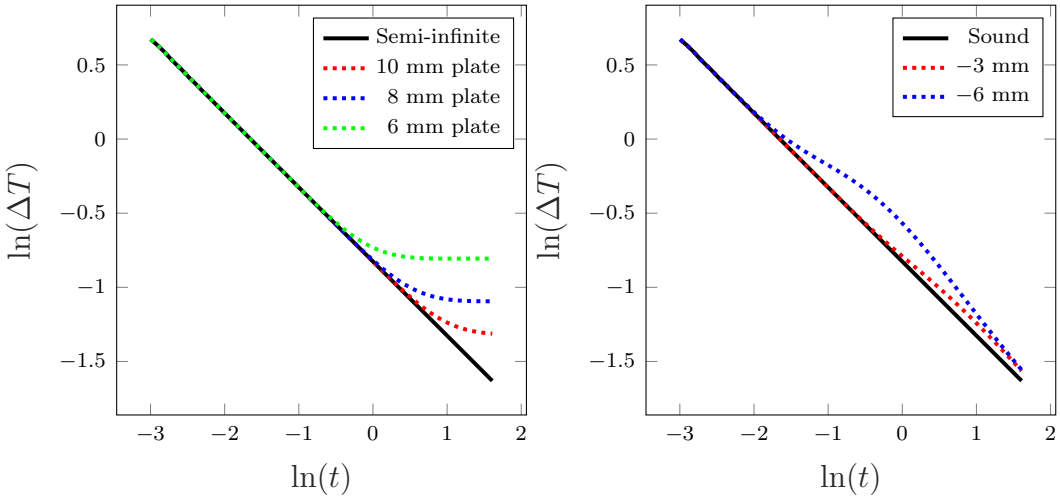

(a) Comparison of temperature time plot of a semi-infinite sample with three adiabatic samples of different thickness in the logarithmic space.

(b) Comparison of temperature time plot of a sound sample with two defected samples at different depth in the logarithmic space.

Figure 3.1.4: Regression by a logarithmic polynomial of degree n equal to 7 and 17, for a sound and a damaged zone.

but in a different way comparing to the case of the adiabatic flaw-free plate, as shown in Fig. 3.1.4b. In Fig. 3.1.4a and Fig. 3.1.4b, the thermograms have been normalised based on Eq. (3.1.4) where the term which describes the source and the material effect have been removed.

Noise reduction and data compression

For a given position, the response given by Eq. (3.1.4) can be approximated by a function or set of orthogonal functions. In this case a polynomial series will be used to fit the experimental data in log-log space:

$$\ln\left(\Delta T\right) = \sum_{n=0}^{N} a_n \left[\ln(t)\right]^n . \tag{3.1.5}$$

The fitting of the log-log thermogram, for each pixel (i, j), by the logarithmic polynomial replaces the full sequence of the temperature images $T(i, j, t)$

by the series of $(n+1)$ images of the polynomial coefficients: $a_0(i,j), \cdots, a_n(i,j)$.

Once the time evolution of each pixel has been approximated by Eq. (3.1.5), the original data can be reconstructed as:

$$\Delta T = \exp\left(\sum_{n=0}^{N} a_n \left[\ln(t)\right]^n\right). \tag{3.1.6}$$

Thus, it is only necessary to save the polynomial coefficients a_n and reconstruct the images stack at required time samples. This approach provides a significant degree of data compression. An high-speed IR camera produces images with a frame rate up to 1kHz, *i.e.* 1000 images per second, while the polynomial degree used for the regression is lower than 15 for the whole recorded image sequence.

A low–degree polynomial expansion is applied usually to serve as a low–pass filter. Thus, this approximation preserves the essential thermal response, while rejecting non–thermal noise contributions. The use of higher-order polynomials reproduces the original data and replicates also part of the noise that appears in the later, low–amplitude data. In Fig. 3.1.5 reconstructed noisy signals by using polynomial degrees $n = 7$ and 17, with and without the presence of a defect, are compared.

Logarithmic Derivatives and Signal Enhancement

As shown, the use of TSR removes effectively the temporal noise from the recorded raw data. However, the reduction of temporal noise does not necessarily increase the flaw detectability, which is more related to the contrast between the signal and background. This contrast not only depends on the instrumentation and the experimental conditions but also on the relative properties of the flaw and the host material. This can be partially addressed by the computation of the first and second time derivatives, using Eq. (3.1.5),

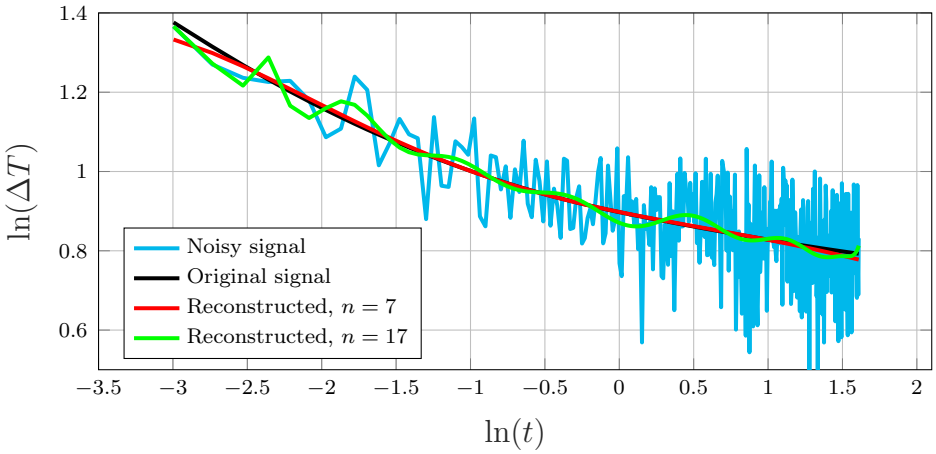

(a) Polynomial regression for a sound area.

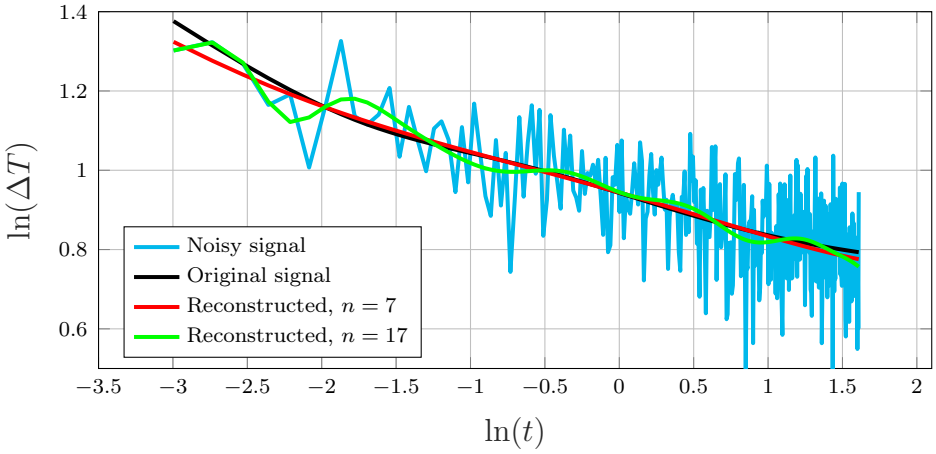

(b) Polynomial regression for a flawed area.

Figure 3.1.5: Regression by a logarithmic polynomial of degree n equal to 7 and to 17, for a sound area and a flawed area.

without additional noise contributions, which leads to equations

$$\frac{\mathrm{d}\ln(\Delta T)}{\mathrm{d}[\ln(t)]} = \sum_{n=1}^{N} n a_n [\ln(t)]^{n-1} \tag{3.1.7}$$

$$\frac{\mathrm{d}^2\ln(\Delta T)}{\mathrm{d}[\ln(t)]^2} = \sum_{n=2}^{N} n(n-1) a_n [\ln(t)]^{n-2} \tag{3.1.8}$$

for the first and the second derivative, respectively. The temperature in the logarithmic scale has been compared with the first and the second time deriva-

tive for a sound area and a flawed area in Fig. 3.1.6.

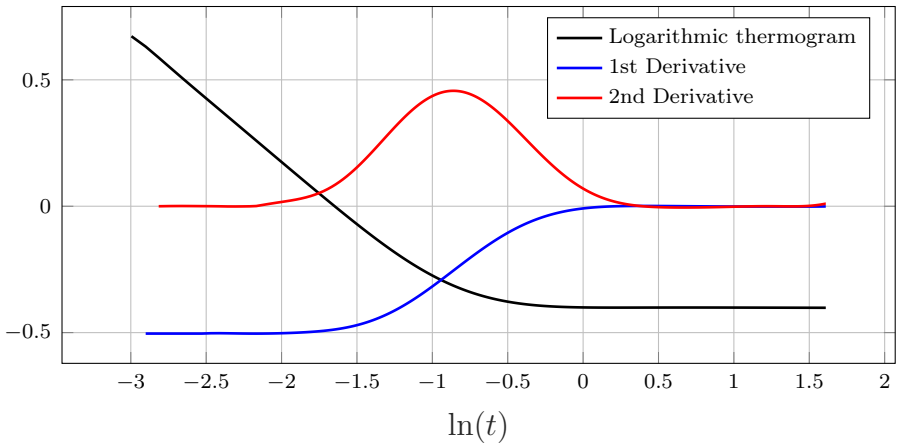

(a) Sound area.

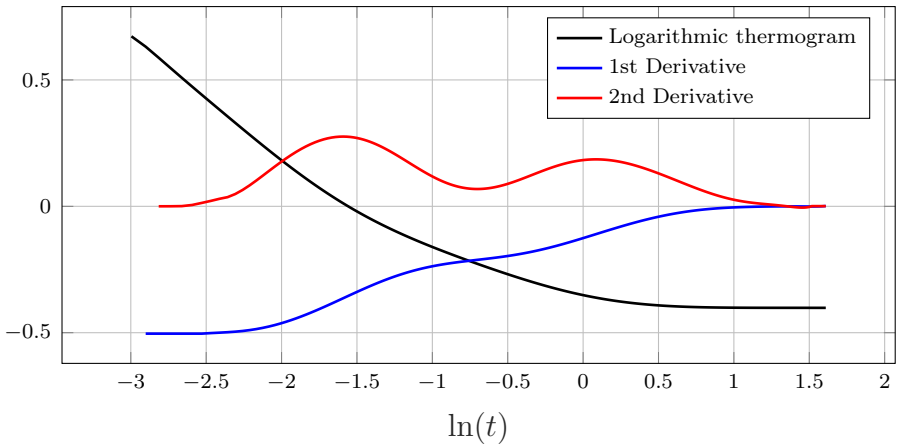

(b) Damaged area.

Figure 3.1.6: 1st and 2nd derivatives for a thick steel plate, with and without flaw.

Moreover, the reconstructed images suffer from diffusion blurring. The peaks in the derivative signals always occur before the contrast peak in the temperature–time image signal, as depicted in Fig. 3.1.7. Maximum contrast can be obtained earlier for derivative images compared to conventional images because the ascending inflexion point in the temperature-time evolution of a pixel corresponds to a maximum in the time evolution of the first time derivative, and the ascending inflexion point of the first derivative corresponds

to a maximum in the second derivative time evolution. The derivative images provide earlier indications of the presence of a subsurface defect than normal contrast images of the same target and this leads to significant reduction of diffusion blurring.

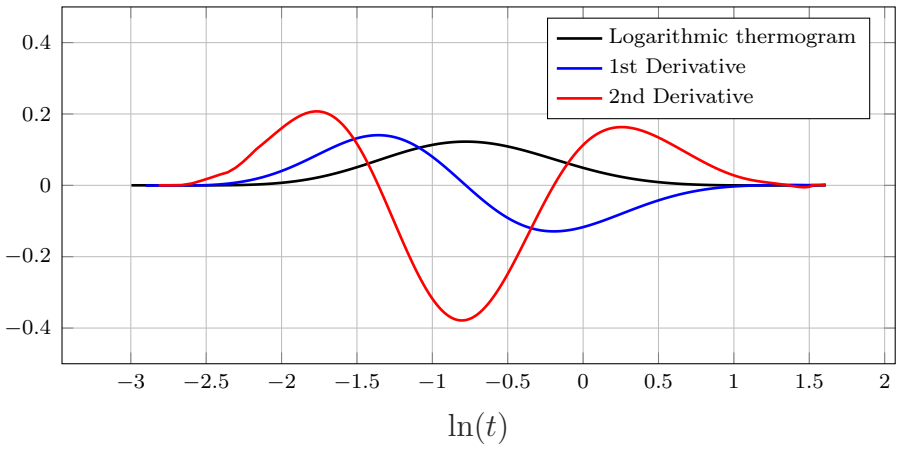

(a) Contrast

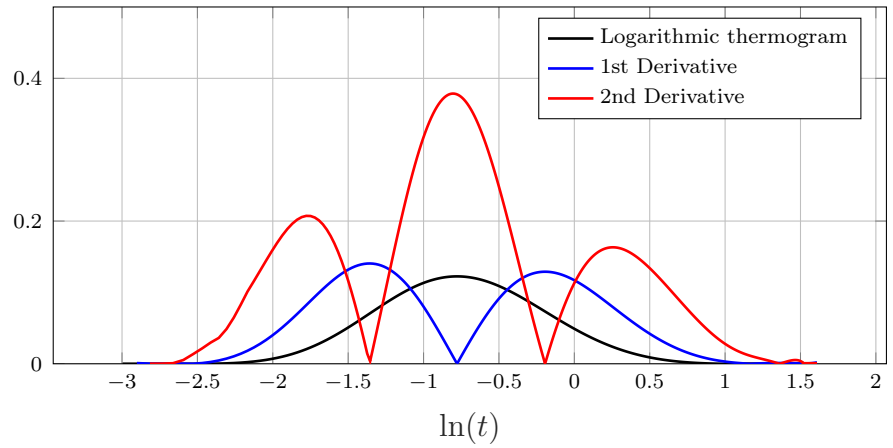

(b) Absolute contrast.

Figure 3.1.7: Contrast curves for a damaged area.

The denoising provided by TSR is not limited to the time signals but has been partially transmitted to the spatial signals also, this is an indirect effect. The derivatives, by definition, are much more sensitive to small changes in amplitude than the raw signal. However, after the application of the TSR that acts as a low-pass filter, the derivatives are less sensitive to random sig-

nal fluctuations. In Fig. 3.1.8 the temperature of the raw signals versus the horizontal position plot of the steel defect sample and the TSR first derivative are compared.

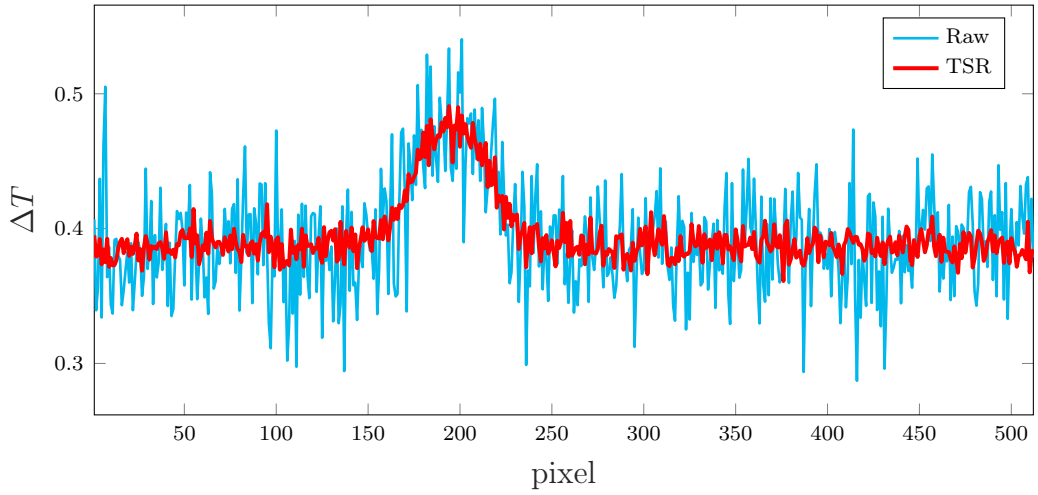

(a) Comparison of raw signals and TSR.

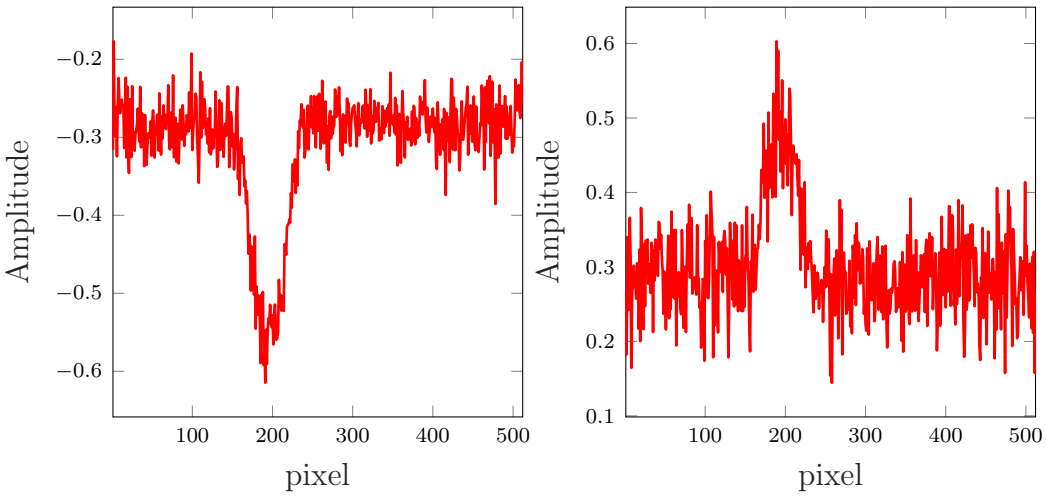

(b) TSR 1st derivative for the same line. **(c)** TSR 2nd derivative for the same line.

Figure 3.1.8: Comparison of raw and TSR results for a horizontal line through the centre row of delamination.

The derivative signals have been partially denoised by TSR, too. The high sensitivity of the derivatives to small changes makes them ideal for the detection of features that can be undetectable in the original data. Comparing

now images obtained from TSR, first and second derivatives, Fig. 3.1.9, it is obvious that the images are sharper and the detectability of small flaws has been significantly improved.

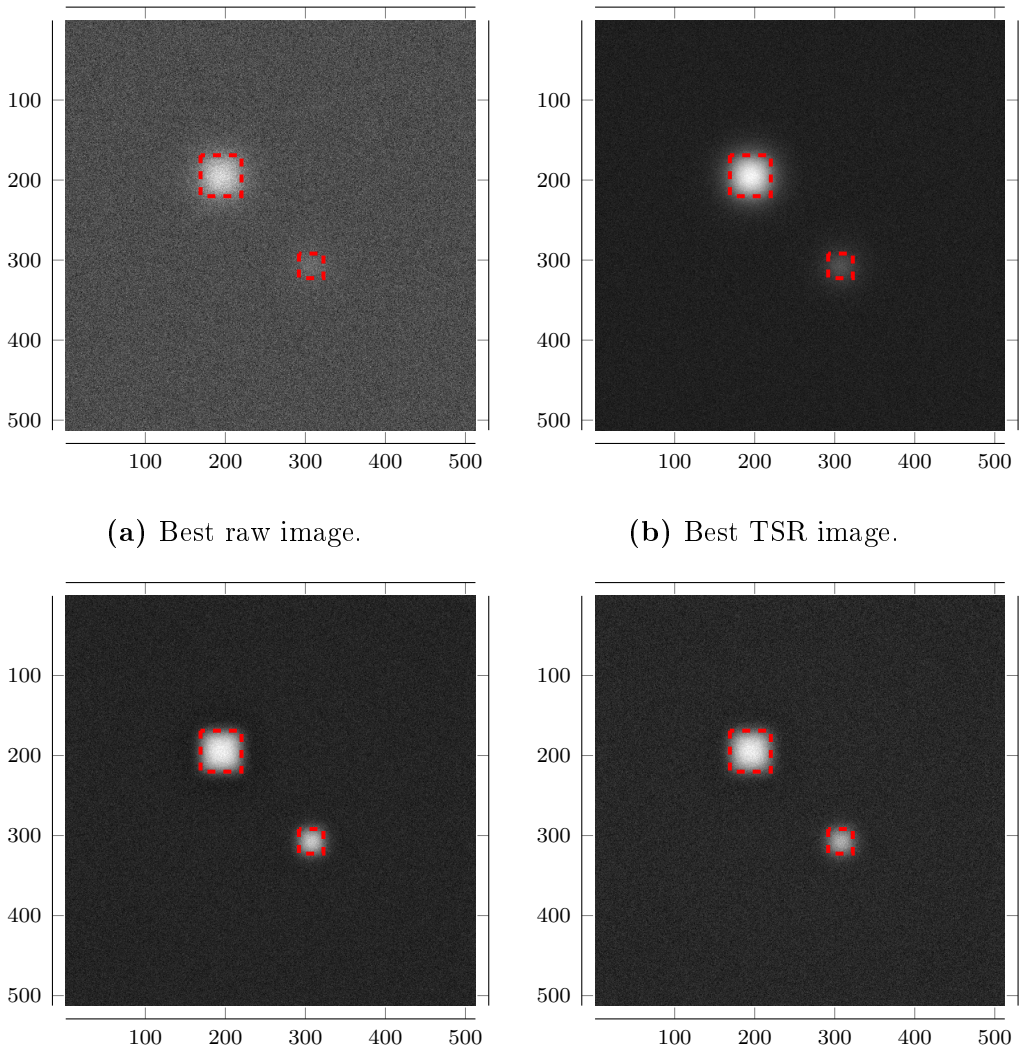

(a) Best raw image.

(b) Best TSR image.

(c) Best 1st derivative image.

(d) Best 2nd derivative image.

Figure 3.1.9: Comparison of raw, TSR, 1st and 2nd derivative images.

3.1.2 TSR-based method

As long as detection only is aimed at and no identification of the depth of the defects is required, a new TSR-based method can answer with success. In the

"classic TSR" method, as explained before, all the information needed for the defect detection is stored in the coefficients of the fitted polynomials which are used to reproduce the signals and their time derivatives images. The new TSR-based method uses the original method as a basic pre-processing operation to compute and store the coefficients of the fitted logarithmic polynomials. Instead of using these coefficients to reproduce the signals or their time derivatives, images are formed for each monomial. In a second step, only the three best images, out of $n+1$ images for a polynomial of degree n, are selected and projected into an RGB basis to form a unique composite image. This representation makes easier the detection of defects located at different depths using one single image. In the "classic TSR", however, one has to go through all observation times to choose the best-produced image or images.

Like in all TSR–based approaches, the choice of the observation time window and the degree of the polynomial are very crucial. It is shown that a polynomial of degree 11 fits very well the data for time analysis of logarithmic images but for defect imaging and detection a polynomial of degree 5 to 8 can be considered as optimal, see Appendix D. For the results shown in Fig. 3.1.10, a polynomial of degree $n = 7$ is used. The best images, in this case, were found to be those corresponding to monomials $7, 6$ and 5, shown in Figs. 3.1.10a to 3.1.10c and used to produce the composite RGB image Fig. 3.1.10d.

3.2 Edge detection and shape reconstruction

3.2.1 The Canny algorithm

One of the well-established edge-detection algorithms is the so-called Canny algorithm [110]. Because of a better signal to noise ratio and detection accuracy, the Canny operator becomes the evaluation criterion of other methods. The algorithm consists of Gauss filtering, gradient calculation, non-maximum

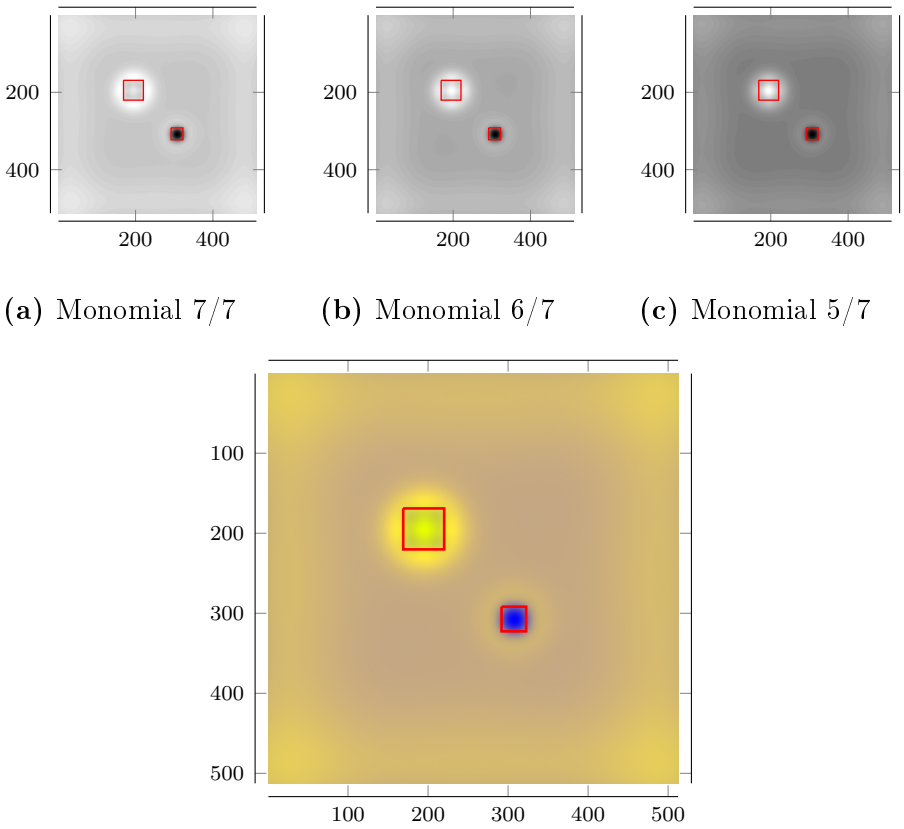

(a) Monomial 7/7 **(b)** Monomial 6/7 **(c)** Monomial 5/7

(d) Monomials 7/7,6/7,-5/7

Figure 3.1.10: *First row:* grey level images (256 bits) of individual component. *Second row:* RGB projection of these components.

suppression, double thresholding, checking the edges and connecting the edges.

Gaussian filtering and gradient computation In its classical form, the Canny algorithm processes the image smoothly through Gaussian convolution and obtains the gradient image through differential operation to the image which is processed via Gaussian convolution. Consider the two-dimensional Gaussian function:

$$G(x,y) = \frac{1}{2\pi\sigma^2} \exp\left(-\frac{x^2+y^2}{2\sigma^2}\right) \tag{3.2.1}$$

with mean $\mu = 0$ and standard deviation σ. The parameter σ is the width of the Gaussian filter and directly determines the effect of filtering. The filtered image is derived from the convolution

$$\widehat{\mathcal{I}}(x, y) = G(x, y) * \mathcal{I}(x, y) \tag{3.2.2}$$

where $\mathcal{I}(x, y)$ is the original image matrix. Making use of Gaussian function's separability, ∇G can be decomposed to two one-dimension filters:

$$\frac{\partial G}{\partial x} = kx \exp\left(-\frac{x^2}{2\sigma^2}\right) \exp\left(-\frac{y^2}{2\sigma^2}\right) \tag{3.2.3a}$$

$$\frac{\partial G}{\partial y} = ky \exp\left(-\frac{y^2}{2\sigma^2}\right) \exp\left(-\frac{x^2}{2\sigma^2}\right). \tag{3.2.3b}$$

By convolving these equations with the image we obtain:

$$L_x = \frac{\partial G}{\partial x} * \mathcal{I}(x, y), \quad L_y = \frac{\partial G}{\partial y} * \mathcal{I}(x, y) \tag{3.2.4}$$

where in a matrix representation this can be written as:

$$L_x = K_x * \mathcal{I}(i, j), \quad L_y = K_y * \mathcal{I}(i, j) \tag{3.2.5}$$

where i and j are the coordinates of a pixel in the image.

This is a way to compute the gradient, but not the only one. Different kernels can be used to calculate the image gradient. This could separate the denoising part of the algorithm from the computation of the gradient. For the traditional Canny algorithm, two 2×2 convolution operators K_x and K_y are deployed to calculate the image gradient in the x and y directions, respectively. These operators are written as:

$$K_x = \begin{bmatrix} 1 & -1 \\ 1 & -1 \end{bmatrix}, \quad K_y = \begin{bmatrix} 1 & 1 \\ -1 & -1 \end{bmatrix}. \tag{3.2.6}$$

The angle accuracy of the computation of the gradient can be improved by using 3×3 or 5×5 truncated area sampled Gaussian derivatives, Eq. (3.2.3), as the Scharr kernel:

$$K_x = \begin{bmatrix} 47 & 0 & -47 \\ 162 & 0 & -162 \\ 47 & 0 & -47 \end{bmatrix}, \quad K_y = K_x^T. \tag{3.2.7}$$

or the proposed [111] Gaussian derivative with optimized sigma $\sigma = 0.6769$

$$K_x = \begin{bmatrix} 0.0007 & 0.0037 & 0 & -0.0037 & -0.0007 \\ 0.0052 & 0.1187 & 0 & -0.1187 & -0.0052 \\ 0.0370 & 0.2589 & 0 & -0.2589 & -0.0370 \\ 0.0052 & 0.1187 & 0 & -0.1187 & -0.0052 \\ 0.0007 & 0.0037 & 0 & -0.0037 & -0.0007 \end{bmatrix}, \quad K_y = K_x^T. \tag{3.2.8}$$

which gives a minimal angle error.

In general, 2×2 or 3×3 kernels based on finite differences are used for the computation of the gradient. These kernels perform well in not challenging situations. In the literature one can find many other derivative kernels which provide also some smoothing in the data, with the most used ones being the Sobel operator:

$$K_x = \begin{bmatrix} 1 & 0 & -1 \\ 2 & 1 & -2 \\ 1 & 0 & -1 \end{bmatrix}, \quad K_y = K_x^T \tag{3.2.9}$$

the Roberts operator:

$$K_x = \begin{bmatrix} 1 & 0 \\ 0 & -1 \end{bmatrix}, \quad K_y = K_x^T \tag{3.2.10}$$

and the Previtt kernel:

$$K_x = \begin{bmatrix} 1 & 0 & -1 \\ 1 & 0 & -1 \\ 1 & 0 & -1 \end{bmatrix}, \quad K_y = K_x^T. \tag{3.2.11}$$

After convolution of the image with the kernels, the gradient-component intensity of the image is derived from:

$$M(i,j) = \sqrt{L_x^2(i,j) + L_y^2(i,j)} \tag{3.2.12}$$

and its normal vector direction at the pixel (i,j) is defined as:

$$\theta(i,j) = \arctan\left[\frac{L_x(i,j)}{L_y(i,j)}\right]. \tag{3.2.13}$$

Non-maximum suppression To follow, after smoothing the image using Gaussian smoothing and convolving it with derivative kernels, we end up with the gradient magnitude image $M(i,j)$ which reflects the edge intensity at the pixel(i,j) and $\theta(i,j)$, which reflects the normal vector at the pixel (i,j) in the image. Edges of objects can be extracted from the gradient component intensity image but they will be quite blurry. In this step, the algorithm aims at thinning those edges by setting the pixels around local maxima in the gradient image M to 0.

Firstly, the direction angle is rounded to $0°, 45°, 90°, 135°$ for the relative position in adjacent pixels of the image. Aiming at every pixel whose value is non-zero, the gradient-component intensity of a candidate pixel $M(i,j)$ is compared with two adjacent pixels along the rounded direction angle. The candidate pixel is preserved only if its gradient component intensity is the largest. Otherwise, it is set to zero. Let the processed image be $\widehat{M}(i,j)$.

Thresholding The non-maximum suppression gives the non-zero pixels providing more accurate approximation regarding the edges of the objects in the processed image $M(i,j)$. These pixels are taken as the edge pixels. Due to noise in the original image, $\widehat{M}(i,j)$ contains pixels depicting false edges, the spurious edge response. To mitigate these spurious edges, hysteresis tracking is performed using dual thresholding by setting a high τ_h and a low τ_l threshold parameter. Edge pixels which have gradient larger than τ_h are added automatically to the final binary image and are considered as strong edge pixels. In opposition, edge pixels with a gradient lower than τ_l are considered as phantom edges and are discarded. The remaining pixels with a gradient value between τ_l and τ_h are considered as weak edges and are added to the final binary image only if they are connected with a strong edge pixel. When none of the 8-connected neighbourhood pixels is a strong pixel, the candidate pixel is suppressed.

The choice of thresholds is very crucial for the success of the method. The algorithm can wipe off most of the spurious edges while increasing the value of τ_h, but meanwhile, some edges may be missed. On the other hand, by decreasing the value of τ_l more information about the edges will be preserved but by the contrary, the edge's characteristic will become less and less at the point where the true edges will be missed. Auto-select thresholding value is a difficult task. At present, there are many kinds of methods in selecting threshold values. The more widely used is the Otsu method [112] but also other methods based on histogram, maximum entropy, or statics are used [113, 114, 115].

The Otsu method has the best threshold value in the statistical sense and is the most stable method in the image threshold segmentation. The method has been used here to choose the value of τ_h automatically. The method assumes that the pixels of the image to be thresholded can be separated into two classes, *e.g.* foreground and background, then calculates the optimum thresh-

old separating those two classes so that their combined spread is minimal.

Suppose that $G = [0, L-1]$ is the range of greyscale of in image F and P_i is the probability of every greyscale and the threshold value τ has splitted the image in two classes which are $C_0 = [0, \tau]$ and $C_1 = [\tau + 1, L-1]$. The two classes probabilities are

$$\alpha_0 = \sum_{i=0}^{\tau} P_i$$

and

$$\alpha_1 = 1 - \alpha_0$$

respectively. The average grey values of the two classes are

$$\mu_0 = \sum_{i=0}^{\tau} \frac{iP_i}{\alpha_0} = \frac{\mu_\tau}{\alpha_0}$$

and

$$\mu_1 = \sum_{i=\tau+1}^{L-1} \frac{iP_i}{\alpha_1} = \frac{\mu - \mu_\tau}{1 - \alpha_0}$$

respectively, therein

$$\mu = \sum_{i=0}^{L-1} iP_i, \qquad \mu_\tau = \sum_{i=0}^{\tau} iP_i.$$

The criterion function has been defined as variance between the two classes, expressed as

$$\eta^2(\tau) = \alpha_0 (\mu_0 - \mu)^2 + \alpha_1 (\mu_1 - \mu)^2 \tag{3.2.14}$$

$$= \alpha_0 \alpha_1 (\mu_0 - \mu_1)^2 . \tag{3.2.15}$$

The optimal threshold value $\tau^\star$ is given by

$$\eta^2(\tau^\star) = \max_{0 \le \tau \le L} \eta^2(\tau). \tag{3.2.16}$$

Threshold $\tau^\star$ will be used as the high threshold parameter τ_h. The value of the low threshold τ_l, usually, is set to be $\tau_l = \frac{\tau_h}{2}$.

Edge linking The last step of the algorithm is the connection of already detected edges on the binary image under some restrictions. These restrictions are criteria set upon the gradient value $\widehat{M}(i,j)$ and the gradient angle $\theta(i,j)$ of the non-edge pixels between two edges. If the gradient is greater than a given value and the gradient angle is close to zero, the pixels between the two edges are added to the binary image.

The output of the Canny algorithm is a binary image which contains the edges of any present objects in the initial image. This binary image will be used as *a-priori* information in the next step of the defect characterisation.

3.3 Parameter estimation - Optimization

We will be seeking to characterize detected flaws which are described through some parameters. Hence, these parameters have to be estimated. A classical approach of parameter estimation has been taken in this thesis. For its completeness, the optimization method will be presented in this section.

3.3.1 The function to be minimized

In the inversion process, one usually minimizes a discrepancy between some experimental data, say u_d, and some model data, say u. The discrepancy function also called cost or objective function, is often expressed as a norm of the difference between u_d and u. Classically, one uses the $L_2(\cdot)$ norm if some continuous u and especially u_d are available. When the available data u_d are given only at specific locations, then the squared Euclidean norm is to be used:

$$||u - u_d||_2^2 := \sum_i \left(u^i - u_d^i\right)^2 = \int_{\mathcal{S}} \delta_i^j \left(u - u_d\right) \, \mathrm{d}s \tag{3.3.1}$$

where $\delta_i^j = d(x^i - x^j)$. In order to write down a general form for the cost function to be minimized, we use:

$$\mathcal{J} = f\left(||u - u_d||^2\right) \tag{3.3.2}$$

without specifying any choice of the norm. The norm $||\cdot||$ is squared so that the function $\mathcal{J}$ does not a priori present discontinuity. Regularization terms could be added to the cost function which would become:

$$\mathcal{J} = f\left(||u - u_d||^2\right) + g\left(||\psi||^2\right). \tag{3.3.3}$$

Therefore the cost function is explicitly given in terms of u, it is actually to be minimized with respect to what is searched, the parameters ψ. Hence we write the equality:

$$j(\psi) := \mathcal{J}(u) \tag{3.3.4}$$

where the function j is the so-called reduced cost function, as opposed to $\mathcal{J}$ which is the cost function.

3.3.2 Elements of minimization

The function denoted j is defined on $\mathcal{K}$ with values in $\mathbb{R}$. $\mathcal{K}$ is a set of admissible elements of the problem. In some cases, $\mathcal{K}$ defines some constraints on the parameters or functions. The minimization problem is written as:

$$\inf_{\phi \in \mathcal{K} \subset \mathcal{V}} j(\phi). \tag{3.3.5}$$

Using the notation "inf" for a minimization problem means that one does

know, a priori, if the minimum is obtained, *i.e.* if there exists $\phi \in \mathcal{K}$ such that:

$$j(\phi) = \inf_{\psi \in \mathcal{K} \subset \mathcal{V}} j(\psi).$$

To indicate that the minimum is obtained, one should prefer the notation:

$$\phi = \arg\min_{\psi \in \mathcal{K} \subset \mathcal{V}} j(\psi).$$

If j is a convex function in $\mathcal{K}$, the local minimum of j in $\mathcal{K}$ is the global minimum in $\mathcal{K}$.

3.3.3 Optimality conditions

For convex functions, there is no difference between local minima and global minimum. Thus, we are more interested in minimizing a function without specifying whether the minimum is local or global.

Let us derive here the minimization necessary and sufficient conditions. These conditions use the first-order derivatives (order-1 condition), and second-order derivatives (order-2 condition) on the cost function j. Using gradient-type algorithms, the first-order condition is to be reached, while the second-order condition leads to fix the convexity hypothesis, and then make a distinction between minima, maxima and optima.

Let us assume that $j(\psi)$ is continuous and has continuous partial first derivatives $\frac{\partial j(\psi)}{\partial \psi_i}$ and second derivatives $\frac{\partial^2 j(\psi)}{\partial \psi_i \partial \psi_j}$. Then the necessary condition for $\widetilde{\psi}$ to be a minimum, at least locally, of j is that:

(i) $\widetilde{\psi}$ is a stationary point, *i.e.* $\nabla j(\widetilde{\psi}) = 0$

(ii) the Hessian $\nabla^2 j(\widetilde{\psi}) = \frac{\partial^2 j(\psi)}{\partial \psi_i \partial \psi_j}$ is a positive semi-definite matrix, *i.e.*

$$\forall y \in \mathbb{R}^n, \left(\nabla^2 j(\widetilde{\psi}) y, y\right) \geq 0$$

where $(\cdot,\cdot)$ is a scalar product in $\mathbb{R}^n$ and $\dim(\psi) = n$.

A point $\widetilde{\psi}$ which satisfies condition (i) is called a stationary point. It is important to point out that stationarity is not a sufficient condition for local optimality. For instance, the point of inflexion for cubic functions would satisfy condition (i) while there is no minimum. Hence the Hessian is not positive-definite but merely positive semi-definite.

The sufficient condition for $\widetilde{\psi}$ to be a minimum of j is that

(i) $\widetilde{\psi}$ is a stationary point, *i.e.* $\nabla j(\widetilde{\psi}) = 0$

(ii) the Hessian $\nabla^2 j(\widetilde{\psi}) = \frac{\partial^2 j(\psi)}{\partial\psi_i \partial\psi_j}$ is a positive definite matrix, *i.e.*

$$\forall y \in \mathbb{R}^n, y \neq 0, \left(\nabla^2 j(\widetilde{\psi}) y, y\right) > 0.$$

3.3.4 Stopping criteria

Since the convergence of the iterative algorithms is, in general, not achieved in a finite number of iterations, a stopping criterion must be applied. Some commonly used criteria are given next. We denote ψ^k the vector parameter ψ at the optimization iteration k.

$$\left|\left|\nabla j(\psi^k)\right|\right|_\infty \leq \varepsilon_1 \tag{3.3.6}$$

$$\left|\left|\nabla j(\psi^k)\right|\right|_2 \leq \varepsilon_2 \tag{3.3.7}$$

$$\left|j(\psi^k) - j(\psi^{k-1})\right| \leq \varepsilon_3 \tag{3.3.8}$$

$$\psi^k - \psi^{k-1} \leq \varepsilon_4 \tag{3.3.9}$$

$$j(\psi^k) \geq \varepsilon_5 \tag{3.3.10}$$

Sometimes it is asked that the constraints be satisfied over several successive iterations.

The four first presented criteria are convergence criteria applied on the cost function gradient, on the cost function value itself, or on the parameters: the

first two criteria are the $||\cdot||_\infty$ and $||\cdot||_2$ norms of the cost function gradient at iteration k; the third criterion is related to the stabilization of the cost function from the actual iteration with respect to the previous one, and the fourth is linked to the stabilization of the parameters. These criteria are commonly used when dealing with optimization problems. The last criterion refers to the fact that when the cost function reaches a value that depends on the variance of the measurement error, the optimization algorithm should stop [100]. By lowering the cost function below a given criterion, which has to be based on measurement error, only affects the result in highlighting its intrinsic noise.

3.3.5 Optimization algorithms

Zero-order methods, also called derivative-free optimization (DFO) are based on a global vision of the cost function value j. The main interest of using such methods is when the cost function gradient is not available, or when the cost gradient is not easy to compute, or when the cost function presents local minima. There is an increasing number of computation tools to solve optimization problems with no gradient [116] such as the simplex method, which is a deterministic algorithm, and the particle swarm optimization method (PSO), which is probabilistic.

There is a great number of one-dimensional optimization methods one could find in the literature [117, 118, 119, 120]. Some of the most often used are the Newton-Raphson method, the secant method, the quadratic interpolation and the dichotomy method. Other methods may be more or less complicated and some of them may be much more optimal than the above-mentioned methods. In practice, both the Fibonacci method and the golden section search method are very widely used. The cubic interpolation method is also very widely.

There is a wide variety of multi-dimensional gradient-type optimization algorithms. Since in all cases, the stationarity of j is a necessary optimality condition, almost all unconstrained optimization methods consist in searching

the stationary point $\widetilde{\psi}$ where $\nabla j(\widetilde{\psi}) = 0$. The usual methods are iterative and proceed this way: one generates a sequence of points $\psi^0, \psi 1, \ldots, \psi^k$ which converges to a local optimum of j. At each stage k, ψ^{k+1} is defined by $\psi^{k+1} = \psi^k + \alpha^k \ \mathrm{d}^k$ where d^k is a displacement direction which may be either the opposite of the gradient of j at ψ^k $\left(\mathrm{d}^k = -\nabla j(\psi^k)\right)$, or computed from the gradient or chosen in another way provided that it is a descent direction, *i.e.* $\left(\nabla j(\psi^k),\ \mathrm{d}^k\right) < 0$. Some of the 1st order frequently used methods are:

- the gradient with predefined steps method,
- the steepest descent method,
- the conjugate gradient method for quadratic functions,
- the conjugate gradient method for arbitrary functions.

If the cost function $j(\psi)$ is twice continuously differentiable and the second derivatives exist one can use Newton's method which is a second-order method. The idea is to approach the cost function gradient by its quadratic approximation through a Taylor expansion:

$$\nabla j(\psi^{k+1}) = \nabla j(\psi^k) + \left[\nabla^2 j(\psi^k)\right] \delta\psi^k + \mathcal{O}(\delta\psi^k)^2 \tag{3.3.11}$$

and equating the obtained approximated gradient to zero to get the new parameter $\psi^{k+1} = \delta\psi^k + \psi^k$:

$$\psi^{k+1} = \psi^k - \left[\nabla^2 j(\psi^k)\right]^{-1} \nabla j(\psi^k)\ . \tag{3.3.12}$$

By using second-order optimization algorithms, the direction of descent, as well as the step size, are obtained from the last equation in one iteration. Another interesting point is the fact that the algorithm converges to $\widetilde{\psi}^k$ in a single step when applied to strictly quadratic functions. One limitation of Newton's method is when the Hessian $\nabla^2 j(\psi^k)$ is not positive definite, and also

the Hessian is usually very difficult to compute and highly time-consuming. To overcome these difficulties, one should, in practice, prefer using one of the numerous quasi-Newton methods. The quasi-Newton methods consist of generalizing Newton's recurrence formulation, Eq. (3.3.12).

Since the limitation of the Newton's method is the restriction of the Hessian to be positive definite, the natural extension consists indeed in replacing the inverse Hessian by an approximation to a positive definite matrix $\mathbf{H}^k$ which has to be updated at each step k. There is much flexibility in the computation of the matrix $\mathbf{H}^k$ but usually the imposed condition is:

$$\mathbf{H}\left[\nabla j(\psi^k) - \nabla j(\psi^{k-1})\right] = \psi^k - \psi^{k-1} \tag{3.3.13}$$

so that the approximation given by Eq. (3.3.12) is valid at previous step $k-1$. Many variations of this method can be found in the literature where corrections, of rank 1 or 2, of the type:

$$\mathbf{H}^{k+1} = \mathbf{H}^k + \mathbf{\Lambda}^k \tag{3.3.14}$$

are imposed. For the rank 1 correction, the main point is to choose a symmetric matrix $\mathbf{H}^0$ and perform the corrections so that they preserve the symmetry of the matrices $\mathbf{H}^p$. Rank 2 corrections as in the algorithms Davidon-Fletcher-Powell (DFP) and Broyden-Fletcher-Goldfarb-Shanno (BFGS) are done in a more sophisticated way where a displacement factor is introduced in the modification of the inverse Hessian [121]. If the number of the parameters is not very high and the cost function is explicitly given in terms of data, that is of the form:

$$j(\psi) := \mathcal{J}(u) = \int_{\mathcal{S}} (u - u_d)^2 \, \mathrm{d}s$$

the Gauss-Newton method or some derivatives may be interesting to deal with.

The Gauss-Newton method uses the gradient of the cost function; to define it we have to define first the derivative $u'(\psi;\delta\psi)$ of the state at the point ψ in the direction $\delta\psi$ as:

$$u'(\psi;\delta\psi) := \lim_{\varepsilon\to 0} \frac{u(\psi+\varepsilon\delta\psi)-u(\psi)}{\varepsilon} \ . \tag{3.3.15}$$

The directional derivative of the cost function can be written now as:

$$j'(\psi;\delta\psi) = (\mathcal{J}'(u), u'(\psi;\delta\psi)) \tag{3.3.16}$$

where $j'(\psi;\delta\psi) = (\nabla j(\psi), \delta\psi)$. Equivalently, the second derivative of $j(\psi)$ at the point ψ in the directions $\delta\psi$ and $\delta\phi$ is given by:

$$j''(\psi;\delta\psi,\delta\phi) = (\mathcal{J}'(u), u''(\psi;\delta\psi,\delta\phi)) + ((\mathcal{J}''(u), u'(\psi;\delta\psi))\,, u'(\psi;\delta\phi)) \ . \tag{3.3.17}$$

By neglecting the second-order term, which is actually the Gauss-Newton approach, one has:

$$j''(\psi;\delta\psi,\delta\phi) \approx ((\mathcal{J}''(u), u'(\psi;\delta\psi))\,, u'(\psi;\delta\phi)) \ . \tag{3.3.18}$$

One has to choose the directions for the canonical base of ψ to form the cost function gradient vector and the approximated Hessian matrix. The so-called sensitivity matrix S can be used, which gathers the derivatives of u in all directions $\delta\psi_i,\ i = 1,\ldots,\dim\psi$ and the product $(u'(\psi;\delta\psi_i), u'(\psi;\delta\psi_j))$ is the product of the so-called sensitivity matrix with its transpose. Thus, the Newton relationship is approximated as:

$$S^t S\delta\psi^k = -\nabla j\left(\psi^k\right). \tag{3.3.19}$$

The matrix system S^tS is obviously symmetric and positive definite with

a dominant diagonal. However, this matrix system is often ill-conditioned and one way to decrease the ill-condition feature is to "damp" the system by using:

$$\left[S^t S + \ell I\right] \delta\psi^k = -\nabla j\left(\psi^k\right) \tag{3.3.20}$$

or

$$\left[S^t S + \ell \,\mathrm{diag}\left(S^t S\right)\right] \delta\psi^k = -\nabla j\left(\psi^k\right) \ . \tag{3.3.21}$$

The "damping" parameter ℓ may be adjusted at each iteration. Note that $\ell \to 0$ yields the Gauss-Newton algorithm while ℓ larger gives an approximation of the steepest descent gradient algorithm. The presented method is the so-called Levenberg-Marquardt (LM).

A brief presentation of the parameter estimation theory was conducted in this section. From the presented methods and because of its features, the Levenberg-Marquardt method will be used in our inversion schemes. Results of the method applied to the flaw's parameter estimation will be shown in the next chapter.

3.3.6 Parameter estimation in TNDT

In this thesis we are seeking to characterize defects of delamination type. These kinds of defects can be fully characterized if one knows their shape, location and size in the three directions. As the shape, location and size in the x, y-plane will be provided from the techniques used during the pre-processing phase, here the estimation of thickness and depth of the delamination will be aimed at.

The forward model we use here accounts for defects of delamination type as boundary conditions in a fictional interface inside a double-layer plate. Thus, we are limited to consider only flaws that are located at the same depth. For

the m detected flaws, the number of the unknown parameters will be $m+1$,

$$\psi = (\psi_1, \psi_2, \ldots, \psi_{m+1})^{\mathrm{T}} .$$

If the thickness of the plate's layers is known, the number of the unknown parameters is reduced to m.

Preparation of the given data. The first step in any optimisation procedure is the preparation of the data. In this case, the input data are provided as a three-dimensional matrix $\mathbf{T}_{p_x,p_y,n+1}$, containing $n+1$ frames of $p_x \times p_y$ elements with the coefficients of the n-degree polynomials as expressed in Eq. (3.1.5). For each pixel, a couple of (p_{x_i}, p_{y_j}), we reconstruct the temperature signals in the logarithmic scale by evaluating the polynomials at the, previously chosen, time instances t_i, $i = 1, 2, \ldots, n+1$. The data to be fitted, denoted as u_d, is now the vectorised temperature field in the logarithmic scale.

The initialisation of the forward model. The second step is the configuration of the forward model using the *a-priori* information, that is, the shape, the location and the size in the x, y-plane. The initialisation of the parameter vector ψ is done by setting the thickness of every defect equal to zero and the depth at which they are located equal to half of the plate's thickness, $\psi^0 = (0, \ldots, 0, L/2)^T$, where L is the plate's thickness.

Stopping criteria. In all optimisation procedures, the choice of the stopping criteria is a crucial step. Here we will be measuring the stabilisation of the cost function and the stabilisation of the parameters themselves. This is achieved by using the aforementioned criteria Eqs. (3.3.8) and (3.3.9). Since we know that the initial data are corrupted due to some noise, we use that knowledge to apply one more criterion. This is given by Eq. (3.3.10), where a low-bound has been imposed to the cost function. A constraint on the iteration number

has been imposed, too.

3.4 Summary

In this chapter, the general theory of the strategy and the methods used for the characterization of the flaws was presented. The process of the characterization of delamination-type defects in planar media has been separated in two steps. The first step refers to the denoising of the raw signals and the detection of any possible defects, and the second one refers to the characterization of the detected defects. The first step is accomplished by using the TSR technique and the Canny algorithm which were presented. For the characterization of the defects, iterative optimization methods that will be used have been presented in detail.

Chapter 4

Modelling results and fast imaging

In this chapter, results from a model-based strategy for detection and characterisation of delamination in planar stratified media will be shown. As stated before, this approach requires a forward model which will provide the temperature field for the given configuration and an inversion scheme for the detection and the characterisation of the delamination. The numerical implementation of the derived semi-analytical model and its computational performance will be discussed in detail. The TREE model will be numerically evaluated concerning two different numerical methods, FIT and FEM, in its two- and three-dimensional configuration. Numerical results from interesting industrial configurations will be shown here. Results from the detection and the characterisation of single or multiple defects will be shown.

All simulations have been performed on a workstation equipped with an Intel® Xeon® E3-1241 v3 @ 3.5 GHz processor and 16 GB RAM. Finally, the computational times given refer to the computation of the temperature field in the mentioned region and for the given time window.

4.1 Problem definitions

Planar layered geometries can be found in many structures in different industries. The most common are structures that consists of a stack of different laminates glued together. The integrity of these structures has to be assessed during the manufacturing process and service life. One of the most common defects that can cause their failure is a delamination which can occur between their layers.

The need for reliable and effective repair of damaged structures is growing in different industries and especially in aeronautics. In order to have reliable repair, it is necessary to assess bonding and patch quality. Both delaminations in patch and disbond between patch and structure effect the integrity of the repair as the service life of the structure [122]. This is another application where a planar layer geometry can appear.

When such defects are detected, it is necessary to perform a defect assessment to identify their positions inside the structure and their dimensions. As said already, our work is focused on the characterisation of this kind of defects.

The characterisation of defects by using pulsed thermography (active thermography) often requires *a priori* knowledge of the defect-free zone in the field of the inspection. The absence of this knowledge can be compensated with the knowledge of the geometry of the structure and its thermal properties. Assuming that this knowledge has been achieved, the development of a model which describes the problem is a natural step. The developed TREE model will be used to generate accurate reference data for characterisation of the defects. The data will then be used in a minimization procedure for parameter estimation.

4.2 Modelling in TNDT

In this section, the capabilities of the developed model will be stressed. A double-layer plate with embedded thin delamination between the two layers of the plate is considered, Fig. 4.2.1, which depicts a two-dimensional projection of the configuration. The models developed in Chapter 2, with dimensions in x and y-directions being sufficiently large versus the dimensions of the area of interest so that there is no interaction with the boundary. The truncation range in the x-direction is denoted as L where the thickness of the first layer and second layer are denoted as d_1 and d_2, respectively.

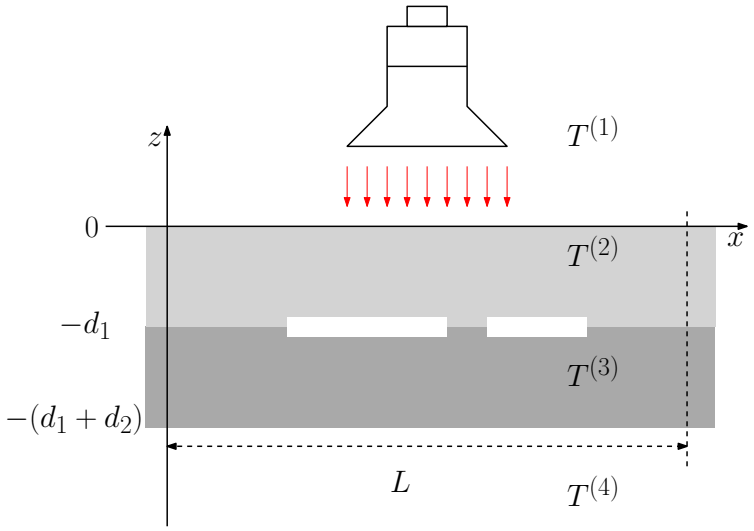

Figure 4.2.1: A two-dimensional representation of a double-layer plate with two embedded defects, illuminated by a flash lamp.

Following the experimental configuration described in [123], a flash lamp, which can deliver a heating power density of $Q = 10^6 \mathrm{W/m}^2$ on the surface of the work-piece, has been used. The flash has been modelled as a Dirac's delta in time and a uniform density in space. The inspected work-piece consists of two metallic plates of $d_1 = d_2 = 2.5$ mm thickness each. The top layer is a steel plate and the bottom one an aluminium plate. The computational region has been truncated in the $x-$direction at a length of $L_x = 50$ mm and in the $y-$direction at a length of $L_y = 50$ mm.

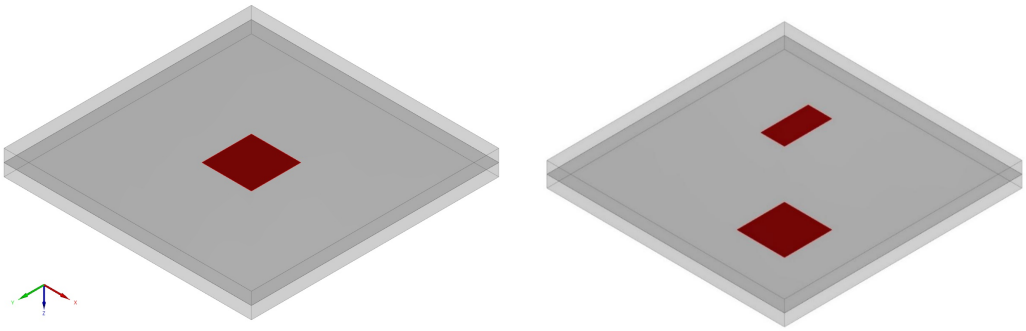

(a) Single-delamination plate. **(b)** Double-delamination plate.

Figure 4.2.2: Two double-layer plates of steel and aluminium with embedded thin delaminations.

We will be investigating here two different configurations. Their differences lay in the flaws between the layers and the spatial support of the source. In the first case, Fig. 4.2.2a, a single finite-support delamination is taken into account. This delamination is modelled as an air-filled gap of dimensions 10 mm $\times$ 10 mm in the $xy-$plane, placed at its centre. The expansion of the delamination in the $z-$direction is modelled as a delamination $d = 10^{-3}$ mm thick. The spatial support of the source, flash lamp, is an area of 30 mm $\times$ 30 mm centred on the $xy-$plane. For the second configuration, Fig. 4.2.2b, two delaminations of different sizes but of the same thickness, have been taken into account. The expansion of these delaminations in the $xy-$plane is 5 mm $\times$ 10 mm and 10 mm $\times$ 10 mm. The spatial support of the source, in this case, is an area of 45 mm $\times$ 45 mm centred on the $xy-$plane. The physical parameters of the materials used in these simulations are given in Table 4.2.1.

Table 4.2.1: Thermophysical properties of materials.

Bulk material	**Thermal conductivity** k [W/mK]	**Heat capacity** C_p [J/kgK]	**Density** ρ [kg/m^3]
Aluminium	237	897	2707
Steel	44.5	475	7850
Air	0.02454	1005	1.1843

In Fig. 4.2.3 the temperature distribution at the front and the rear surface is shown for first case at 0.0408 and 0.2143 s, respectively.

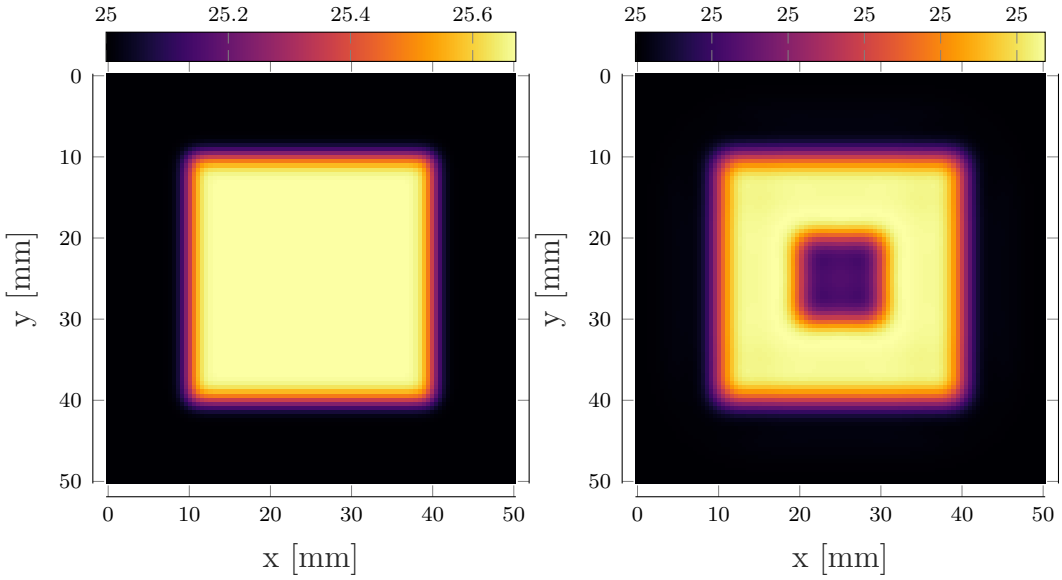

(a) Front surface, $t_1 = 0.0408$ s. **(b)** Rear surface, $t_1 = 0.0408$ s.

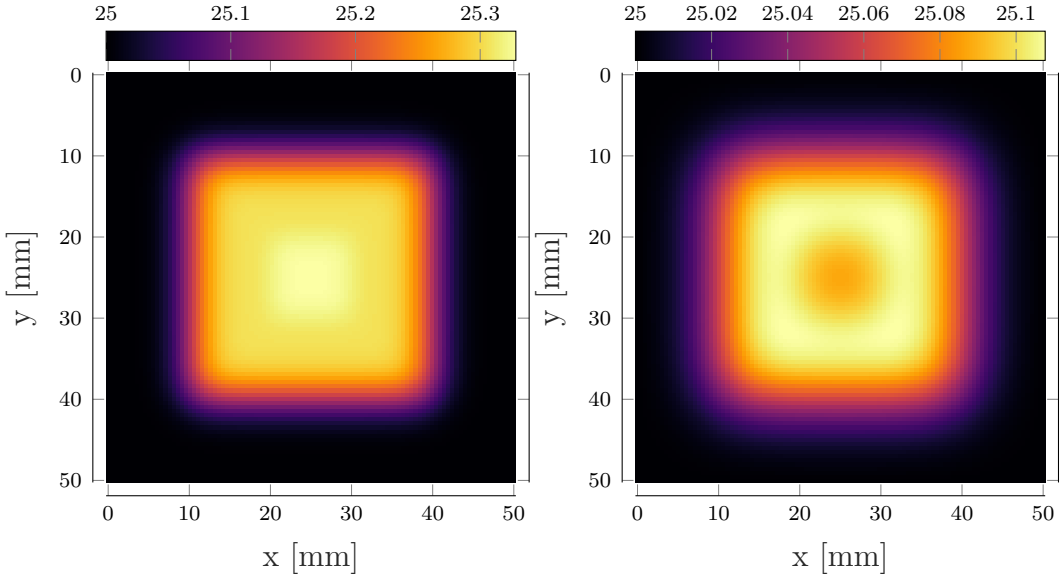

(c) Front surface, $t_2 = 0.2143$ s. **(d)** Rear surfaces, $t_2 = 0.2143$ s.

Figure 4.2.3: Simulated surface temperature field for the single-flaw configuration at two different times.

Fig. 4.2.4 show the same results for the double-flaw configuration. These

figures illustrate how heat diffusion is effected by the presence of the flaw.

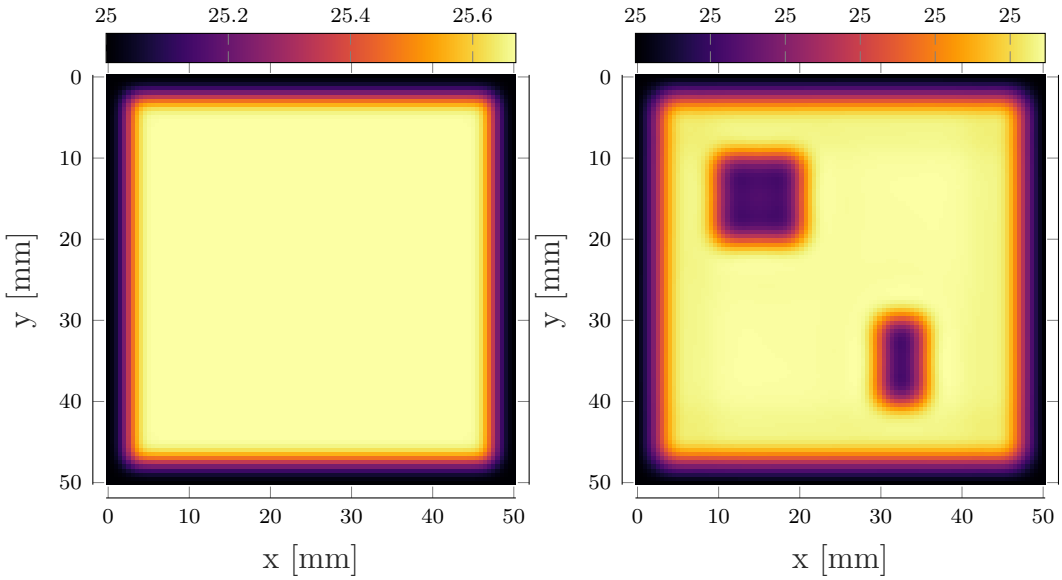

(a) Front surface, $t_1 = 0.0408$ s. **(b)** Rear surface, $t_1 = 0.0408$ s.

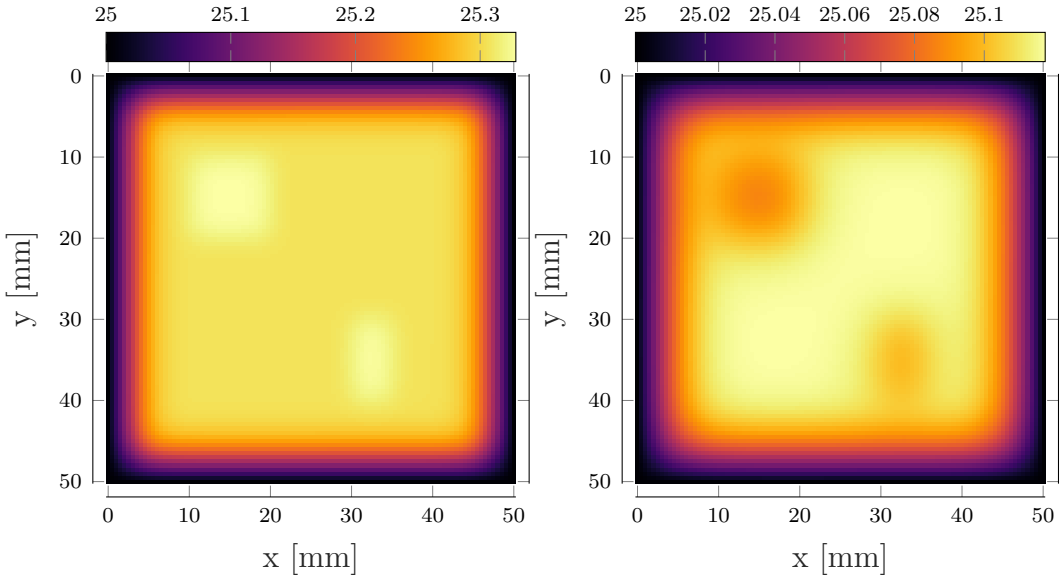

(c) Front surface, $t_2 = 0.2143$ s. **(d)** Rear surfaces, $t_2 = 0.2143$ s.

Figure 4.2.4: Simulated surface temperature field for the multi-flaw configuration at two different times.

4.2.1 Numerical validation of the TREE model

In order to proceed with a quantitative comparison of the results obtained with the TREE method, the same problem has been solved using a commercial numerical modelling software, the heat transfer module of COMSOL Multiphysics® [124]. The numerical solver of COMSOL Multiphysics® is based on the finite element method using a time-stepping technique.

The energy conservation equation treated with the COMSOL Multiphysics® solver reads as

$$\rho C_p \frac{\partial T}{\partial t} + \nabla \cdot \mathbf{q} = Q \tag{4.2.1}$$

where $\mathbf{q} = -\mathbf{k}\nabla T$. The source is described as a surface condition at $z = 0$ as

$$-\mathbf{n} \cdot \mathbf{q} = Q_b \tag{4.2.2}$$

where $Q_b(t) = Q_0\delta(t - \tau)$, [W/m^2]. The defect is described as a thin layer of resistance $R_s = d_s/k_s$, where d_s is its thickness and k_s its thermal conductivity, modelled as a surface condition

$$-\mathbf{n}_d \cdot \mathbf{q}_d = -\frac{T_u - T_d}{R_s} \tag{4.2.3}$$

$$-\mathbf{n}_u \cdot \mathbf{q}_u = -\frac{T_d - T_u}{R_s} \tag{4.2.4}$$

where the subscript u stands for the upper layer and the subscript d stands for the lower layer. The boundary conditions in the x and y directions have been taken the same as in the TREE model. Since the FEM method requires the definition of a closed box as solution domain, Dirichlet boundary conditions have been imposed also in the z-direction, at a sufficient distance from the domain of interest in order not to perturb the solution.

Thermograms simulated with TREE and FEM have been compared in Figs. 4.2.5 and 4.2.6 for the single- and double-flaw configuration, Fig. 4.2.2,

respectively. A very good agreement between both results is observed.

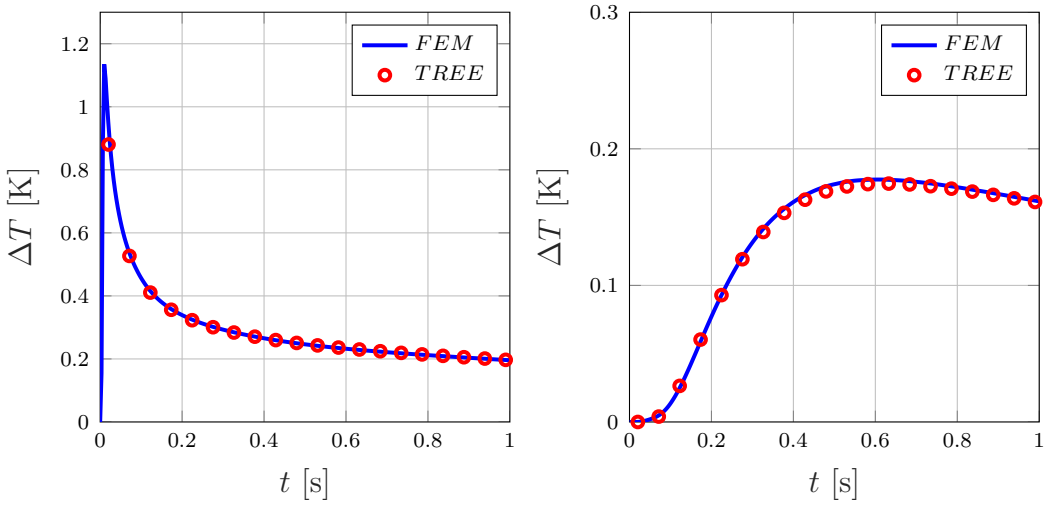

(a) Front surface. **(b)** Rear surface

Figure 4.2.5: Simulated thermograms for the single-flaw model using COMSOL Multiphysics® and the TREE method obtained at the centre of the $xy-$plane and at a distance of 0.5 mm from the surface of the plate.

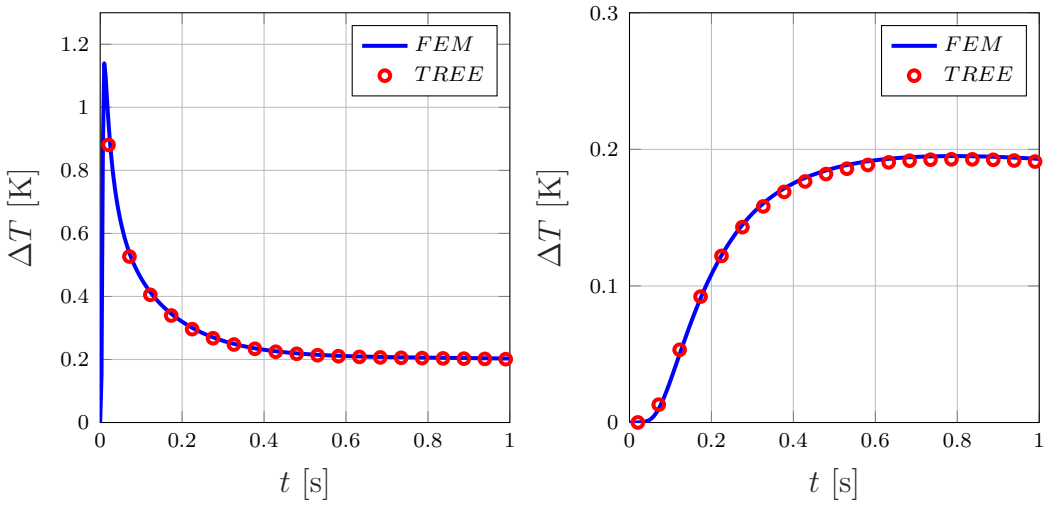

(a) Front surface. **(b)** Rear surface.

Figure 4.2.6: Simulated thermograms for the multi-flaw model using COMSOL Multiphysics® and the TREE method obtained at the centre of the $xy-$plane and at a distance of 0.5 mm from the surface of the plate.

Paying some attention to this comparison in Fig. 4.2.7 we plot the simulated thermograms for the front surface in a loglog plot. In these plots, the discrepancy between the two methods is clear in early time when it is well known that numerical methods usually fail if no adaptive discretization of the time space has been carried out.

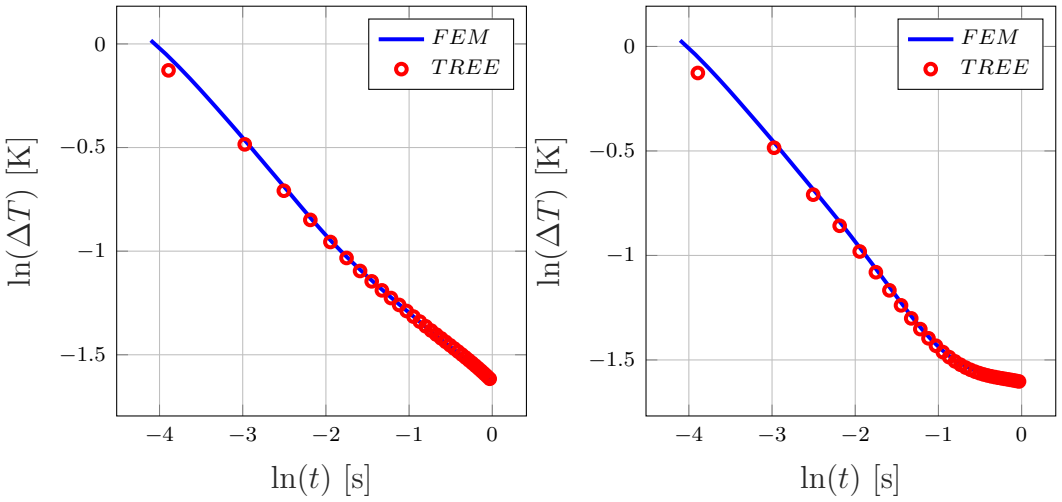

(a) Single-flaw model. **(b)** Multi-flaw model.

Figure 4.2.7: Simulated thermograms for the multi-flaw model using COMSOL Multiphysics® and the TREE method obtained at the centre of the $xy-$plane and at a distance of 0.5 mm from the front surface of the plate.

4.2.2 Computational performance of the implementation and acceleration

In this subsection, we comment on the implementation of the developed model and focus on its acceleration. This acceleration is based on the simple idea of taking advantage of the Laplace solution to the problem which gives the option to compute the solution only at specific times, *i.e.,* reduce the time sampling, since no time-stepping is performed. The starting point will be the derived equations from Chapter 2.

The temperature in the media is given in an explicit form in the Laplace

transformed time domain by a set of equations, Eq. (4.2.5), whose coefficients, $C^{(i)}$ and $D^{(i)}$, have to be computed.

$$\widehat{T}^{(1)}(x,y,z;s) = \sum_{m=1}^{M}\sum_{n=1}^{N} C_{mn}^{(1)} e^{-\mu_{mn}^{(1)} z} \sin(\kappa_m x)\sin(\lambda_n y) \tag{4.2.5a}$$

$$\widehat{T}^{(2)}(x,y,z;s) = \sum_{m=1}^{M}\sum_{n=1}^{N} \left[C_{mn}^{(2)} e^{-\mu_{mn}^{(2)}(z+d_1)} + D_{mn}^{(2)} e^{\mu_{mn}^{(2)} z}\right] \sin(\kappa_m x)\sin(\lambda_n y) \tag{4.2.5b}$$

$$\widehat{T}^{(3)}(x,y,z;s) = \sum_{m=1}^{M}\sum_{n=1}^{N} \left[C_{mn}^{(3)} e^{-\mu_{mn}^{(3)}(z+d_1+d_2)} + D_{mn}^{(3)} e^{\mu_{mn}^{(3)}(z+d_1)}\right] \sin(\kappa_m x)\sin(\lambda_n y) \tag{4.2.5c}$$

$$\widehat{T}^{(4)}(x,y,z;s) = \sum_{m=1}^{M}\sum_{n=1}^{N} D_{mn}^{(4)} e^{\mu_{mn}^{(4)}(z+d_1+d_2)} \sin(\kappa_m x)\sin(\lambda_n y) \tag{4.2.5d}$$

The computation of these coefficients is performed by solving a linear system of equations which in matrix form can be written as

$$[\mathbf{A}][\mathbf{X}] = [\mathbf{B}] \tag{4.2.6}$$

where $\mathbf{X}$ contains the unknown coefficients which will be used to compute the temperature field in the Laplace domain. The matrix $\mathbf{A}$ has to be numerically inverted for each given Laplace variable, s, which is linked to the time instances, t_i, when the solution is required. This procedure makes the implementation time consuming because of the use of the Stehfest algorithm [104, 105]. This algorithm for each t_i requires ten Laplace variables. Thus, the system has to be solved ten times for each t_i.

Since the geometry is planar, the simulated logarithmic thermograms at the surface at early times in a sound region of the plate are linear and in regions, with existing flaws, these thermograms can be approximated with low degree polynomials. We choose to reduce the time sampling by carefully choosing the time instances when the solution to the problem is computed. To do that, a

one–dimensional configuration of the given three–dimensional model including the flaw is automatically generated. If more than one flaw is present in the given model, more one-dimensional configurations have to be generated. The problem is solved for these configurations in less than a second with a relatively dense time sampling. The thermograms are then studied in the logarithmic time-space.

The logarithmic thermograms are then approximated by a polynomial and second time derivatives are reconstructed using the polynomial coefficients. Criteria upon the second time derivative have to be set in order to choose the time samples. To understand the nature of the criteria one has to understand first the behaviour of this second time derivative. In Fig. 4.2.8 the logarithmic thermograms for a sound area $\ln[T_s]$ and a flawed area $\ln[T_f]$ are compared with the logarithmic thermogram of a semi-infinite plate, $(-1/2\ln[t])$, taking out the effect of the material thermal properties. The absolute value of the second time derivatives for the flawed and the sound area are compared where the effect of the flaw on the thermograms is clear. By having this behaviour of the thermogram as a guide the chosen time samples are indicated in Fig. 4.2.8 in yellow boxes. These samples correspond to time instances where the absolute value of the second time derivative in the logarithmic space has local minima and maxima. The first and last time instances have to be added to this sampling.

This sampling is used for the solution of the three-dimensional problem and it can be safely interpolated in the logarithmic time-space in a denser time sampling if needed. After an extensive study of this approximation, under different configurations, we saw that the added relative error to the solution was lower than 0.4%, which is considered as a valid approximation. The random access memory (RAM) requirement of the method is decreased significantly, but, even more impressive, is the reduction of the CPU time by a factor larger than 20.

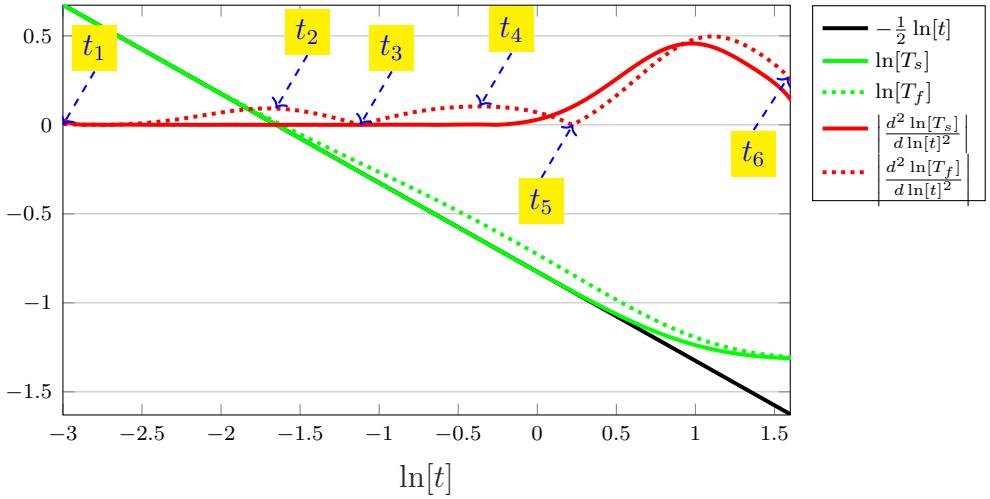

Figure 4.2.8: Thermograms in logarithmic scale for a sound area T_s, a flawed area T_f and the absolute value of their second logarithmic derivatives.

4.2.3 Application in eddy current thermography

An application in induction thermography has been presented in this early work [108]. The modelled configurations consist of a homogeneous metallic plate with a circular coil above it, as illustrated in Fig. 4.2.9. The model assumes axial symmetry along the $z-$axis. Aluminium alloy and steel has been used as materials for the plate. Two different configurations of the metallic plate has been considered also, with the first one modelling a homogenous plate with no defect in it and the second one a circular hole has been modelled at the bottom of the metallic plate.

The problem combines electromagnetic induction and thermography where the coil induces eddy current into the plate causing heating to it because of the Joule effect. This is a multi-physical problem and a two-dimensional, in-house, solver based on the finite integration technique has been used to solve it [59, 107].

The same numerical tool has been used to solve both physical problems, namely the electromagnetic induction by the coil in the plate and the heat diffusion in the plate after excitation. Due to the large difference in time scale

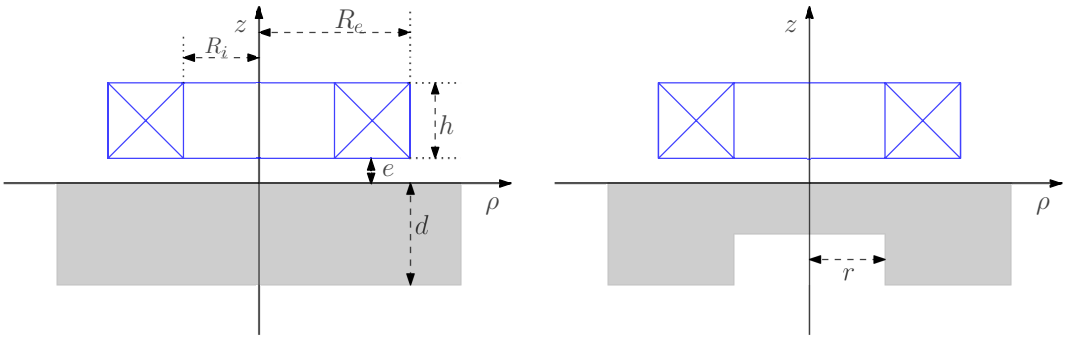

(a) Homogeneous plate.

(b) Homogeneous plate with a axisymmetric defect of radius r.

Figure 4.2.9: Schematic setup diagram. Circular coil of inner radius R_i, outer radius R_e and height h standing above a conductive plate of thickness d in a distance e.

between the electromagnetic problem and the thermal one, a weak coupling of the two problems is possible. Thus, modelling the generation of eddy current requires an electromagnetic solution in the workpiece, which results in a Joule heat distribution. The latter is used as a volumetric heating source in order to obtain the temperature distribution in the workpiece as a function of time.

The use of such a numerical solver is important to easily investigate some aspects like the effect of piece inhomogeneity or anisotropy, however, it can lead to heavy calculations and complicated meshing considerations when addressing three-dimensional configurations. For this reason, this tool was used only in its two-dimensional implementation here mostly to study the weak coupling of the two physical problems.

The theoretical formulation of the problem and numerical results of this work can be found on their full extension in Appendix F.

4.3 Flaw characterization

In this section, the proposed multi-step flaw characterization technique will be demonstrated by employing the forward model developed in Chapter 2, and the image processing and parameter estimation techniques described in Chapter 3.

Temperature signals, produced by the three-dimensional TREE model, have been corrupted with Gaussian noise of different levels to simulate temperature signals collected by an infrared camera and from now on are called raw signals. Other types of noise beyond Gaussian could be used in this part but this is out of our scope. The detection and characterization procedure has been divided into two parts.The first step concerns the detection and shape reconstruction of candidate flaws and the second step, their characterization through an iterative parameter estimation technique regularised by the information gained from the first step.

Concerning this section, the three-dimensional model developed in Chapter 2 has been used to compute the temperature field, for the general configuration depicted in Fig. 4.3.1. These signals are supposed to be collected on

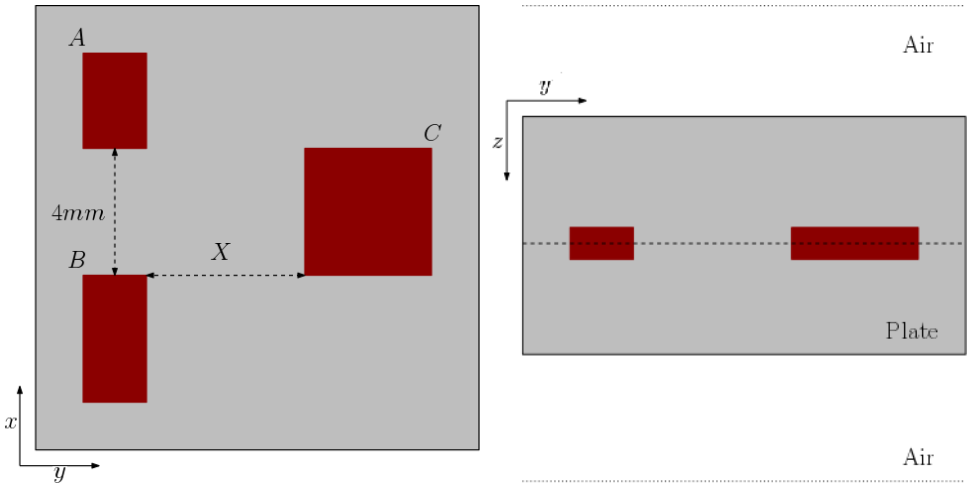

Figure 4.3.1: Sketch of the configuration in the (x, y) and (x, z)–plane, left and right respectively.

the front, or upper, surface and back, or bottom, surface of the working piece. A grade 4340 steel plate with thermal conductivity $k = 44.5$ W/mK, heat capacity $C_p = 475$ J/kgK, density $\rho = 7850$ kg/m^3 and thickness $d = 3$ mm is used. The plate is considered to be infinite in the x– and y–direction where the area of interest is a $(40 \times 40$ mm) rectangle. Three well-defined air-filled defects, named A, B and C, which simulate delaminations of different thick-

ness, $d_A = 3 \times 10^{-3}$ mm, $d_B = 2 \times 10^{-3}$ mm, $d_C = 1 \times 10^{-3}$ mm and of different sizes (2×3 mm), (2×4 mm), (4×4 mm), respectively, have been embedded into the plate with their larger faces set to be parallel to the plate surface. As an excitation term, a flash lamp, set above the plate and parallel to its surface, depositing a heating power density of $\mathrm{Q} = 10^4$ W/m^2 at the surface of the plate has been modelled as a Dirac's delta function in time, whereas its spatial distribution is considered to be uniform and covers all the domain of interest, as already done before.

4.3.1 Shape reconstruction

The described configuration will be used in this part with the addition that the flaws are located in the middle of the plate along the z–axis.

The shape reconstruction part of the technique starts by applying the TSR method to the noisy signals. This provides the polynomial approximation of the signals, say, the matrix $\mathcal{P}$ of dimensions $N_x \times N_y \times (p+1)$, where N_x, N_y are the pixels' number along the x– and y–direction, respectively, and p is the polynomial degree. Polynomial coefficients of the first and second time derivatives are stored in the matrices $\mathcal{P}_1$ and $\mathcal{P}_2$, respectively. The time-dependent temperature field in the logarithmic scale, as well as the first and second time derivatives, can be reconstructed using the polynomial matrices $\mathcal{P}, \mathcal{P}_1, \mathcal{P}_2$ and stored in the matrices $\mathcal{I}, \mathcal{I}_1, \mathcal{I}_2$, respectively. The reconstruction of the time signals derives time frames which are smoother and suitable for defect detection. The reconstructed second time derivative matrix, $\mathcal{I}_2$, will be used for the detection of the time which corresponds to the best frame.

The choice of the polynomial degree is a very crucial task for the TSR technique since it is a trade-off between the accuracy of the approximation, noise management and computational time. Here we choose to work with 7^{th} degree polynomials that were shown to approximate the original signal with high accuracy and filtering most of the noise as observed from the $\log - \log$

plots in Fig. 3.1.5. In Fig. 4.3.2 the reconstructed signals versus time are compared with the raw noisy signals as well as with the synthetic signals as a reference. The signals correspond to two different pixels with the first one being at the centre of the plate where it is considered to be a sound area, Fig. 4.3.2a and the second one at the centre of the largest defect, named C, Fig. 4.3.2b. It is clear from Fig. 4.3.2 that most of the noise has been significantly filtered through the TSR method and the original signals have been approximated with great accuracy.

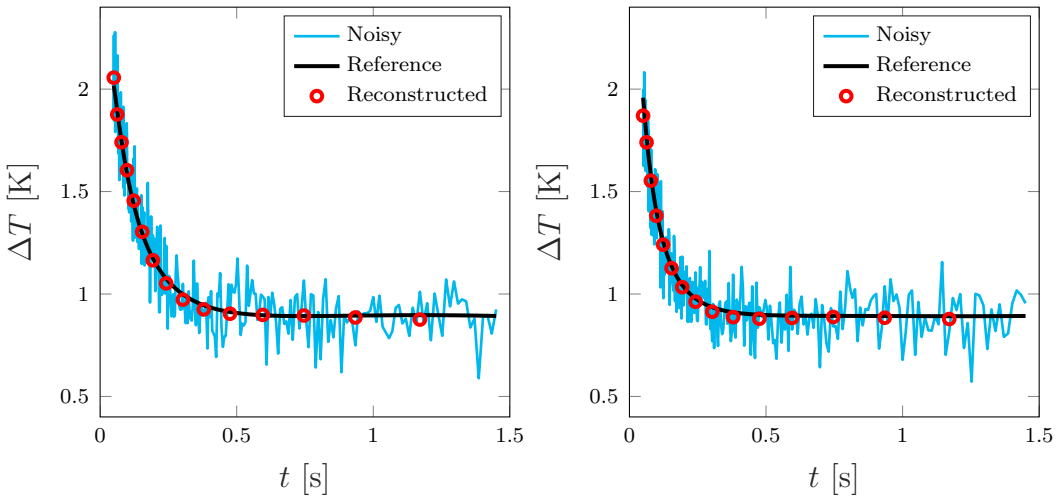

(a) Time signals corresponding to a sound area of the plate.

(b) Time signals corresponding to a flawed area of the plate.

Figure 4.3.2: Reconstruction of temperature noisy signals with the TSR technique for a sound area and a flawed area. Comparison of the reconstructed signals with the reference signals and the noisy signals.

The choice of the most suitable frame for shape reconstruction is very crucial at this point. The best frame for the shape reconstruction algorithm should correspond to a time instant which maximises the contrast of the image. The contrast for defects of different thicknesses, located at different depths reach their maximum contrast at different times [125]. To compute the contrast, one needs information about where the flaws are located and a reference sound area. Since no reference data will be used, so the computation of the contrast

could be considered as an option, the second time derivative matrix $\mathcal{I}_2$ will be used. A criterion upon the second time derivative for each pixel will be set, instead. Each variation that occurs in the time-dependent signals, which is a result of the alteration of material thermal properties at a specific depth, is indicated by a change of the first time derivative of the signals. This change on the first time derivative of the signal causes the second time derivative to change significantly. The times at which the second time derivative reaches its local maxima are correlated with the times where the absolute contrast of the second derivative reaches its local maxima. In order to have an early flaw identification, and avoid the image blurring at later times, we will take into account the times where the second time derivative changes sign. For each frame, the frequency of the sign changes of the second time derivative will be computed and the frame with the maximum frequency will be chosen as shown in Fig. 4.3.3, where the maximum frequency has been marked with a red asterisk. If the candidate frame it is not only one, the frame that corresponds to the earlier time will be chosen. This results in a sharper image but in a multilayer configuration could results in loss of information about deeply buried defects. In such a case multiple images could be used.

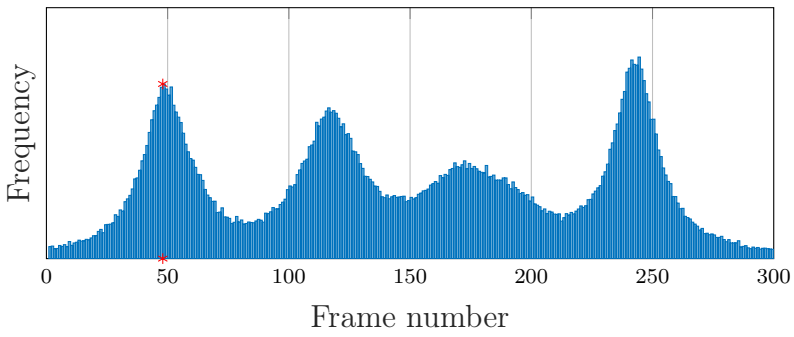

Figure 4.3.3: Frequency of the sign changes of the second time derivative for all pixels in each frame of the reconstructed signals.

The image that corresponds to that frame number is shown in Fig. 4.3.4b and that frame will be named $\mathcal{I}^*$. The effect of the technique on partially denoising the signals in space can be seen by the comparison of the derived image

with the raw image that corresponds to the same frame number, Fig. 4.3.4a. An RGB image constructed from the triplet $\mathcal{I}^*, \mathcal{I}_1^*, \mathcal{I}_2^*$ is shown in Fig. 4.3.5. The later is useful in understanding the relative depth of the flaws and their relative thickness since flaws with significantly different thickness or located at different depth appear with different colours.

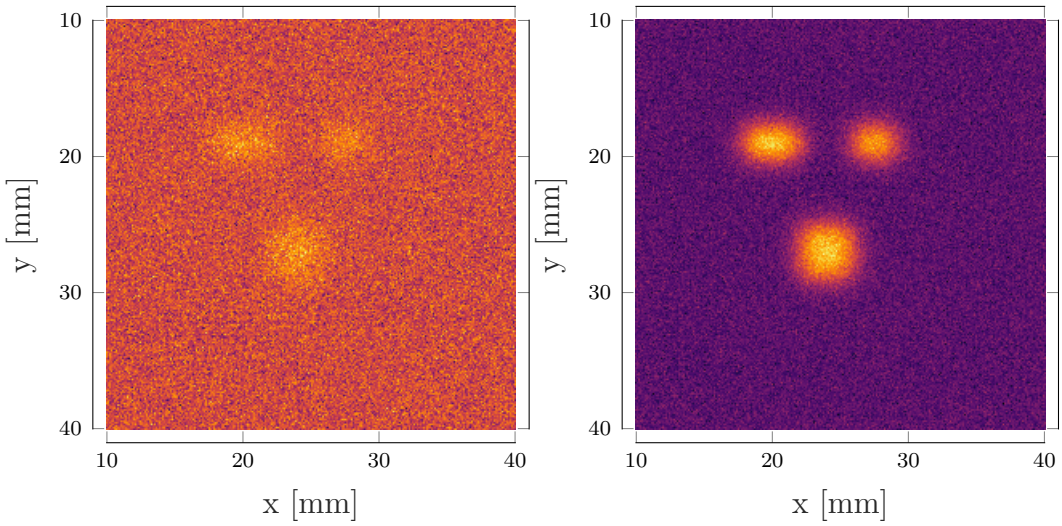

(a) Raw image. **(b)** Reconstructed image, ($\mathcal{I}^*$).

Figure 4.3.4: Comparison of a raw image with the reconstructed image corresponding to the same optimal frame number.

A similar RGB image can be constructed from the monomials but that representation is quite noisy when a high degree polynomial is used. The degree of the polynomials used here, $p = 7$, is considered to be high compared with the short time period of the recorded signals and the noise level. For a longer time period or lower noise level, an RGB image reconstructed using the monomials could be as useful as the image in Fig. 4.3.5. We illustrate this in Fig. 4.3.6 where signals with higher SNR (40) are used to reconstruct RGB images using 5^{th} and 7^{th} degree polynomials. In Fig. 4.3.6a the monomials $-5/5, 4/5, 3/5$ are used to form the image and in Fig. 4.3.6b the used monomials are the $-7/7, 6/7, 5/7$. It is clear from the figures that a lower degree polynomial will offer more qualitative information about the flaws that a higher degree

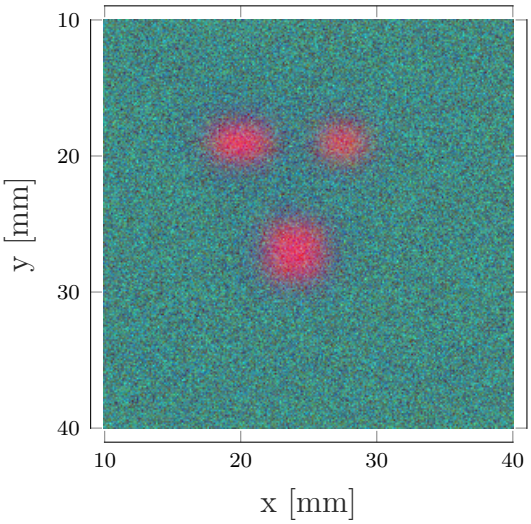

Figure 4.3.5: RGB($\mathcal{I}^*, \mathcal{I}_1^*, \mathcal{I}_2^*$) image corresponding to the optimal frame number.

polynomial which inherits a larger part of noise.

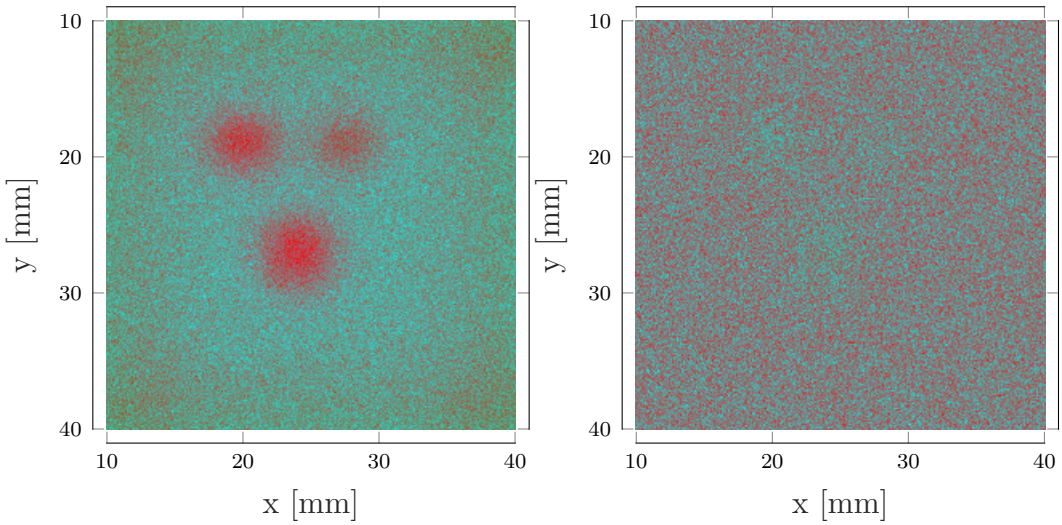

(a) TSR with 5^{th} degree polynomial. **(b)** TSR with 7^{th} degree polynomial.

Figure 4.3.6: Reconstructed RGB image from the projection of three monomials after applying TSR on noisy signals, SNR = 40.

At this point, the image $\mathcal{I}^*$ will be provided to the Canny algorithm for the detection and the reconstruction of defects' shape. The first step of the algorithm consists of a Gaussian smoothing of which the image will be a subject.

Thus the parameter σ that defines the amount of smoothing will be provided to the Canny algorithm since the smoothing algorithm has been integrated into the Canny algorithm. In our case, we perform a slight smoothing by using $\sigma = 5$. A comparison in greyscale of the input image and the smoothed one is shown in Fig. 4.3.7, where the two images have been rescaled.

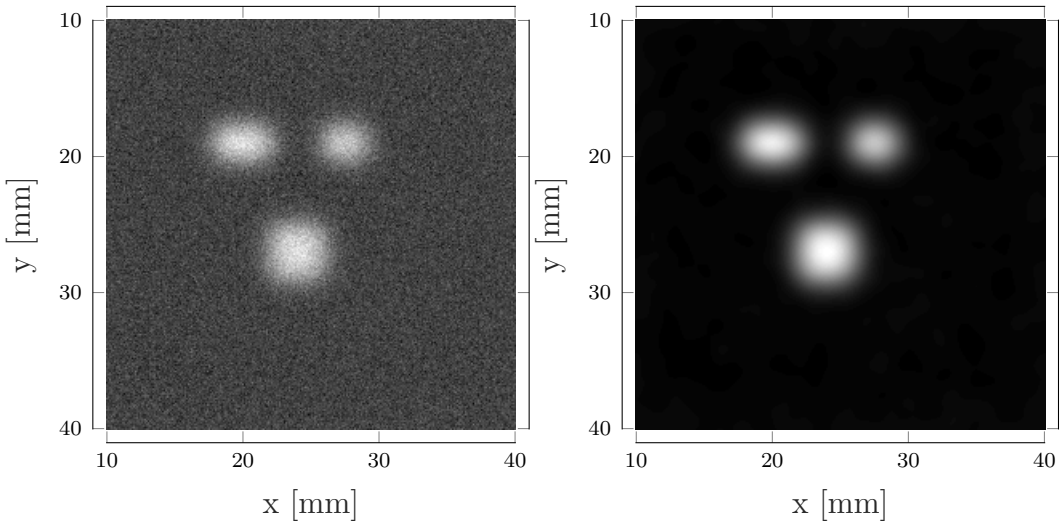

(a) The noisy input image $\mathcal{I}^*$.

(b) The smoothed image $\widehat{\mathcal{I}^*}$.

Figure 4.3.7: The impact of the Gaussian smoothing on the noisy input image for the Cany algorithm shown in grey scale.

A gradient magnitude image M, Fig. 4.3.8a, of the smoothed image $\widehat{\mathcal{I}^*}$, Fig. 4.3.7b, will be derived after its convolution with the derivative kernel, and in this case, the Sobel kernel has been used. By applying non-maximum suppression to the gradient image, all values along the line of the gradient that are not peak values of the ridge have been suppressed. This leads to the image $\widehat{M}$, Fig. 4.3.8b, which contains one pixel wide edges.

Due to noise in the original image, $\widehat{M}$ contains pixels depicting false edges and to mitigate these spurious edges, hysteresis tracking is performed using dual thresholding. The choice of the threshold parameters is very crucial for the success of the method, so we use the Otsu [112] method to compute these parameters. The method will provide the high threshold parameter τ_h and the

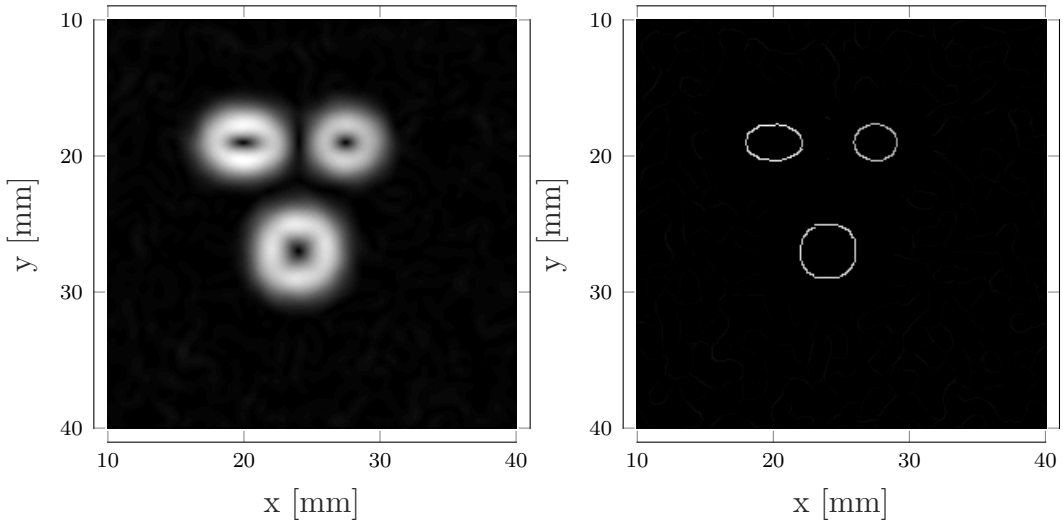

(a) The gradient intensity image before applying non-maximum suppression, $M(i,j)$.

(b) The gradient intensity image after applying non-maximum suppression, $\widehat{M}(i,j)$.

Figure 4.3.8: The impact of the non-maximum suppression on the gradient intensity image. Before, $M(i,j)$, and after, $\widehat{M}(i,j)$, applying non-maximum suppression.

low threshold parameter τ_l will be set by us, $\tau_l = \tau_h/2$. Pixels that correspond to values higher than the high threshold are considered strong edges and have been preserved, pixels that falls under the low threshold are omitted. Pixels that falls between the two threshold parameters are considered as weak edges and will be kept only if they are connected with a strong edge. The last step of the algorithm is the connection of already detected edges in the binary image under some restrictions upon the gradient and the gradient angle.

The stages of the edge detection are shown in Fig. 4.3.9, where different colours refer to different stages of the detection. The strong edges that are detected after the non-maximum suppression are in blue. In yellow and red, are the parts of the edge that was omitted or added after the hysteresis tracking, respectively. The green part of the edges is the last added part during the connectivity analysis.

The final binary image which gives the edges of the flaws is depicted

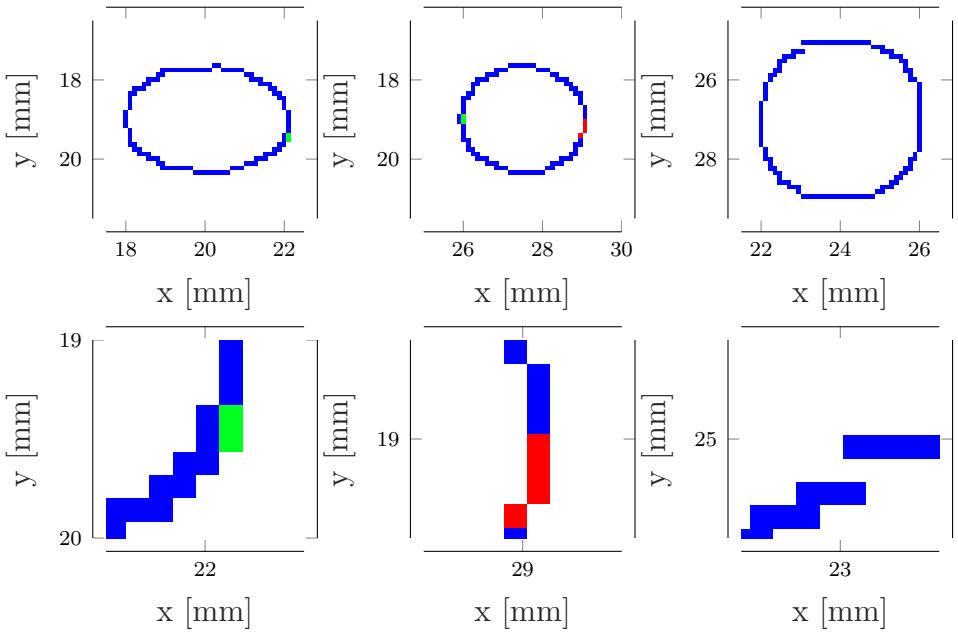

Figure 4.3.9: The stages of the edge detection algorithm illustrated with different colours.

in Fig. 4.3.10 where the true shape of the defects is depicted with green colour lines. Rectangles are fitted to the approximated defect shapes for the next step, the parameter estimation.

The presented multi-step procedure was fully automated exempting the fact that the smoothing parameter σ needed to be given. By giving a different value to that parameter the results will be effected but in our case not dramatically as can be seen in Fig. 4.3.11 where the smoothed input image is given for $\sigma = 3$, Fig. 4.3.11a, and the final binary, Fig. 4.3.11b.

For completeness of the text, the one-dimensional Gaussian kernels are depicted in Fig. 4.3.12 where the effect of the parameters is shown.

Challenging applications of this edge detection algorithm can be found in Appendix E where complex-shaped defects have been simulated and their shape has been reconstructed using the same automated multistep procedure.

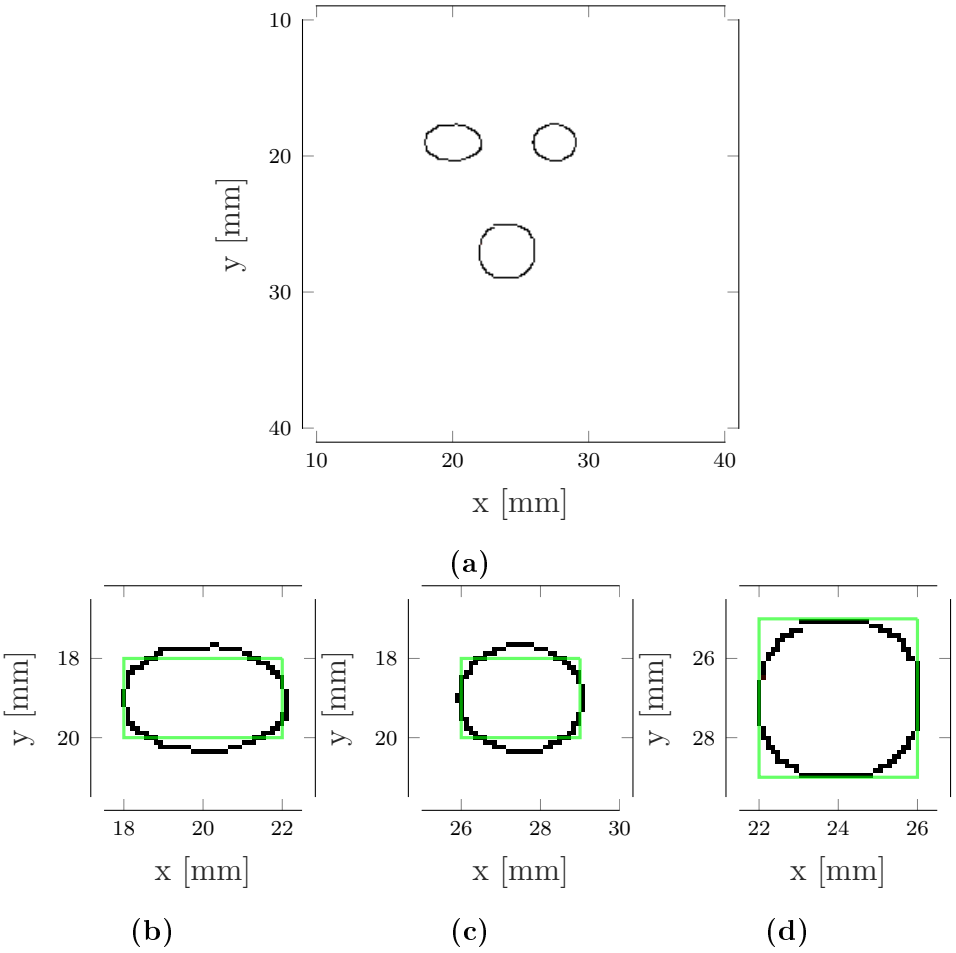

Figure 4.3.10: The final binary image.

4.3.2 Parameters estimation

Considering the configuration depicted in Fig. 4.3.1, the three embedded flaws inside the plate can be characterised exactly by their relative location inside the plate, their physical dimensions and their thermophysical properties. Their relative location in the (x, y)–plane inside the plate and their dimensions in the same plane are provided by the previous step of this procedure where the defects were well localised and their shape was approximated with great accuracy. These parameters will be used to regularize the inverse problem where the characterization of the defects is aimed at.

Since the geometry consists a double layer plate, any possible flaws will be

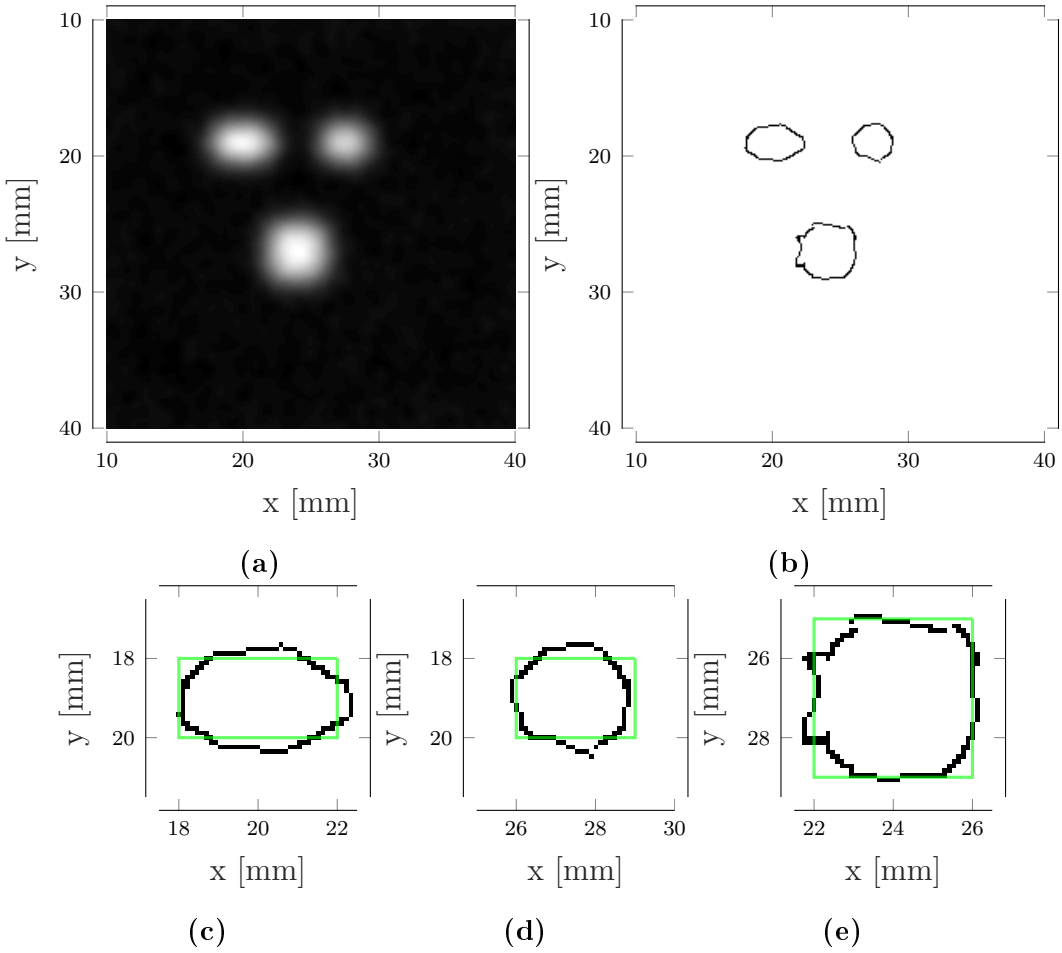

Figure 4.3.11: Gaussian smoothing of the input image to the Canny algorithm shown in grey scale. *Left:* The noisy input image $\mathcal{I}^*$. *Right:* The smoothed image $\widehat{\mathcal{I}^*}$.

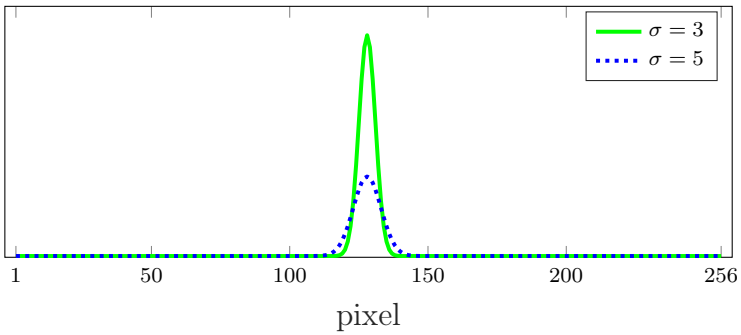

Figure 4.3.12: One-dimensional projection of the Gaussian distribution used to denoise the images.

present at the same depth, *i.e.,* the flaws will be located at same relative location inside the plate in the z–direction. Assuming that the flaws are air-filled delaminations, their material is known, thus, the parameters to be estimated are the common depth at which the flaws are located and their thicknesses, Z and d_A, d_B, d_C respectively.

The capability of the inversion scheme to estimate the defects' depth and thickness is challenged in the subsection. First, the robustness of the scheme versus additive noise is tested where different noise levels are taken into account. For each case with a different SNR, the noise has been generated 25 different times and the mean relative error for the given SNR is shown only. Raw signals in reflection, transmission and in both situations are to be fitted. The relative error occurred is shown in Fig. 4.3.13 for each estimated parameter as a function of SNR.

The correlation between SNR and estimation's relative error is clearly illustrated in Fig. 4.3.13 where a lower SNR value gives larger relative error values for the estimation of each parameter. Nonetheless, the relative error for the studied cases is less than 4% and acceptable in the field of application. From the same figure, the nature of the estimated parameters is revealed and how their estimation can be effected by the signals used. It is clear here that the best estimation of the defects' depth can be achieved by using both recorded signals, *i.e.* in reflection and transmission, and the worst one by using only the signals in transmission, Fig. 4.3.13d. The latter is not true for the estimation of the defects' thickness as it is clear from Figs. 4.3.13a to 4.3.13c where the estimation is better using the signals in transmission than in reflection.

By using the current configuration as a reference, the performance of the inversion scheme is to be tested in challenging situations. Such situations arise when the defects are located very close to the top or bottom surface of the plate. In the reference case, the defects were located at the middle of the plate, *i.e.* their distance from the top and bottom surface was 1.5 mm. For the

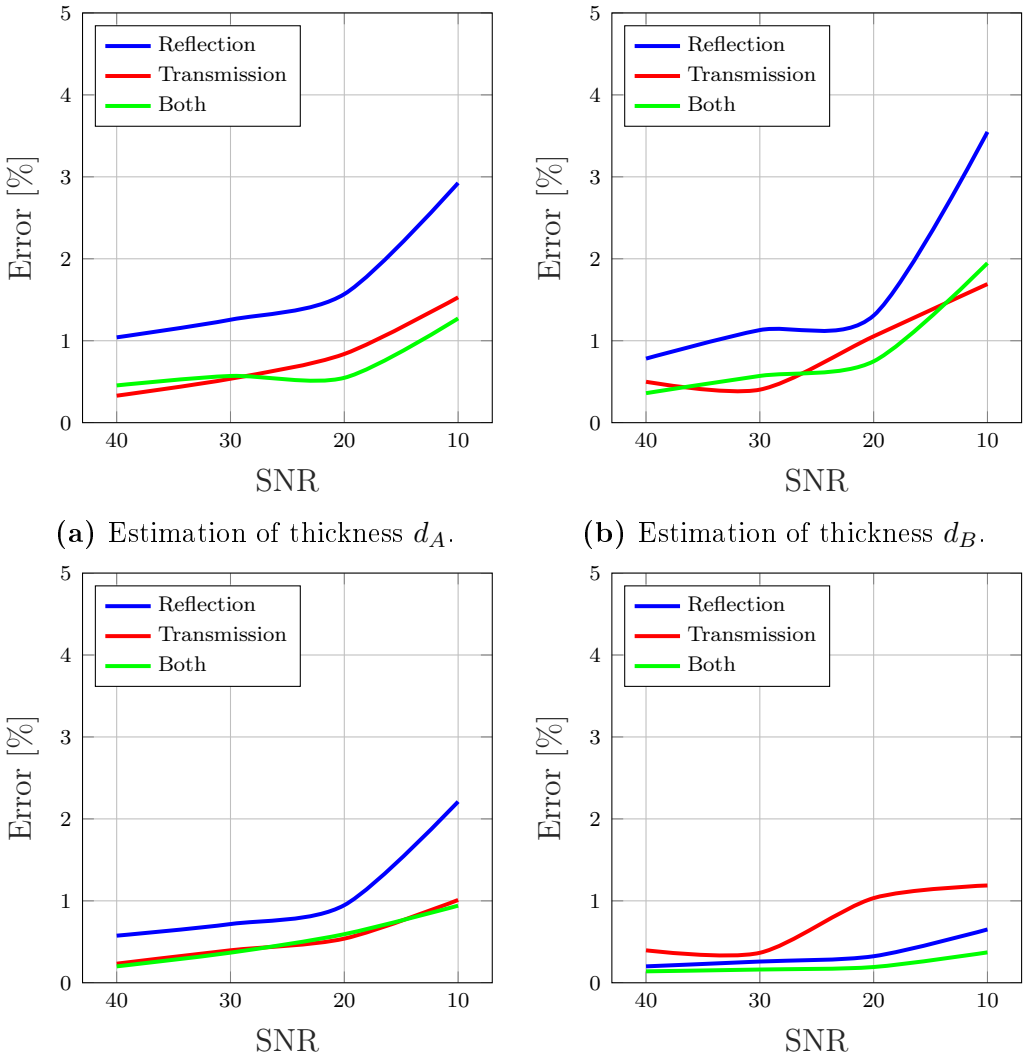

(a) Estimation of thickness d_A.

(b) Estimation of thickness d_B.

(c) Estimation of thickness d_C.

(d) Estimation of depth Z.

Figure 4.3.13: Relative error for the estimation of defects' thickness and depth as a function of SNR.

next shown results, this distance has been changed to 0.75 mm and 2.25 mm while the noise level has been kept constant, SNR = 20. The relative error occurred during the estimation of the parameters is shown in Fig. 4.3.14 for each estimated parameter as a function of defects' depth.

The estimation of the depth parameters d_A, d_B and d_C is strongly effected by the defects' depth as shown in Figs. 4.3.14a to 4.3.14b. For the configuration where the defect is deeply buried in the plate, $z = 2.25$ mm, the estimation of

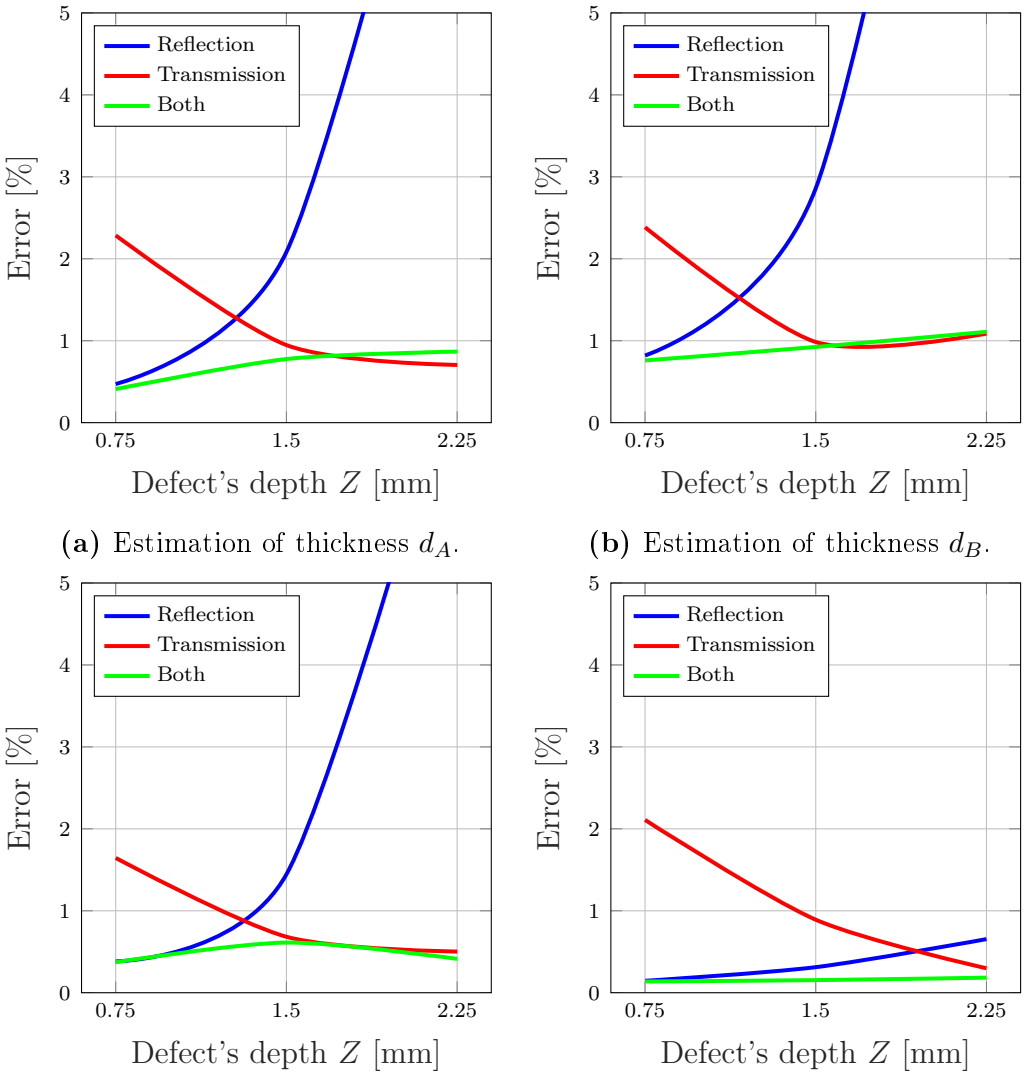

(a) Estimation of thickness d_A.

(b) Estimation of thickness d_B.

(c) Estimation of thickness d_C.

(d) Estimation of depth Z.

Figure 4.3.14: Relative error for the estimation of defects' thickness and depth as a function of defects' depth.

the thickness is very poor using the signals in reflection, relative error higher than 10%, but very accurate when using the signals in transmission. On the other hand, when the defects are close to the upper surface, the estimation accuracy is not significantly effected. As for the estimation of the defects' depth, for the buried defects the estimation accuracy is not significantly better using signals in transmission whereas in the case of the defects being close to the upper surface of the plate the estimation is better using signals in reflection.

These results agree with the physics of the problem.

An interesting configuration where the advantages of using a three-dimensional forward model could be fully exploited is that of thee defects located close to each other. This case studies the sensibility of the estimation quality on the interaction of the defects. Keeping as reference the configuration depicted in Fig. 4.3.1, new configurations have been studied. The distance X between the defects A, B and C has been adjusted from 0 mm to 5 mm and the noise level has been kept constant, $SNR = 20$. In this kind of configurations, where the interaction between the defects is strong, the one-dimensional approaches will fail to accurately characterize the defects. The advantage of using a three-dimensional model can be exemplified by Fig. 4.3.15 where one cannot find a strong connection of the estimation accuracy and the defects' relative location in the xy-plane.

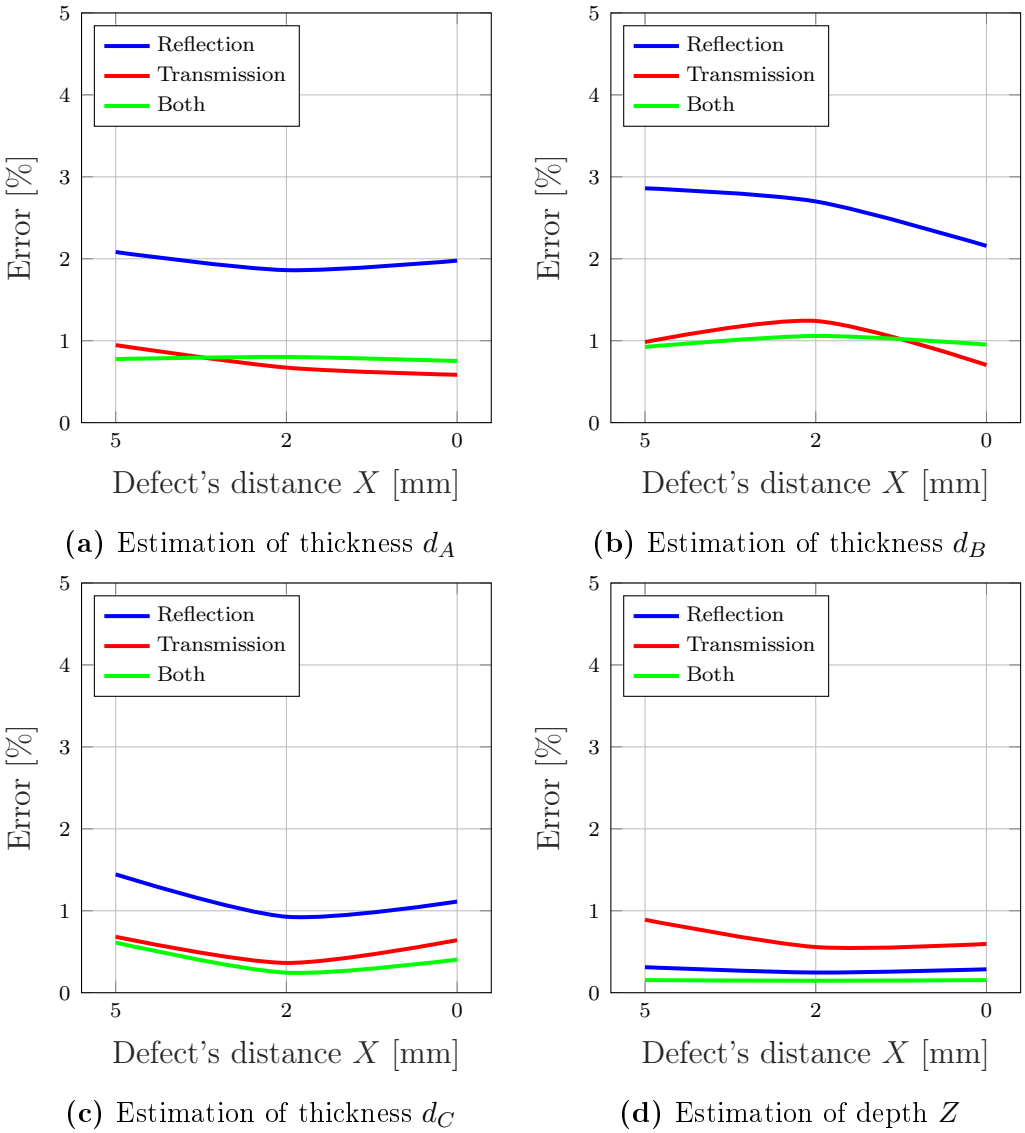

(a) Estimation of thickness d_A

(b) Estimation of thickness d_B

(c) Estimation of thickness d_C

(d) Estimation of depth Z

Figure 4.3.15: Relative error for the estimation of four parameters as a function of the relative distance X between defects A, B and C.

4.4 Summary

This chapter has been divided into two parts, numerical modelling in TNDT and defect characterization. The former deals with the numerical validation of the developed TREE model and its computational performance. A great agreement of numerical results obtained with the TREE model and with a FEM model has been shown. Furthermore, the acceleration of the developed

semi-analytical model has been described in detail. We refer also to an application in eddy current thermography. This application concerns of the inspection of a metallic plate with a circular bottom-hole using ECT. The multi-physical problem has been solved using a numerical solver based on the finite integration technique. The theoretical formulation of the problem, simulated temperature field inside the plate concerning of two different materials and a discussion on the results can be found in the Appendix F were a published work has been attached. The second part of the chapter concerns results on the flaw detection and characterization. Temperature, time-dependent, signals obtained with the semi-analytical model have been corrupted with different noise levels and been used as raw signals in this part. Appling the TSR method and the Canny algorithm, candidate defects have been localized in the x, y-plane. Their shape and dimensions have been used for the regularization of a least-square scheme to characterize their thickness and depth.

Results shown in this chapter indicate that the forward model can produce fast and accurate thermal signals and the proposed procedure for the detection and characterization of the defects is shown to be fast and accurate.

Chapter 5

Conclusions and perspectives

5.1 Recapitulation of main results

The aim of this thesis was the development of a fast three-dimensional forward model to simulate the thermographic non-destructive testing of planar pieces with embedded defects and a robust model-based inversion strategy for the detection and characterization of the defects.

A model based on the so-called truncated region eigenfunction expansion method has been presented where the thermal problem is solved in the Laplace domain with respect to time and its solution, the temperature distribution, is given as a tensor product. Configurations consisting of multi-layer planar workpieces with delamination-like defects were addressed. Thin delamination-like defects were introduced into the model as interface conditions allowing their treatment via the applied modal approach without additional discretisation needed. Flash lamp, which is used in a wide range of applications, were modelled to provide the thermal excitation term to the media. The model has been evaluated numerically with commercial simulation software and a great agreement between the results was observed.

The second goal of this thesis was the development of an inversion strategy for the detection and characterization of the defects. Signal and image

processing techniques and optimization methods available in the literature has been used to meet this goal. The thermal reconstruction technique was used to denoise the signals and compress the recorded data. The Canny edge-detection algorithm was presented in detail and used to approximate the shape of the sub-surface defects. The approximated shape of the defects projected in the x, y-plane was used as a priori information to regularize a least-square scheme used to estimate their depth and thickness. Results shown indicate that the proposed procedure for the detection and characterization of the defects is shown to be fast and accurate.

5.2 Perspectives

The presented model can be enhanced in order to improve its performance and deal with even more complex applications. The inversion strategy could feature more sophisticated inversion schemes.

Indeed, the numerical implementation of the model can be enhanced using a low-level programming language and parallelize parts of it in order to decrease further its computational time and memory requirements. The model itself could be expanded in order to include different thermal sources, such as an induction coil [108] in order to simulate a broader range of thermal inspection applications. Taking into account material anisotropy seems to be the natural next extension of the model. For the simulation of more general defect geometries, as for example corrosion, cracking, etc., one must resort to the more general strategy involving an integral equation formalism like in [126, 127].

The estimation of the transverse location and shape of the flaws could be integrated into the inversion scheme for adaptive estimation of parameters offering a faster convergence and a better estimation. Clustering algorithms can be applied in chosen images for the detection of pixels that corresponds to flawed areas. Meta-modelling approaches in combination with sophisticated

interpolators can be used to build a database which will allow nearly real-time evaluations in the parameter optimization process.

Appendices

Appendix A

Fundamental properties of the Laplace transformation.

Theorem 1.

$$\mathcal{L}\{v_1 + v_2\} = \mathcal{L}\{v_1\} + \mathcal{L}\{v_2\}$$

Theorem 2.

$$\mathcal{L}\left\{\frac{\partial v}{\partial t}\right\} = p\mathcal{L}\{v\} - v_0, \tag{A.0.1}$$

where v_0 is the value of $\lim_{t\to+0} v$. In general v_0 will be a function of the space variables x, y, z.

The result (A.0.1) follows immediately on integration by parts, since

$$\int_0^\infty e^{-pt}\frac{\partial v}{\partial t}\,\mathrm{d}t = \left[e^{-pt}v\right]_0^\infty + p\int_0^\infty e^{-pt}v\,\mathrm{d}t = -v_0 + p\bar{v}$$

Theorem 3.

$$\mathcal{L}\left\{\frac{\partial^n v}{\partial x^n}\right\} = \frac{\partial^n \bar{v}}{\partial x^n}, \tag{A.0.2}$$

with similar results for the other space variables.

This is equivalent to

$$\int_0^\infty e^{-pt}\frac{\partial^n v}{\partial x^n}\,\mathrm{d}t = \frac{\partial^n}{\partial x^n}\int_0^\infty e^{-pt}v\,\mathrm{d}t,$$

and we assume v to be such that the orders of integration and differentiation can be interchanged in this way.

Theorem 4.

$$\mathcal{L}\left\{\int_0^t v(t')\,\mathrm{d}t'\right\} = \frac{1}{p}\mathcal{L}\{v\}, \tag{A.0.3}$$

for, integrating by parts,

$$\begin{aligned}\int_0^\infty e^{-pt}\,\mathrm{d}t \int_0^t v(t')\,\mathrm{d}t' &= -\left[\frac{1}{p}e^{-pt}\int_0^t v(t')\,\mathrm{d}t'\right]_0^\infty + \frac{1}{p}\int_0^\infty e^{-pt}v\,\mathrm{d}t \\ &= \frac{1}{p}\bar{v}. \end{aligned}\tag{A.0.4}$$

Theorem 5. *If k is a positive constant, and*

$$\mathcal{L}\{v(t)\} = \bar{v}(p), \tag{A.0.5}$$

then

$$\mathcal{L}\{v(kt)\} = \frac{1}{k}\bar{v}\left(\frac{p}{k}\right), \tag{A.0.6}$$

for

$$\int_0^\infty e^{-pt}v(kt)\,\mathrm{d}t = \frac{1}{k}\int_0^\infty e^{-(p/k)t'}v(t')\,\mathrm{d}t' = \frac{1}{k}\bar{v}\left(\frac{p}{k}\right). \tag{A.0.7}$$

Theorem 6. *If a is any constant and $\mathcal{L}\{v\} = \bar{v}(p)$, then*

$$\mathcal{L}\left\{e^{-at}v\right\} = \bar{v}(p+a), \tag{A.0.8}$$

for

$$\int_0^\infty e^{-pt}e^{-at}v\,\mathrm{d}t = \int_0^\infty e^{-(p+a)t}v\,\mathrm{d}t = \bar{v}(p+a). \tag{A.0.9}$$

Theorem 7. *If $f(t) = H(t-t_0)\phi(t-t_0)$, where $H(t-t_0)$ is a Heaviside's unit function defined by*

$$H(t-t_0) = 0, \qquad t < t_0 \tag{A.0.10}$$

$$H(t-t_0) = 1, \qquad t > t_0 \tag{A.0.11}$$

then

$$\mathcal{L}\{f(t)\} = e^{-pt_0}\mathcal{L}\{\phi(t)\}. \tag{A.0.12}$$

Theorem 8. *If $f(t)$ is periodic with period T,*

$$\mathcal{L}\{f(t)\} = \frac{1}{1-e^{-pT}}\int_0^T e^{-pt}f(t)\,\mathrm{d}t, \tag{A.0.13}$$

for

$$\begin{aligned}\mathcal{L}\{f(t)\} &= \int_0^\infty e^{-pt}f(t)\,\mathrm{d}t = \sum_{n=0}^{\infty}\int_{nT}^{(n+1)T} f(t)e^{-pt}\,\mathrm{d}t \\ &= \sum_{n=0}^{\infty} e^{-npT}\int_0^T e^{-ptt}f(t')\,\mathrm{d}t' \\ &= \frac{1}{1-e^{-pT}}\int_0^T e^{-pt}f(t)\,\mathrm{d}t \end{aligned} \tag{A.0.14}$$

Theorem 9. *Lerch's theorem or the uniqueness theorem.*
If $\mathcal{L}\{f_1(t)\} = \mathcal{L}\{f_2(t)\}$, for all p, then $f_1(t) = f_2(t)$ for all $t \geq 0$, if the functions are continuous; if the functions have only ordinary discontinuities they can only differ at these point.

Theorem 10.

$$\mathcal{L}\left\{\int_0^t f_1(\tau)f_2(t-\tau)\,\mathrm{d}\tau\right\} = \mathcal{L}\{f_1(t)\}\,\mathcal{L}\{f_2(t)\}. \tag{A.0.15}$$

This is known as the Faulting or Superposition theorem, also as Duhamel's theorem.

Theorem 11. *If*

$$\mathcal{L}\{v(t)\} = \bar{v}(p), \tag{A.0.16}$$

then

$$\mathcal{L}\left\{\frac{1}{\sqrt{pt}}\int_0^\infty e^{-u^2/4t}v(u)\,\mathrm{d}u\right\} = \frac{\bar{v}(\sqrt{p})}{\sqrt{p}}. \tag{A.0.17}$$

Appendix B

The Gaver-Stehfest Method.

The principle of the method is to use the following property of the Dirac distribution $\delta(t)$, which is valid for any function $f(t)$:

$$f(t) = \int_0^\infty \delta(t-\lambda) f(\lambda)\, \mathrm{d}\lambda \tag{B.0.1}$$

A Δ-convergent function $\delta_N(t,\lambda)$ is an approximation of the shifted Dirac distribution. In therefore verifies the following property:

$$\lim_{N\to\infty} (\delta_N(t,\lambda)) = \delta(t-\lambda) \tag{B.0.2}$$

The particular Δ-convergent function that has been chosen by Stehfest is

$$\delta_N(t,\lambda) = \sum_{j=1}^{N} u_j \frac{1}{t} \exp\left(-\frac{a_j \lambda}{t}\right) \tag{B.0.3}$$

The coefficients u_j and a_j must be optimized in order to make the Laplace transforms of $\delta_N(t,\lambda)$ and of $\delta(t-\lambda)$ as close as possible, i.e.

$$2\sum_{j=1}^{N} u_j K_0(2\sqrt{a_j \lambda}\sqrt{p}) \cong \exp(-\lambda p) \tag{B.0.4}$$

Once these coefficients have been optimized, $f(t)$ can be calculated using eq.. where $\delta(t-\lambda)$ has been replaced by $\delta_N(t,\lambda)$:

$$f(t) \cong \int_0^\infty \delta_N(t,\lambda) f(\lambda)\, \mathrm{d}\lambda = \frac{1}{t}\sum_{j=1}^{N} u_j \int_0^\infty f(\lambda) \exp\left(-\frac{a_j \lambda}{t}\right)\, \mathrm{d}\lambda \qquad \text{(B.0.5)}$$

or, noting that the integral term in the last member of the preceding equation is simply the Laplace transform of f evaluated in $p = a_j/t$:

$$f(t) \cong \frac{\ln(2)}{t}\sum_{j=1}^{N} V_j F\left(\frac{j\ln(2)}{t}\right) \qquad \text{(B.0.6)}$$

This corresponds to the otpimized coefficients

$$a_j = j\ln(2) \qquad \text{and} \qquad V_j = u_j/\ln(2)$$

where the V_j are given by the following expression for an even value of N:

$$V_j = (-1)^{j+N/2} \sum_{k=Int((j+1)/2)}^{\min(N/2,j)} \frac{k^{N/2}(2k)!}{(N/2-k)!k!(k-1)!(j-k)!(2k-j)!} \qquad \text{(B.0.7)}$$

In this equation "Int" designates the integer part of a real number.

N depends on the floating-point precision of the computer. With single precision, $N = 10$ is often the most suitable choice

Appendix C

Convergence.

The before-mentioned methods are iterative methods and the choice of one of them to use depends on factors such as the convergence speed and the cost of the computation cost of the gradient. This algorithms yields to a series $\{\psi^k\}_{k\geq 1}$ that converges to $\widetilde{\psi}$.

Definition 1. *The convergence rate of the series* $\{\psi_k\}_{k\geq 1}$ *is said to be linear if*

$$\frac{||\psi_{k+1} - \psi_k||}{\left|\left|\psi_k - \widetilde{\psi}\right|\right|} \leq \tau, \quad \tau \in (0,1) \; . \tag{C.0.1}$$

This means that the distance to the solution $\widetilde{\psi}$ *decreases at each iteration by at least the constant factor* τ.

Definition 2. *The convergence rate of the series* $\{\psi_k\}_{k\geq 1}$ *is said to be super-linear in* n *steps if*

$$\lim_{k\to\infty} \frac{||\psi_{k+n} - \psi_k||}{\left|\left|\psi_k - \widetilde{\psi}\right|\right|} = 0 \; . \tag{C.0.2}$$

Definition 3. *The convergence rate of the series* $\{\psi_k\}_{k\geq 1}$ *is said to be quadratic if*

$$\frac{||\psi_{k+1} - \psi_k||}{\left|\left|\psi_k - \widetilde{\psi}\right|\right|^2} \leq \tau, \quad \tau > 0 \, . \tag{C.0.3}$$

The steepest descent method converge linearly but in the case of ill-posed problems the method may converge linearly with a constant τ close to 1. The conjugate-gradient method converges superlinearly in n steps to the optimum. Quasi-Newton methods usually converge superlinearly and the Newton method converges quadratically. Thus the quasi-Newton methods convergence-rate is much higher than the conjugate gradient methods convergence rate which need approximatively n times more steps at the same convergence behaviour. However, for the quasi-Newton method, the memory place is proportional to n^2.

Appendix D

Study on the choice of the polynomial degree.

The choice of the polynomial degree is a very crucial task for the performance of the TSR method. The TSR method acts as a low-pass filter to the noisy signals while trying to reconstruct them. The choice of the polynomial degree is a trade-off between the approximation accuracy and noise management. Choosing a low degree leads to a bad but noiseless approximation and on the other side, choosing a high degree polynomial leads to a good reconstruction of the signals reproducing also a part of the noise. In order to choose appropriately the polynomial degree for the TSR method, we carry out a numerical study.

The configurations depicted in Fig. D.1.1 consists of a single-layer and a double-layer metallic plate, left and right respectively. The materials used for this simulation are aluminium alloy and construction steel, Table D.1.1. In the single-layer configuration, the plate thickness, d, will be changing in the range of $[3, 6]$ mm and in the double-layer configuration the thicknesses, d_1 and d_2, of the plate will be set to be the half of the total thickness of the plate where the plate thickness will vary in the range of $[3, 6]$ mm.

For the given configurations, the temperature on the upper surface of the plate has been simulated and the TSR method has been applied to the noise-

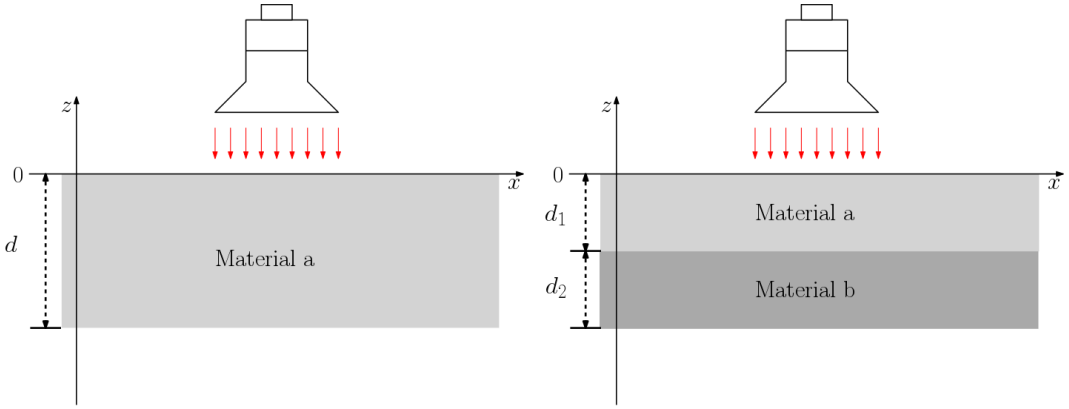

(a) Single-layer plate of thickness d.

(b) Double-layer plate of thicknesses d_1 and d_2.

Figure D.1.1: A two-dimensional representation of a metal work-piece thermal inspection.

less signals for their reconstruction, choosing polynomials of different degrees. The relative error between the simulated temperature signals in the logarithmic scale and the reconstructed ones has been computed and shown in the following plots, as a function of the polynomial degree n, next to the plots of the simulated signals.

A safe conclusion from the plots could be that the relative error introduced to the thermograms in the logarithmic scale, by the polynomial regression, decreases almost exponentially with the polynomial degree. In the tested cases, this error is less than 2% for a regression using polynomials of 5^{th} degree and less than 0.5% when using polynomials of 7^{th} degree. No significant improvement of the approximation can be seen using polynomials with a degree higher than 9.

Table D.1.1: Thermophysical properties of materials.

Bulk material	**Thermal conductivity** k [W/mK]	**Heat capacity** C_p [J/kgK]	**Density** ρ [kg/m^3]
Aluminium	237	897	2707
Steel	44.5	475	7850

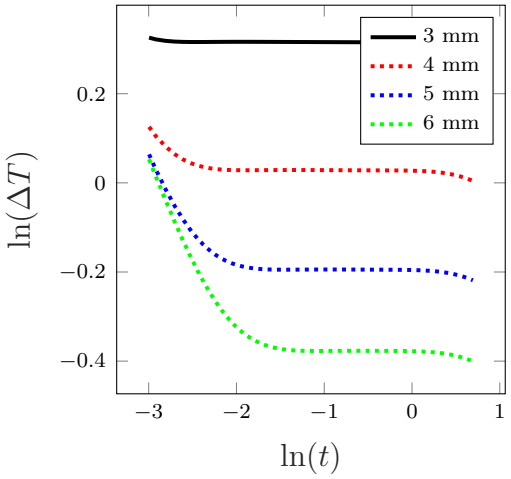

(a) Thermograms in the logarithmic scale.

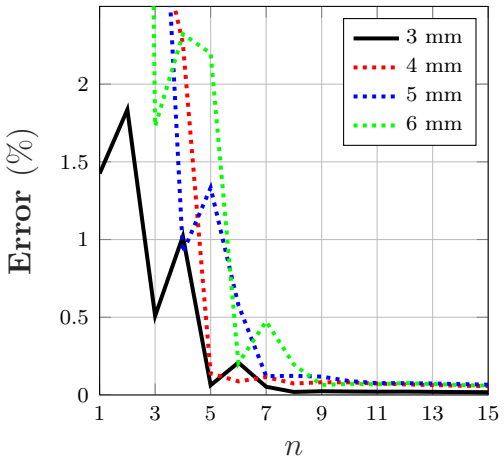

(b) Relative error of the polynomial regression as a function of the polynomial degree n.

Figure D.1.2: Thermograms in the logarithmic scale and the relative error of the polynomial regression as a function of the polynomial degree n. Single-layer aluminium plate of thickness $3, 4, 5$ and 6 mm.

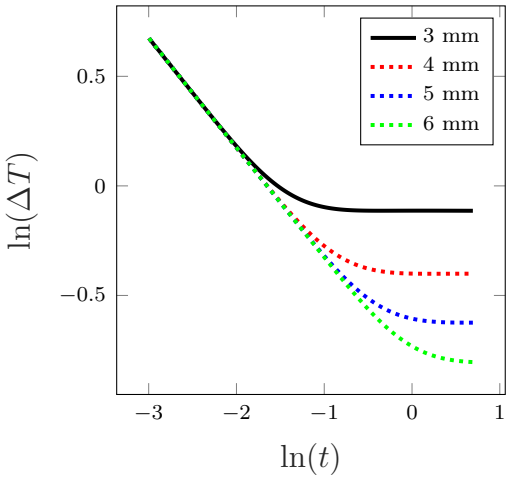

(a) Thermograms in the logarithmic scale.

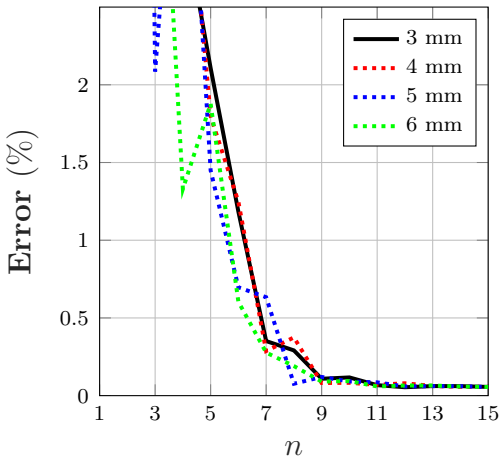

(b) Relative error of the polynomial regression as a function of the polynomial degree n.

Figure D.1.3: Thermograms in the logarithmic scale and the relative error of the polynomial regression as a function of the polynomial degree n. Single-layer steel plate of thickness $3, 4, 5$ and 6 mm.

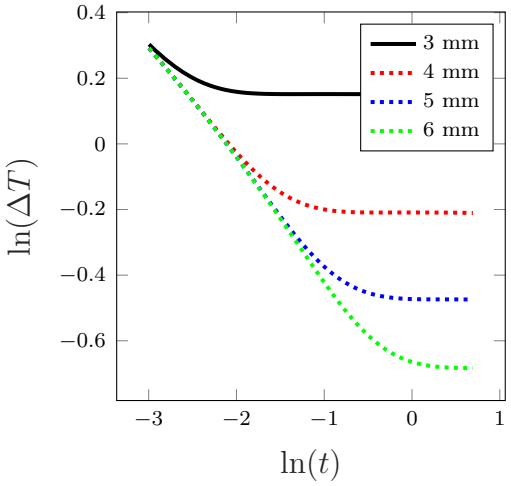

(a) Thermograms in the logarithmic scale.

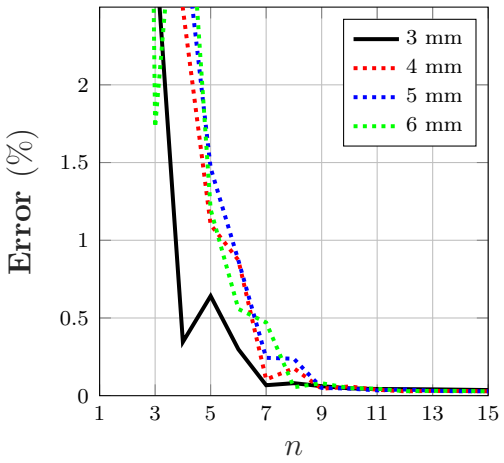

(b) Relative error of the polynomial regression as a function of the polynomial degree n.

Figure D.1.4: Thermograms in the logarithmic scale and the relative error of the polynomial regression as a function of the polynomial degree n. A double-layer plate of thickness $3, 4, 5$ and 6 mm with aluminium in the top layer and steel in the bottom layer.

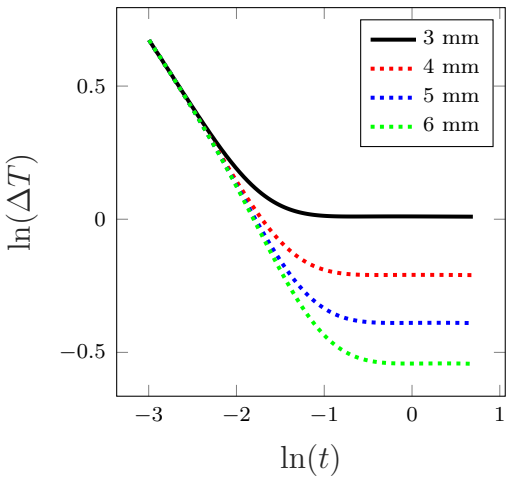

(a) Thermograms in the logarithmic scale.

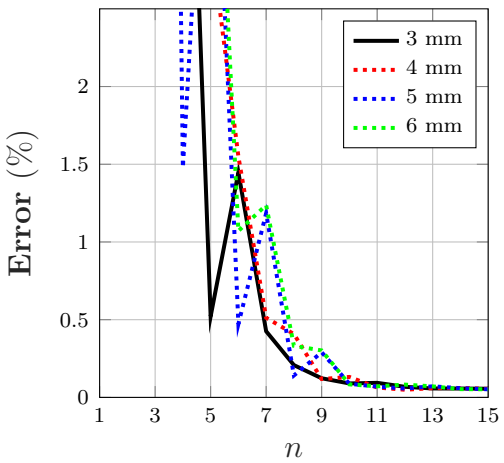

(b) Relative error of the polynomial regression as a function of the polynomial degree n.

Figure D.1.5: Thermograms in the logarithmic scale and the relative error of the polynomial regression as a function of the polynomial degree n. A double-layer plate of thickness $3, 4, 5$ and 6 mm with steel in the top layer and aluminium in the bottom layer.

Appendix E

Edge detection in challenging geometries.

The goal of this appendix is to test the reconstruction procedure in cases where shape of the defect is more complex that the ones used in the main text. The general configuration of the problem consists of a steel plate of 4 mm width and a delamination-type defect of thickness 10^{-3} mm, parallel to the plate's surface, at depth 3 mm. The top surface of the plate is illuminated by a flash lamp which delivers a heating power of $10^6 W/m^2$. The temperature at the top surface of the plate, on an 50×50 mm area, has been recorded, with a resolution of 512×512 pixels, and corrupted with Gaussian noise with the noisy signals having an SNR equal to 10.The corrupted signals are used as the starting point here and from now-on will be called raw signals.

The TSR method and the Canny algorithm are applied to the raw signals trying to reconstruct the defect's shape. Two different shapes are used in this part and depicted in Fig. E.0.1. In the TSR method, for the polynomial regression, polynomials of 7^{th} degree have been used. In the Canny algorithm, Gaussian denoising of the images has been performed using $\sigma = 3$ and the derivative image has been computed using the Sobel kernel.

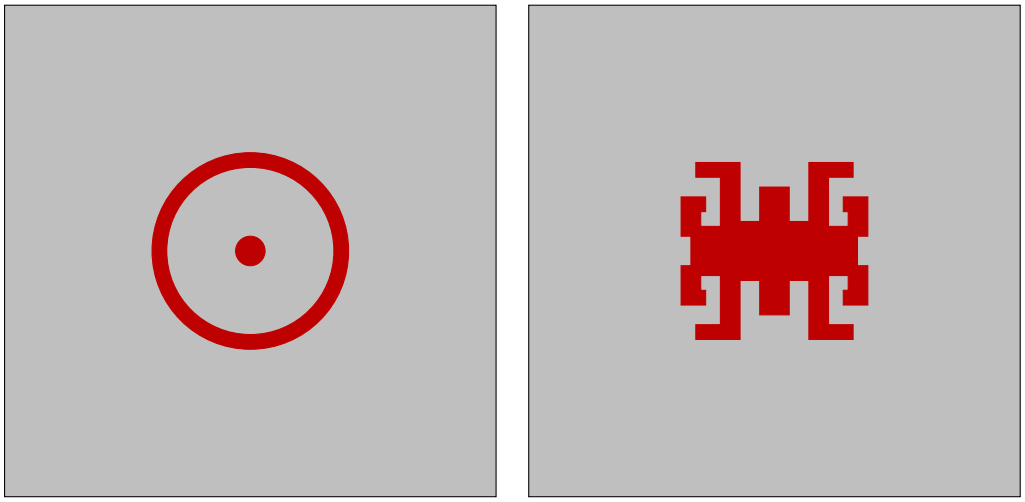

Figure E.0.1: The two geometries projected in the (x, y)-plane. *Left:* A disc of radius 1.5 mm included in a ring of internal radius 8.5 mm and external radius 10 mm. *Right:* A complex shape of dimensions 20×18 mm.

E.1 A disc inside a ring

In the first case, letting a small disc inside a ring, the best frame from the raw signals is shown in Fig. E.1.1a and after the application of TSR the reconstructed image that corresponds to the same time is shown in Fig. E.1.1b, where the features of the image are more clear.

The synthetic RGB image reconstructed from the frame shown in Fig. E.1.1b and the frame of first and second time derivative that corresponds to the same time is shown in Fig. E.1.2.

The first step of the Canny algorithm gives the smoothed image in greyscale shown in Fig. E.1.3b where is compared with the input image Fig. E.1.3a.

The gradient intensity images are shown in Fig. E.1.4 before and after applying non-maximum suppression.

The final binary image of the algorithm is shown in Fig. E.1.5 where the reconstructed edges of the defect are depicted with black colour and compared with the true shape of the defect, in green colour. The multiple stages of the Canny algorithm are shown in Fig. E.1.6 with different colours. The strong edges that are detected after the non-maximum suppression are in blue. In

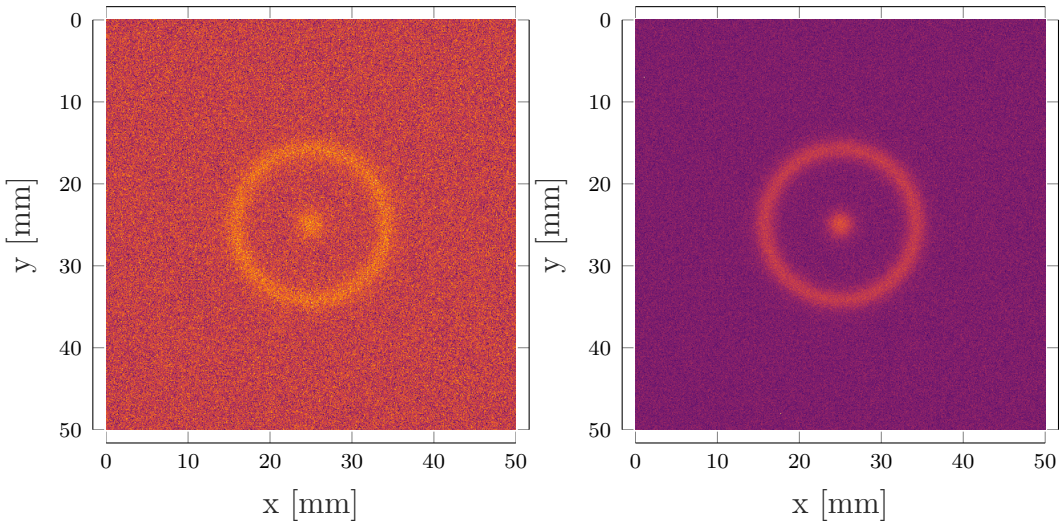

(a) Raw image. **(b)** Reconstructed image, ($\mathcal{I}^*$).

Figure E.1.1: Comparison of a raw image with the reconstructed image corresponding to the same optimal frame number.

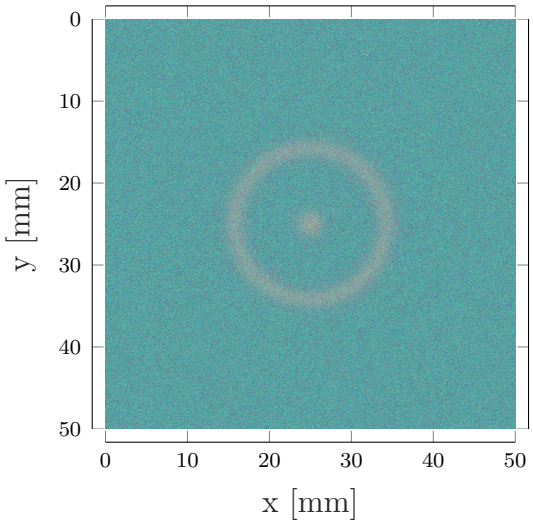

Figure E.1.2: RGB($\mathcal{I}^*, \mathcal{I}_1^*, \mathcal{I}_2^*$) image corresponding to the optimal frame number.

yellow and red, are the parts of the edge that was omitted or added after the hysteresis tracking, respectively. The green part of the edges is the last added part during the connectivity analysis. To help the reader, the parameters used for the edge detection are written in the caption of the images where p is the polynomial degree and σ refers to the Gaussian smoothing.

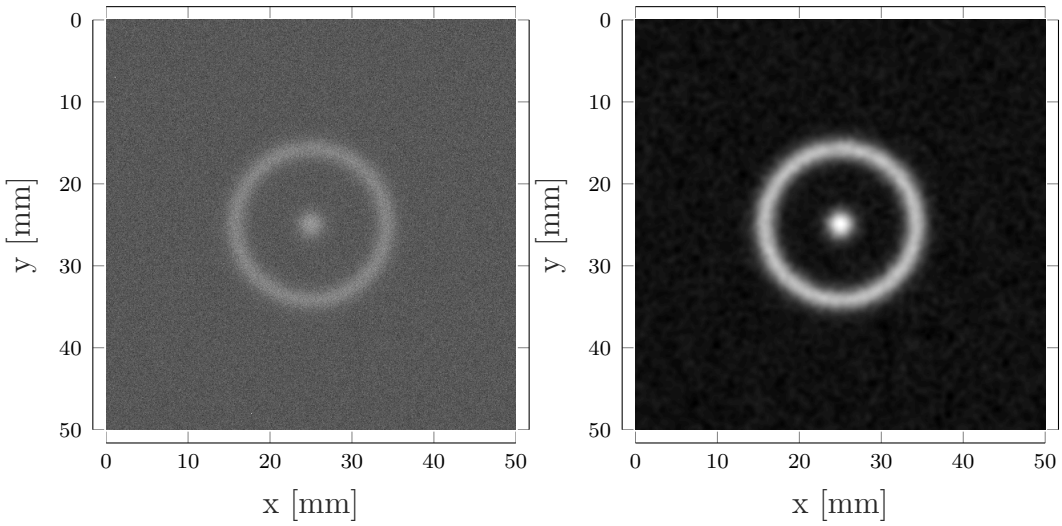

(a) The noisy input image $\mathcal{I}^*$.

(b) The smoothed image $\widehat{\mathcal{I}^*}$.

Figure E.1.3: The impact of the Gaussian smoothing on the noisy input image for the Canny algorithm shown in grey scale.

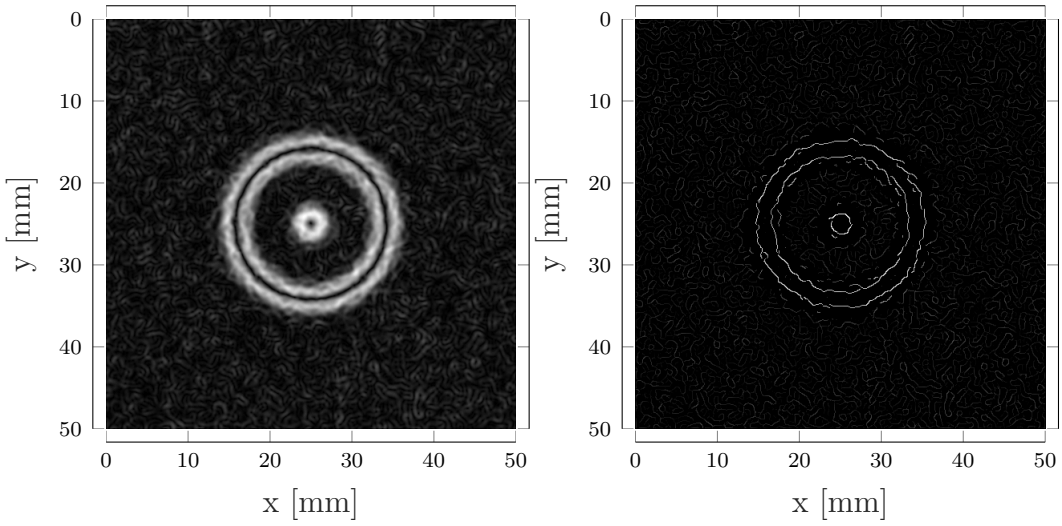

(a) The gradient intensity image before applying non-maximum suppression, $M(i,j)$.

(b) The gradient intensity image after applying non-maximum suppression, $\widehat{M}(i,j)$.

Figure E.1.4: The impact of the non-maximum suppression on the gradient intensity image. Before, $M(i,j)$, and after, $\widehat{M}(i,j)$, applying non-maximum suppression.

Trying to improve the edge detection one could change the used parameters for the two used techniques. Changing the smoothing parameter σ from 3 to

5 will give a less noisy input image resulting a smoother edge detection but with the risk of loosing in resolution. The binary image is shown in Fig. E.1.7 and the stages of the algorithm in Fig. E.1.8 where the detected strong edges, coloured in blue, are the only one processed from the algorithm.

A different strategy to improve the edge detection could be lowering the degree of the polynomial used for the polynomial regression by the TSR method. by setting the polynomial degree equal to 5 the resulting binary image is shown in Fig. E.1.10 and the image with the stages of the algorithm in Fig. E.1.9. The approximation of the edges is better than using 7^{th} degree polynomial but not significantly.

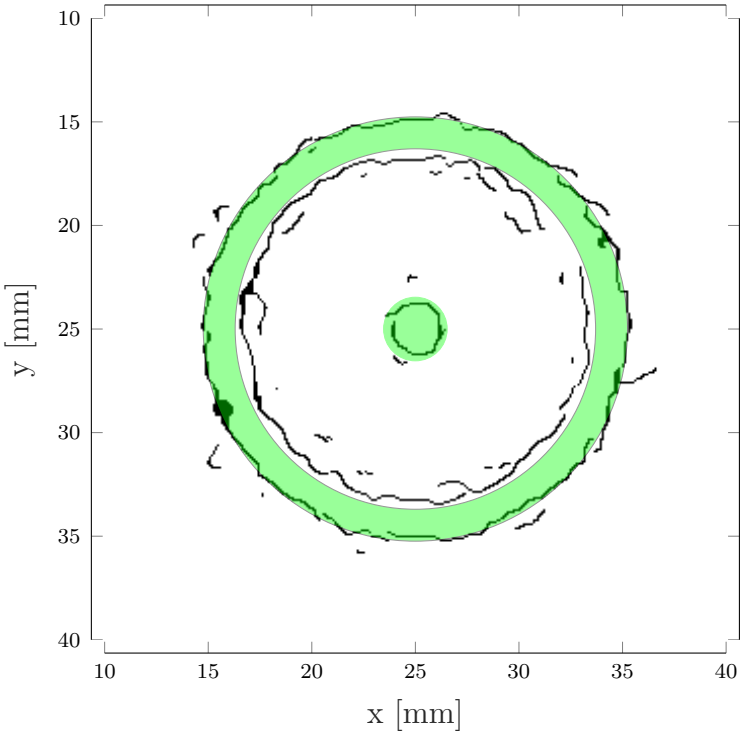

Figure E.1.5: Binary image for $p = 7$ and $\sigma = 3$.

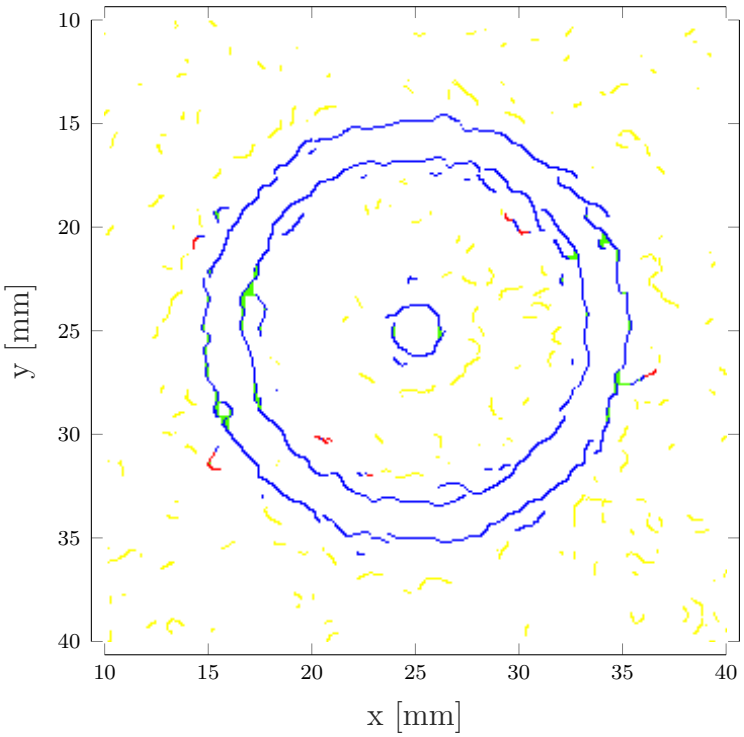

Figure E.1.6: Stages image with $p = 7$ and $\sigma = 3$.

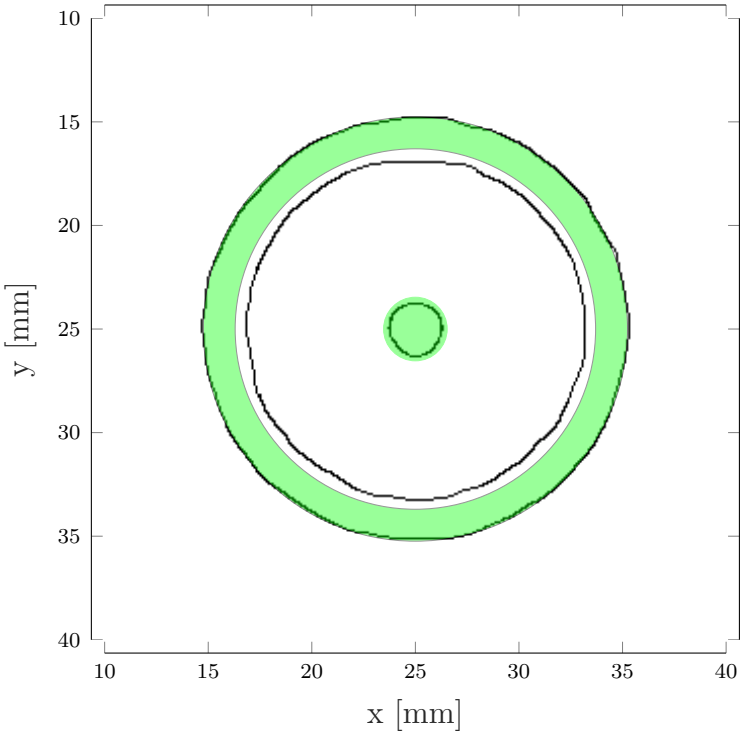

Figure E.1.7: Binary image for $p = 7$ and $\sigma = 5$.

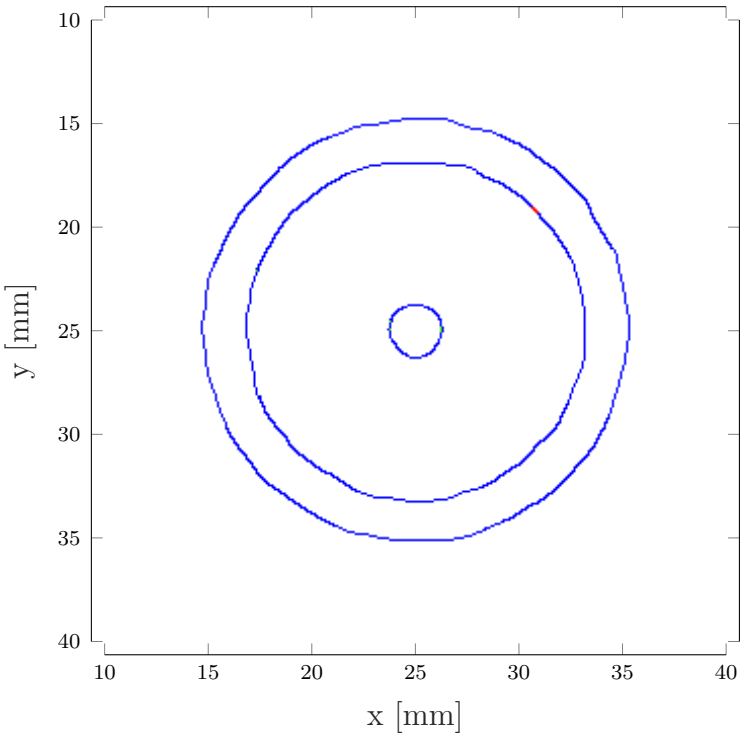

Figure E.1.8: Stages image with $p = 7$ and $\sigma = 5$.

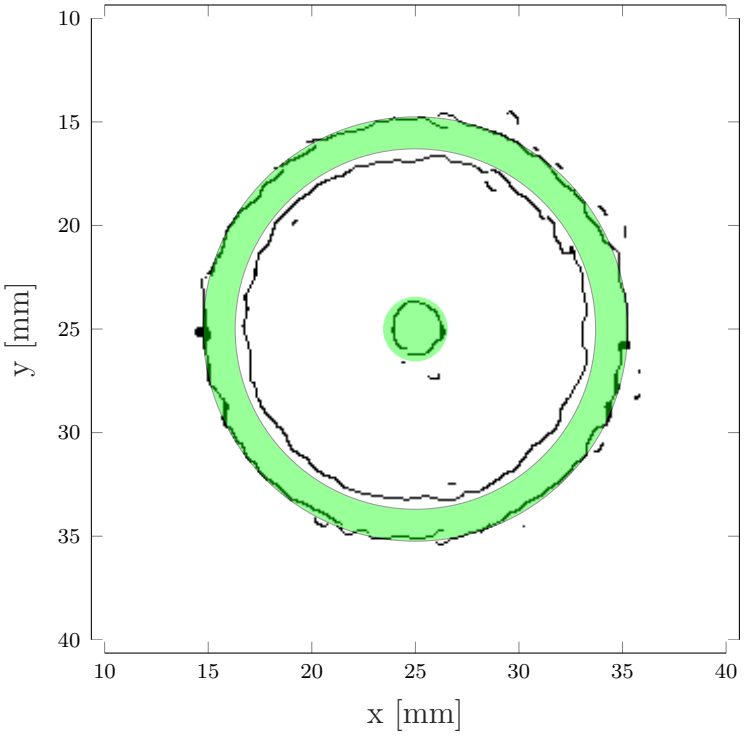

Figure E.1.9: Binary image for $p = 5$ and $\sigma = 3$.

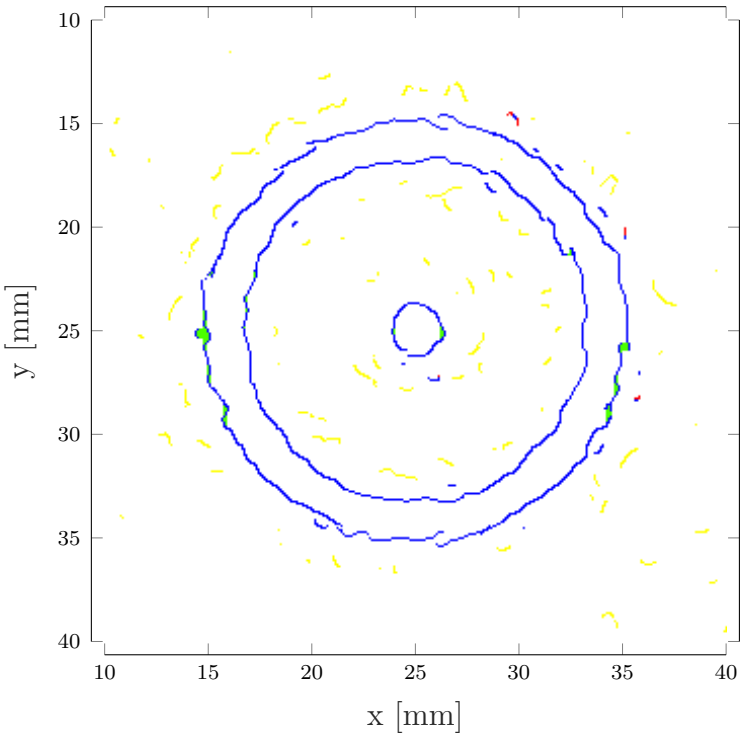

Figure E.1.10: Stages image with $p = 5$ and $\sigma = 3$.

E.2 The "spider"

Because of the shape used in the previous section, one cannot have a clear picture of how the resolution of the approximation is effected by the used parameters in the parts of the edge detection. To demonstrate this, a different shape defect with very thin part and many angles is considered here. In Fig. E.2.1a, the best frame from the raw signals is shown and in Fig. E.2.1b the reconstructed image after the application of TSR, corresponding to the same time, is shown.

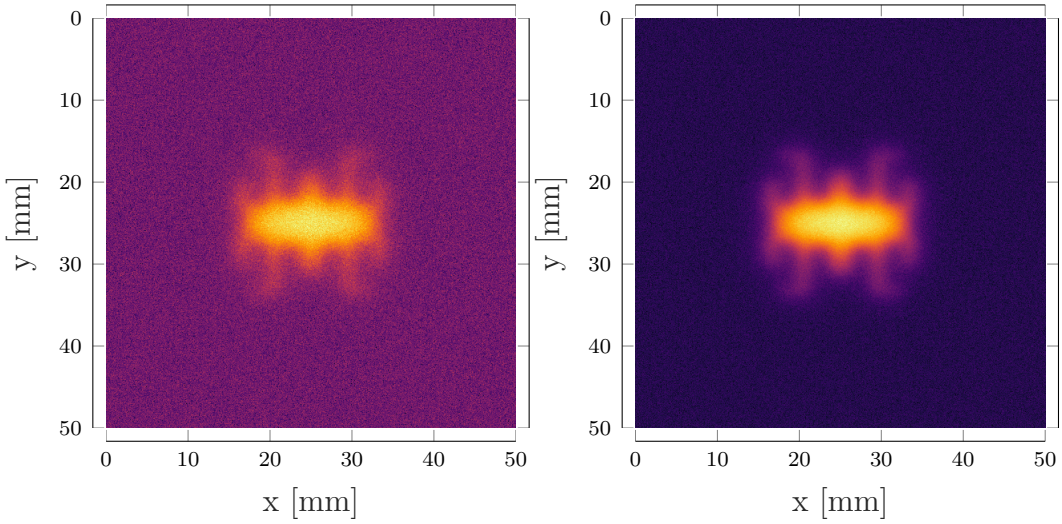

(a) Raw image. **(b)** Reconstructed image, ($\mathcal{I}^*$).

Figure E.2.1: Comparison of a raw image with the reconstructed image corresponding to the same optimal frame number.

The synthetic RGB image reconstructed from the frame shown in Fig. E.2.1b and the frame of first and second time derivative that corresponds to the same time is shown in Fig. E.2.2 where the defect is distinguished from the background and its central part is pictured in different colour.

The smoothed image in greyscale is shown in Fig. E.2.3b where is compared with the input image Fig. E.2.3a.

The gradient intensity images are shown in Fig. E.2.4 before and after applying non-maximum suppression.

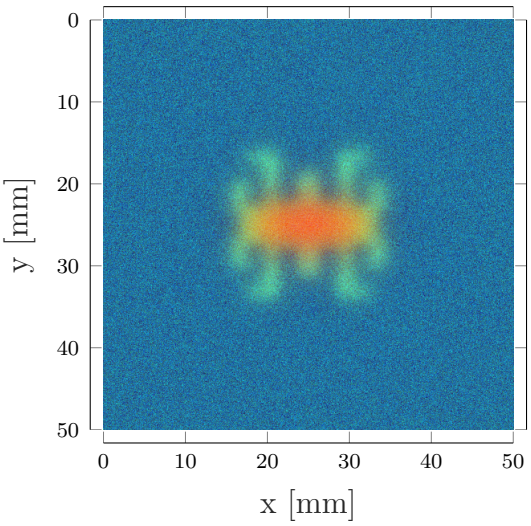

Figure E.2.2: RGB($\mathcal{I}^*, \mathcal{I}_1^*, \mathcal{I}_2^*$) image corresponding to the optimal frame number.

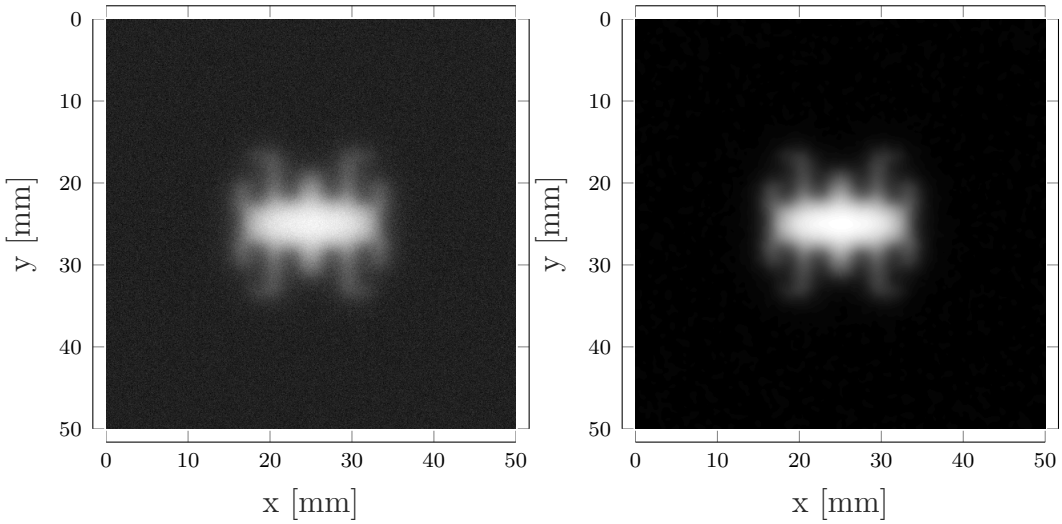

(a) The noisy input image $\mathcal{I}^*$.

(b) The smoothed image $\widehat{\mathcal{I}^*}$.

Figure E.2.3: The impact of the Gaussian smoothing on the noisy input image for the Canny algorithm shown in grey scale.

The final binary image of the algorithm is shown in Fig. E.2.5 where the reconstructed edges of the defect are depicted with black colour and compared with the true shape of the defect, in green colour. The image contains many false edges and its true edges are not all detected. The multiple stages of the Canny algorithm are shown in Fig. E.2.6 with different colours. For the

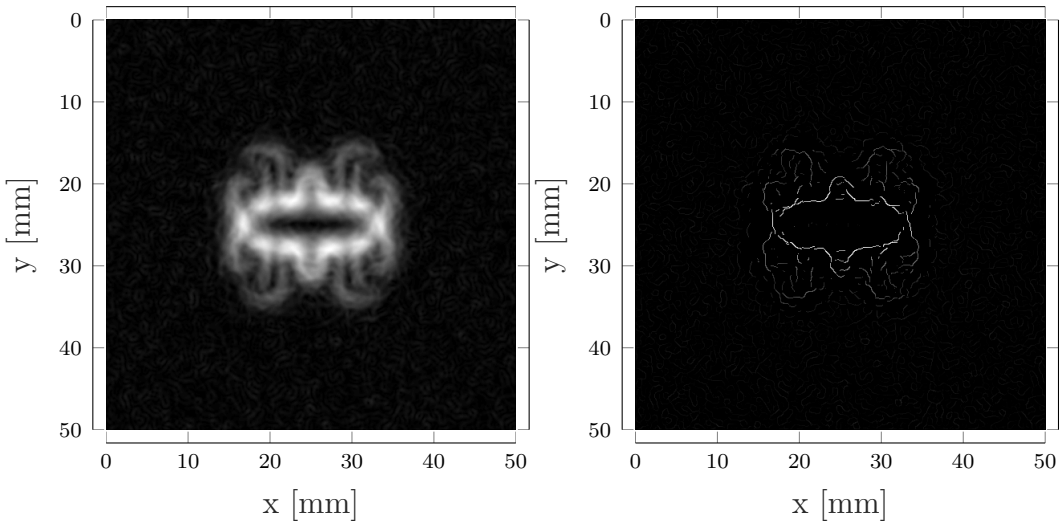

(a) The gradient intensity image before applying non-maximum suppression, $M(i,j)$.

(b) The gradient intensity image after applying non-maximum suppression, $\widehat{M}(i,j)$.

Figure E.2.4: The impact of the non-maximum suppression on the gradient intensity image. Before, $M(i,j)$, and after, $\widehat{M}(i,j)$, applying non-maximum suppression.

obtained results here, 7^{th} degree polynomial has been used for the TSR method and for the Canny algorithm the image was subject of Gaussian smoothing with $\sigma = 3$ and the derivative kernel used is the Sobel kernel.

To preserve a high resolution of the detection, a different strategy is followed here. A 5^{th} degree polynomial is used to reconstruct the edges shown in Fig. E.2.7. The stages of the algorithm are shown in Fig. E.2.8. The reconstructed image is less spurious with many less false edges added to the binary image and with the true edges detected better than previously.

To improve the edge detection, the polynomial degree is kept the same but the smoothing of the image is changed. Using $\sigma = 5$ the reconstructed binary image is shown in Fig. E.2.9 and the stages of the algorithm in Fig. E.2.10. Comparing the resulting binary image with the previous case, less false edges are included.

To move a step further, a different derivative kernel is used and results are

shown in the following figures. The edge detection is not improved significantly except in few parts of the defect contour.

In this case, the used kernel is the one proposed in [111] which is a Gaussian derivative with optimized sigma $\sigma = 0.6769$

$$K_x = \begin{bmatrix} 0.0007 & 0.0037 & 0 & -0.0037 & -0.0007 \\ 0.0052 & 0.1187 & 0 & -0.1187 & -0.0052 \\ 0.0370 & 0.2589 & 0 & -0.2589 & -0.0370 \\ 0.0052 & 0.1187 & 0 & -0.1187 & -0.0052 \\ 0.0007 & 0.0037 & 0 & -0.0037 & -0.0007 \end{bmatrix}, \quad K_y = K_x^T. \tag{E.2.1}$$

and the author shows that this kernel gives a minimal angle error in cases with complex shapes.

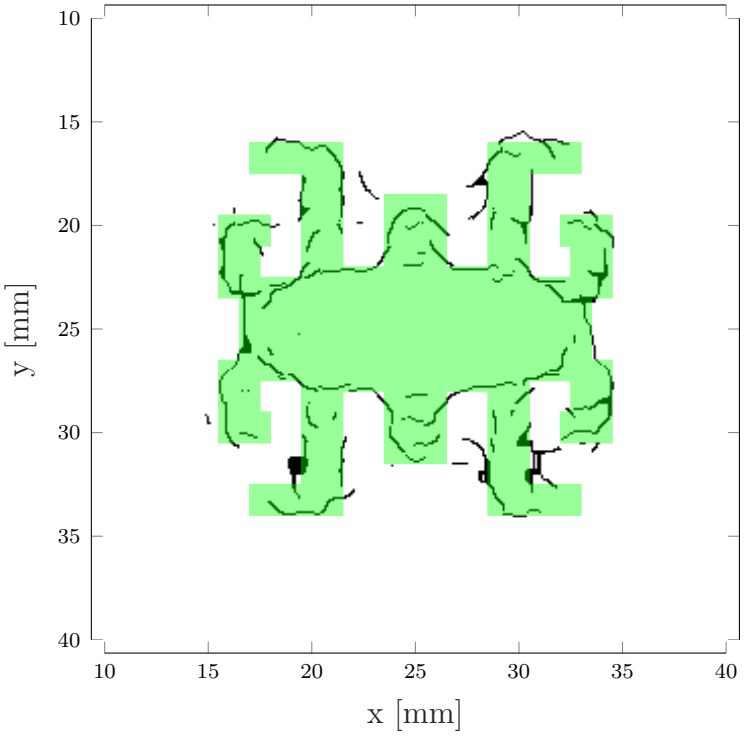

Figure E.2.5: Binary image for $p = 7$ and $\sigma = 3$.

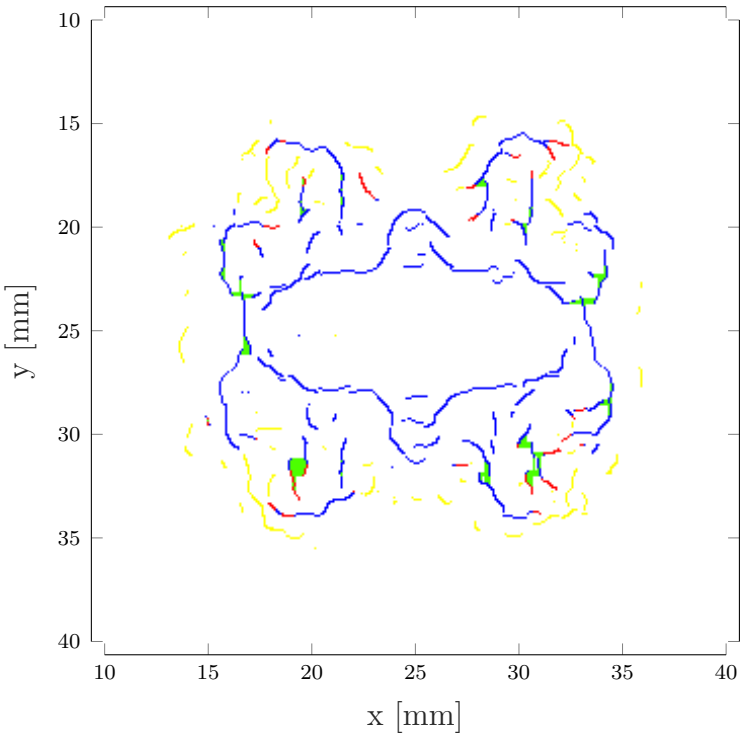

Figure E.2.6: Stages image with $p = 7$ and $\sigma = 3$.

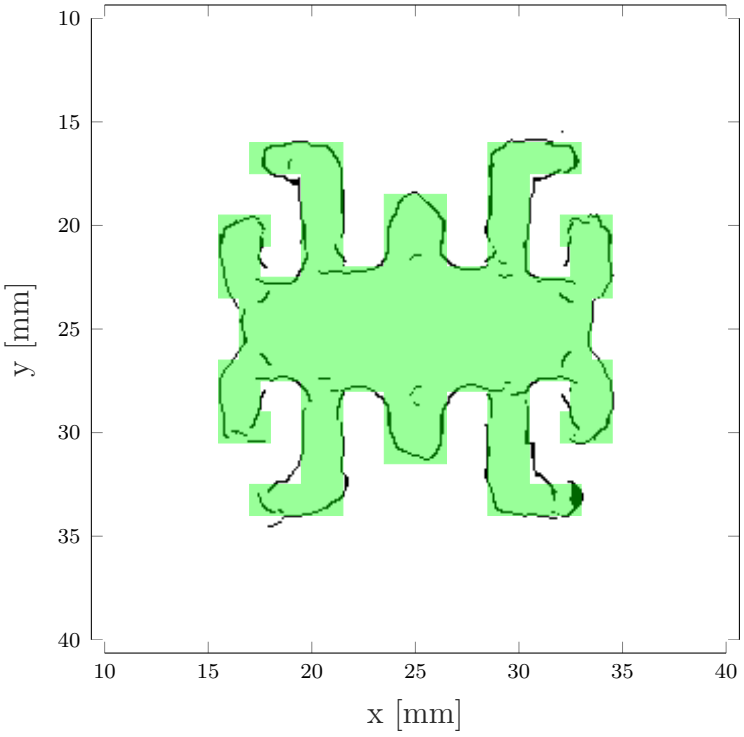

Figure E.2.7: Binary image for $p = 5$ and $\sigma = 3$.

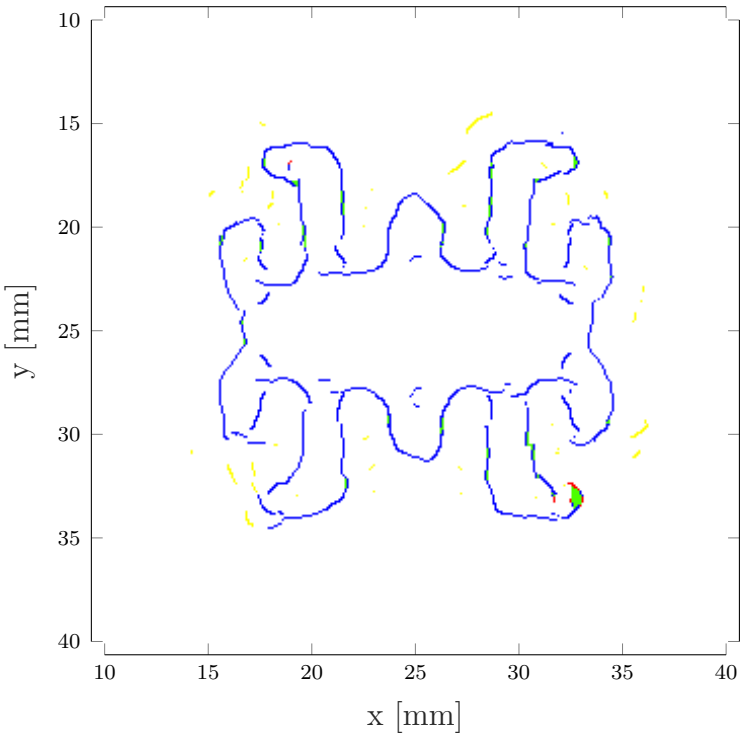

Figure E.2.8: Stages image with $p = 5$ and $\sigma = 3$.

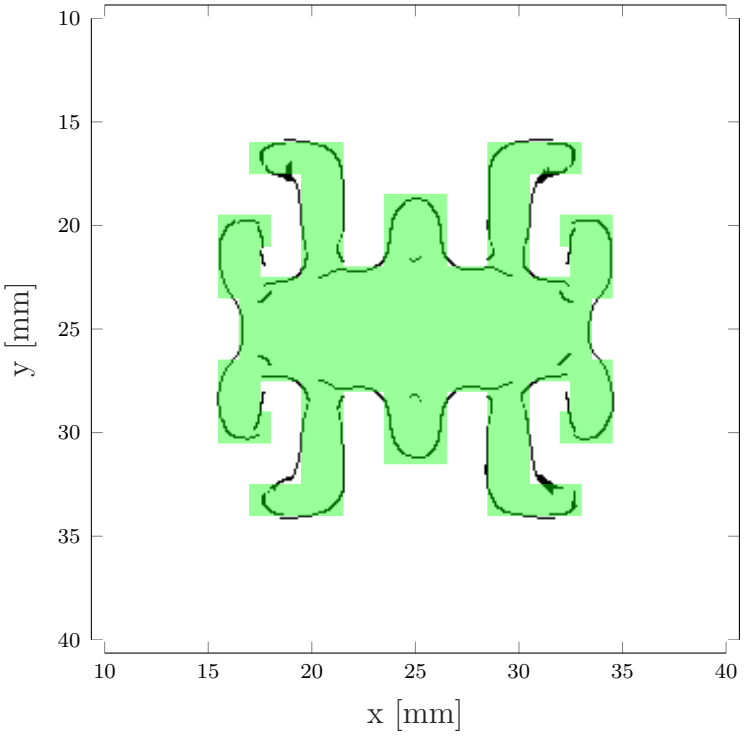

Figure E.2.9: Binary image for $p = 5$ and $\sigma = 5$.

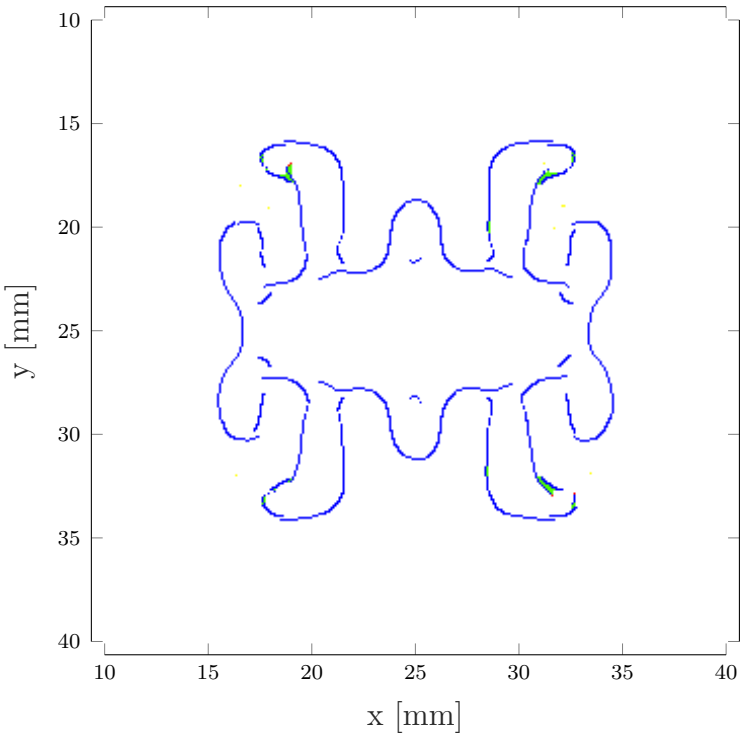

Figure E.2.10: Stages image with $p = 5$ and $\sigma = 5$.

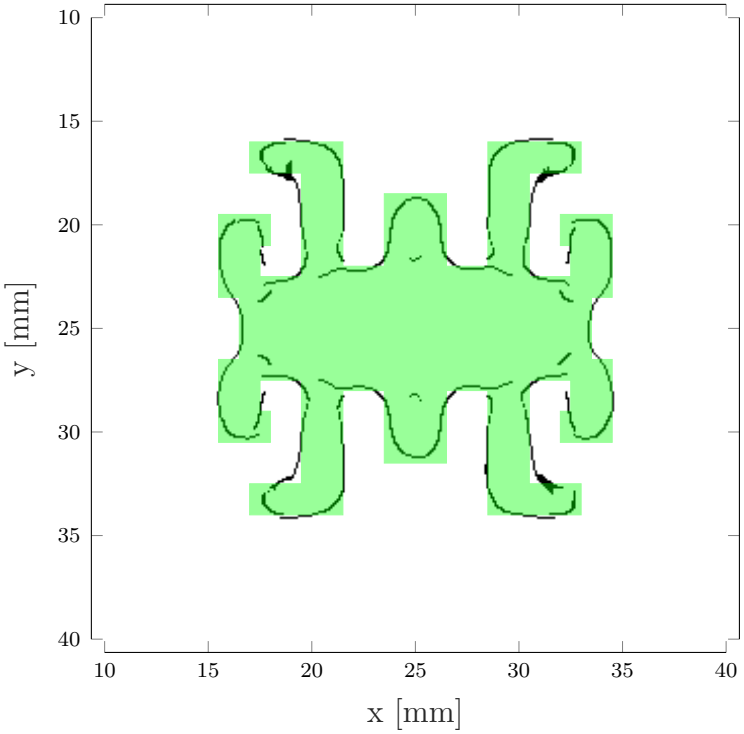

Figure E.2.11: Binary image for $p = 5$ and $\sigma = 5$.

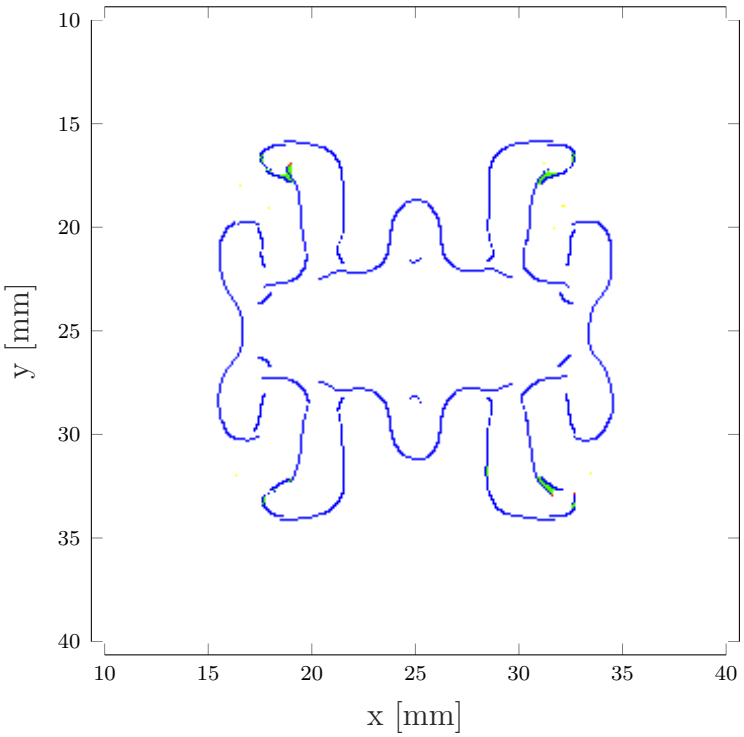

Figure E.2.12: Stages image with $p = 5$ and $\sigma = 5$ and optimized derivative kernel.

Appendix F

Peer-reviewed published articles

[1] A. Ratsakou, C. Reboud, A. Skarlatos, and D. Lesselier, "Fast models dedicated to simulation of eddy current thermography", in *Electromagnetic Non-Destructive Evaluation* (D. Lesselier and C. Reboud, eds.), vol. 43, (Saclay, France), pp. 175 – 182, IOS Press, 2018.

[2] A. Ratsakou, C. Reboud, A. Skarlatos, and D. Lesselier, "Fast simulation approach dedicated to infrared thermographic inspection of delaminated planar pieces", in *AIP Conference Proceedings*, vol. 2102, p. 120004, AIP Publishing, 2019.

[3] A. Ratsakou, C. Reboud, A. Skarlatos, and D. Lesselier, "Model based characterisation of delamination by means of thermographic inspection", in *Journal of Physics : Conference Series*, vol. 1476, p. 012005. 2020.

Electromagnetic Non-Destructive Evaluation (XXI)
D. Lesselier and C. Reboud (Eds.)

doi:10.3233/978-1-61499-836-5-175

Fast Models Dedicated to Simulation of Eddy Current Thermography

Almpion RATSAKOU [a,1], Christophe REBOUD [a], Anastasios SKARLATOS [a] and Dominique LESSELIER [b]

[a] *CEA, LIST, Centre de Saclay, Gif-sur-Yvette F-91191, France*
[b] *Laboratoire des Signaux et Systèmes (UMR8506, CNRS-CentraleSupélec-Univ. Paris Sud), Université Paris-Saclay, 91192 Gif-sur-Yvette cedex, France*

Abstract. This communication presents the first development aiming at efficiently simulating configurations of eddy current thermography for nondestructive evaluation. The numerical method proposed here is based on the Finite Integration Technique for both electromagnetic and thermal problems. Simulation results obtained using two different materials, steel and aluminum, are compared and discussed with respect to the presence of a flaw affecting the piece under test.

Keywords. Eddy current, thermography, simulation, finite integration technique

1. Introduction

The use of thermography [1] for nondestructive testing applications had received growing attention in the last years. This is mainly due to the fact that infrared (IR) cameras have recently improved significantly in both sensitivity and spatial resolution and that this technique is particularly adapted to many applications [2] such as composites' inspection. Unlike other direct imaging techniques, it is a fast, high resolution and contactless method. Thermal testing is generally divided into two main streams: passive and active. Passive thermography is defined as measuring the temperature difference between the target material and its surroundings under different ambient temperature conditions. Active thermography uses a thermal source in order to deposit heat in the target material. Most common sources consist in lamps or lasers [3] that heat part of the piece surface. These techniques of depositing heat on the materials have potential disadvantages, *e.g.* the reflected heat from the material can interfere with the measured signals, causing signal-to-noise-ratio (SNR) problems. For instance, many conductive materials when used in industry are coated or painted. The heating of the workpiece may also be obtained via the application of sonic or ultrasonic energy using a welding horn, *i.e.* vibrothermography, thermosonics or sonic infrared [4]. In this case, however, contact between the workpiece and the ultrasonic welding horn it is required, which can complicate its practical use and cause a loss of energy transmission.

[1]Corresponding Author: Almpion Ratsakou, CEA, LIST, Centre de Saclay, Gif-sur-Yvette F-91191, France; E-mail:almpion.ratsakou@cea.fr.

Eddy current thermography (ECT), also named as induction thermography, is an alternative to inspect metallic structures that does not suffer from the above-mentioned disadvantages. This is an emerging technology in nondestructive testing (NdT) that combines eddy current and thermography. ECT is based on electromagnetic induction and Joule effect heating. The technique uses induced eddy current to heat the sample and defect detection is based on the changes of the induced eddy current flow revealed by the thermal visualization captured by an IR camera. Induction thermography can be used to detect cracks [5], disbond, impact damage, delamination and corrosion.

This work presents a modelling approach using a two-dimensional numerical solver based on the Finite Integration Technique (FIT) [6,7]. A typical configuration, consisting of a coil located above a plate, is sketched in Figure 1. This configuration will be used in our simulations and an axial symmetry is assumed. The same numerical tool is used to solve both physical problems, namely the electromagnetic induction by the coil in the plate and the heat diffusion in the plate after excitation. Due to the large difference in time scale between the electromagnetic problem and the thermal one, a weak coupling of the two problems is possible.

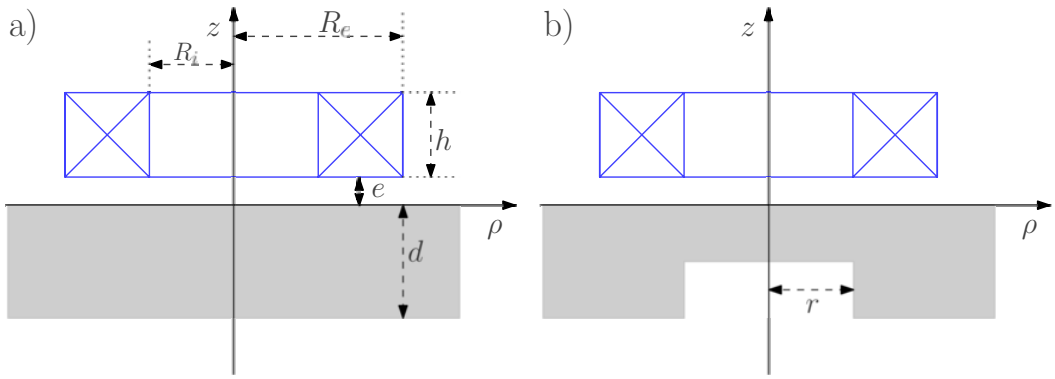

Figure 1. Schematic setup diagram. Circular coil of inner radius R_i, outer radius R_e and height h standing above a conductive plate of thickness d in a distance e. **a)** Homogeneous plate. **b)** Homogeneous plate with a axisymmetric defect of radius r.

In other words, the electromagnetic problem is first solved to calculate the time-dependent eddy current density induced in the plate, then it is converted into a heat source term by considering Joule effect. Finally, the diffusion of heat in the plate is computed with respect to time. This first development will serve as reference for further works, consisting in solving both problems with fast modal methods [8].

2. Theoretical formulation

ECT involves multi-physical interactions with electromagnetic-thermal phenomena including eddy current, Joule heating and heat conduction. Simulation of induction heating requires the ability to model multiple physical fields. Thus, modeling the generation of eddy current requires an electromagnetic solution in the workpiece, which results in a Joule heat distribution. The latter is used as a volumetric heating source in order to obtain the temperature distribution in the workpiece.

The coupling between the electromagnetic problem and the thermal one can often be further complicated by the fact that the electromagnetic properties of the workpiece are

depending on the temperature of the workpiece, which will lead to a strongly-coupled problem. This coupling of the two problems requires the electromagnetic solution to be computed based on a time/temperature updated set of materials properties. This leads to a time consuming numerical computation that can be avoided under some assumptions.

The induction heating process involves multiple time and length scales. Generally, the time scale associated with the heat transfer is much larger than the time scale associated with the electromagnetics. The time scale associated with the electromagnetic solution depends on the frequency f of the alternative current in the coil, while the time scale associated with the transient heat transfer in the workpiece is determined by its thermal properties. The length scale, for the electromagnetic problem, also depends on the frequency, as well on the magnetic permeability μ and electrical conductivity σ. The so-called *skin depth*, defined in the particular case of a half-space medium by the relation $\delta = (\pi\mu\sigma f)^{-1/2}$, illustrates the penetration of the electromagnetic field in the piece. As a consequence, the associated Joule effect is also generated in a depth range of two or three times the skin depth δ. From the numerical point of view, this implies that this particular region must be finely discretized.

2.1. The electromagnetic problem

In a typical configuration, a pulse generator emits a signal to an infrared camera and to a induction heater, which generates an excitation signal. This excitation signal is usually a sinusoidal of alternating current with high amplitude. The current is then driven into an inductive coil, which induces eddy current in the neighbouring workpiece. This phenomenon is described by the Maxwell's equations, which for the quasi-static approximation are

$$\nabla \times \mathbf{E} = -\frac{\partial \mathbf{B}}{\partial t}, \tag{1}$$

$$\nabla \times \mathbf{H} = \mathbf{J}, \tag{2}$$

$$\nabla \cdot \mathbf{B} = 0, \tag{3}$$

where $\mathbf{E}$ is the electric field intensity, $\mathbf{H}$ is the magnetic field intensity, $\mathbf{B}$ is the magnetic flux density, and $\mathbf{J}$ is the current density. Excitation frequencies are typically lower than 10 MHz, consequently the displacement current term $(\partial \mathbf{D}/\partial t)$ in (2) can be neglected. The above equations are combined with the following constitutive relations characterizing a linear, homogeneous and isotropic material

$$\mathbf{J} = \sigma \mathbf{E}, \qquad \mathbf{B} = \mu \mathbf{H}. \tag{4}$$

For solving the above differential equations and since $\mathbf{B}$ is divergence free, it can be expressed as $\mathbf{B} = \nabla \times \mathbf{A}$ where $\mathbf{A}$ is the magnetic vector potential. Substituting $\mathbf{B}$ into (1) and using (2) as well as the constitutive relations (4), the diffusion equation for the magnetic vector potential can be derived as:

$$\nabla \times \mu^{-1} \nabla \times \mathbf{A} + \sigma \frac{\partial \mathbf{A}}{\partial t} = \mathbf{J}_s \tag{5}$$

where $\mathbf{J}_s$ is the current density driving the inductor. The choice of a Coulomb gauge, $\nabla \cdot \mathbf{A} = 0$, is made here.

The FIT method provides a discrete reformulation of Maxwell's equations on its integral form. A typical simulation task is described by a known geometry and material configuration, as well as boundary and initial conditions. In the following a rectangular cubic cell complex consisting of a material grid complex $\mathbf{M}$, a primary grid complex $\mathbf{G}$ and a dual grid complex $\widetilde{\mathbf{G}}$ will be used.

The eddy current density in FIT is computed by the equation

$$\widetilde{\mathbf{C}}\mathbf{M}_{\mu}^{-1}\mathbf{C}\widehat{\mathbf{a}} - \mathbf{M}_{\sigma}\dot{\widehat{\mathbf{a}}} = \widehat{\widehat{\mathbf{j}}} \tag{6}$$

where $\widetilde{\mathbf{C}}$ and $\mathbf{C}$, contain only topological information and represent a discrete curl-operator on the primary and the dual grid $\mathbf{G}$ and $\widetilde{\mathbf{G}}$, respectively, $\mathbf{M}_{\mu}^{-1}$, $\mathbf{M}_{\sigma}$, are the material matrices, $\widehat{\mathbf{a}}$ is the magnetic vector potential and $\widehat{\widehat{\mathbf{j}}}$ is the current density.

Initial conditions of the model assume a thermal equilibrium of the sample and its surroundings. In the z-direction Neumann boundary conditions are imposed. On the artificial left side boundary, at $\rho = 0$ where the axis of the symmetry is, Neumann condition is imposed too. On the right side boundary, at $\rho = \rho_e$ Dirichlet boundary condition is imposed. We suppose that the workpiece is infinite in the ρ-direction so this artificial boundary does not affect the solution within the domain of interest.

2.2. The thermal problem

Due to resistive heating from the induced eddy current, the temperature of conductive materials increases, which is known as Joule heating. It can be expressed by the equation

$$\dot{Q} = \frac{1}{\sigma}\,|\mathbf{J_s}|^2,$$

where the sum of generated power density $\dot{Q}$ is proportional to the square of the eddy current density. The resistive heat will diffuse as a time transient until an equilibrium state is restored between the bulk and its surface, or better saying the workpiece and the environment. The thermal part of the problem can be divided into two phases, *(i)* the heating phase, during which the heat is being deposited in the workpiece and *(ii)* the cooling phase, when the workpiece has reached a maximum temperature, the deposit of heat has stopped, and only diffusion of the heat is occurring in the plate.

Starting with the energy conservation law in integral form

$$\int_V \varrho\, C_p \frac{\partial T}{\partial t}\,\mathrm{d}V = \int_V \dot{Q}\,\mathrm{d}V - \oint_{\partial V} \mathbf{J}\cdot\,\mathrm{d}\mathbf{s} \tag{7}$$

and using the Fourier's law $\mathbf{J} = -\kappa\nabla T$, the heat equation is derived as

$$-\kappa\nabla^2 T + \varrho\, C_p \frac{\partial T}{\partial t} = \dot{Q}, \tag{8}$$

where κ is the thermal conductivity, ϱ the density, C_p the specific heat and T the temperature.

In the FIT, the solution of the thermal problem is given by the equation

$$\widetilde{\mathbf{S}}\mathbf{M}_{\kappa}\mathbf{G}\theta - \mathbf{M}_{c}\dot{\theta} = -\dot{\mathbf{q}}, \tag{9}$$

which is a discrete formulation for the heat equation, where $\widetilde{\mathbf{S}}$ is the div-operator on the dual grid, $\mathbf{M}_{\kappa}$, $\mathbf{M}_{c}$ are material matrices, $\mathbf{G}$ is the discrete gradient matrix, θ the temperature and $\dot{\mathbf{q}}$ the source term.

Pairing this equation with the boundary conditions, the temperature of the workpiece and its surrounding is computed. The boundary conditions that are used here are the same as in the electromagnetic problem.

3. Simulation and results

For the simulations a circular coil is used with $e = 1$ mm of lift-off and inner radius $R_i = 11$ mm, outer radius $R_e = 84$ mm, height $h = 41$ mm and number of wire-turns $N = 408$ as in [9]. For modeling the workpiece, two different materials are used: (i) Aluminum, (ii) Steel, their respective physical parameters being given in Table 1. We are investigating here two scenarios. In the first case, we compare the behaviours of two homogeneous plates of thickness $d = 10$ mm, made of aluminum and steel, respectively. In the second case, we introduce a defect, which can be assumed to be a corrosion, at the bottom surface of a thin plate ($d = 1$ mm) of aluminum. The defect is modelled as a local change of physical properties (same as the surrounding environment). The excitation signal is considered to be a sinusoid of frequency f. Setting the frequency of the excitation signal at $f = 200$ Hz and the duration of the signal at 50 ms we probe the two different plates with 10 periods of the signal. In Figure 2, the images of the simulation for three crucial times are given. In the first two rows, for which no diffusion has been occurring, the skin depth effect is highlighted, i.e. the difference of the electromagnetic properties of the materials.

As one can expect, through the Joule effect, the penetration depth of the eddy currents in the aluminum plate is much larger than in the workpiece of steel. The difference between both rows of images is a result of the difference of the thermal properties of the materials. A corrosion has been now introduced in a thick aluminum plate. The frequency of the probed signal has been kept the same, at 200 Hz, which gives a penetration depth of 6 mm, much larger than the thickness of the plate. The defect has been modeled as a circular discontinuity in the plane (ρ, θ) of radius $r = 3$ cm or 5 cm and a thickness of 0.5 mm in the z-direction. The results of the simulation of this setup are given in Figure 3.

Since only the infrared radiation emitted by the surface of the workpiece as a function of time can be captured by a thermal camera, in Figure 4 and Figure 5 the surface temperatures are plotted. In Figure 4, the temperature of the the workpiece on the sur-

Table 1. Electromagnetic and thermal parameters of the materials.

	μ_r	σ (S/m)	κ (W/m/K)	ϱ (Kg/m^3)	C_p (J/Kg/K)
Aluminum case	1	3.5×10^7	237	2707	897
Steel	700	3.21×10^6	44.5	7850	475

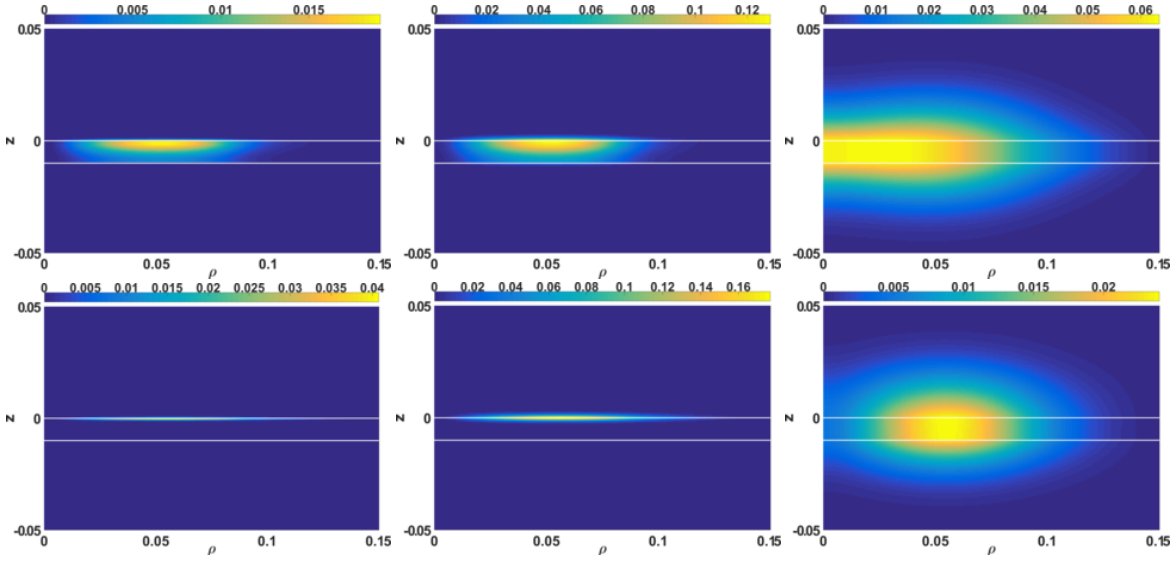

Figure 2. Temperature distribution images in the region of interest for different time and homogeneous materials without defects.
Top: Aluminum. *Left to the right:* Different observation times, $t = t_0$, $t = t_0 + 50$ ms, $t = t_0 + 5$s.
Bottom: Steel. *Left to the right:* Different observation times, $t = t_0$, $t = t_0 + 50$ ms, $t = t_0 + 5$s.

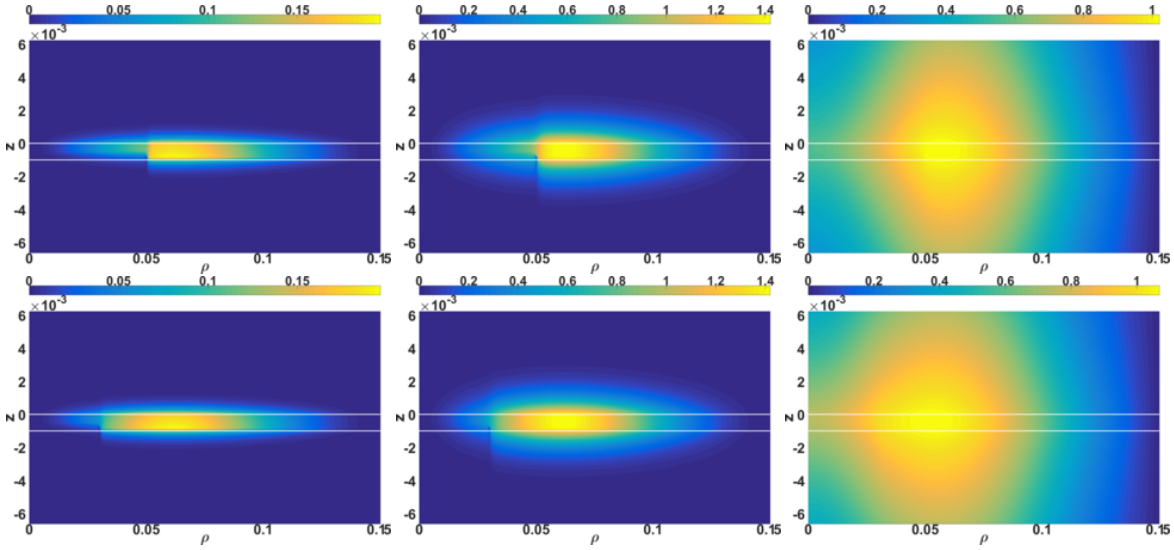

Figure 3. Temperature distribution images in the region of interest for different time and an aluminum plate with defect.
Top: Discontinuity radius: 5 cm. *Bottom:* Discontinuity radius: 3 cm.
Left to the right: Different observation times, $t = t_0$, $t = t_0 + 50$ ms, $t = t_0 + 5$s.

face, when the radius of the corrosion is 5 cm, is plotted compared with the case of the undamaged plate. In Figure 5 the results with a corrosion of radius of 3 cm are given. Since the position of the thermal camera is not fixed, *i.e.* we can have thermal images on both sides of the plate, the difference of temperature is shown in both surfaces.

On both cases, the information about the defect is clear for early times where we are able to distinguish its edges, *i.e.* the size of the defect in the ρ-direction is well defined. When diffusion occurs, the temperature curves of the damaged and undamaged plate are close. In the case of the smaller defect, still we can see that there is a defect in the workpiece but it is impossible to locate its edges. On the other hand, when the defect's

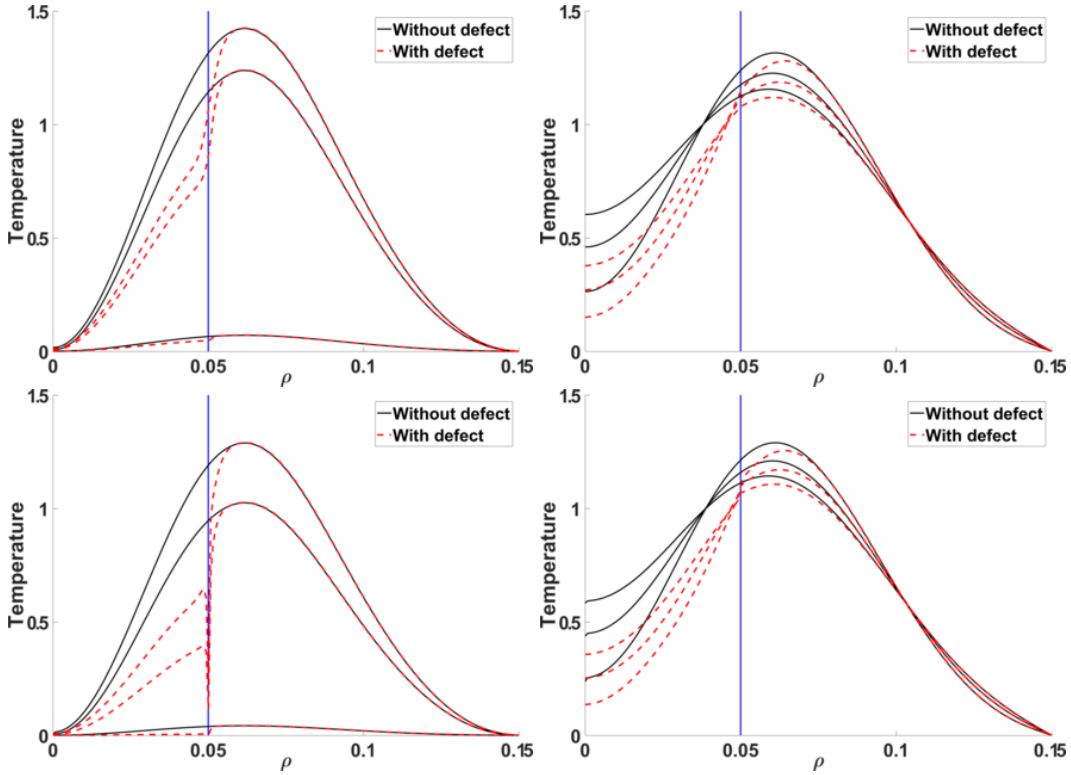

Figure 4. Comparison of the distribution of temperature at the surfaces of the plates with and without defect for different observation times. Defect's radius $r = 5$ cm. *Top:* Upper surface, *Bottom:* Bottom surface. Different observation time: *Left:* 10, 50, 70 ms *Right:* 1, 2, 3s

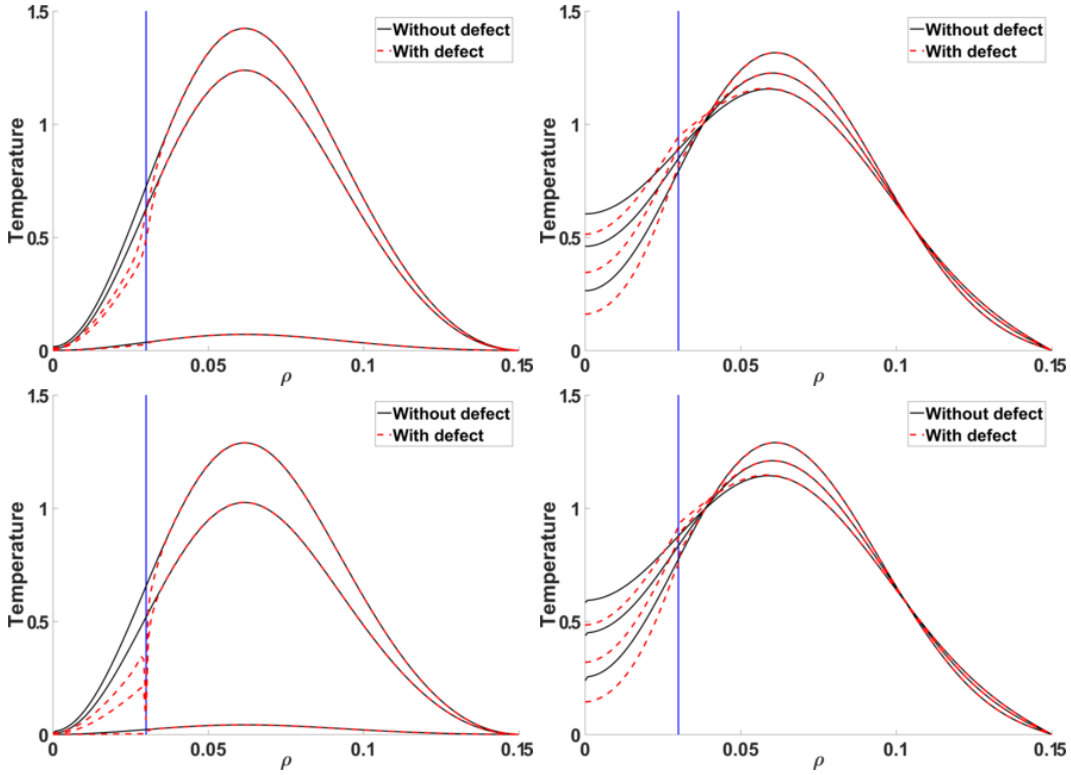

Figure 5. Comparison of the distribution of temperature at the surfaces of the plates with and without defect for different observation times. Defect's radius $r = 3$ cm. *Top:* Upper surface, *Bottom:* Bottom surface Different observation time: *Left:* 10, 50, 70 ms *Right:* 1, 2, 3s

radius is 5 cm, even after 5 seconds the localization of the edges of the defect can be easily achieved through those curves. In general, in ECT we are interested on early times when the difference of the electromagnetic and thermal properties of the workpiece can highlight any presence of a damage on it and this is well shown by the previous results.

4. Conclusions and perspectives

To conclude, a 2D numerical solver based on the finite integration technique has been implemented and used to simulate the behaviour of different materials under inspection by means of eddy current thermography. Both electromagnetic and thermal problems are coupled in a weak way, taking advantage of the large difference between their characteristic time constants. Possible generalizations of this solver are the development of a 3D version or the investigation of strong coupling in the calculation process.

The use of such a numerical solver is important to investigate easily some aspects like effect of piece inhomogeneity or anisotropy, however it can lead to heavy calculations and complicated meshing considerations when addressing 3D configurations. For this reason, this tool will later be used in complement of fast modal methods to adress 3D cases involving canonical geometries like a stratified planar medium.

References

[1] X. Maldague and P. Moore. Infrared and Thermal Testing Nondestructive Testing Handbook, vol. 3. *American Society for Nondestructive Testing*, 2001.

[2] X. Maldague. *Theory and Practice of Infrared Technology for Nondestructive Testing*. Wiley, 2001.

[3] X. Maldague. Introduction to ndt by active infrared thermography. *Materials Evaluation*, 60(9):1060–1073, 2002.

[4] U. Polimeno, D. P. Almond, B. Weekes, and E. W. J. Chen. A compact thermosonic inspection system for the inspection of composites. *Composites Part B: Engineering*, 59:67–73, 2014.

[5] C. Xu, N. Zhou, J. Xie, X. Gong, G. Chen, and G. Song. Investigation on eddy current pulsed thermography to detect hidden cracks on corroded metal surface. *NDT & E International*, 84:27–35, 2016.

[6] R. Marklein. The Finite Integration Technique as a general tool to compute acoustic, electromagnetic, elastodynamic and coupled wave fields. *Review of Radio Science*, 1999.

[7] T. Weiland. A discretization model for the solution of Maxwell's equations for six-component fields. *Archiv Elektronik und Uebertragungstechnik*, 31:116–120, 1977.

[8] T. Theodoulidis and E. Kriezis. *Eddy Current Canonical Problems (with Applications to Nondestructive Evaluation)*. Tech Science Press, 2006.

[9] N. J. Siakavellas. The influence of the heating rate and thermal energy on crack detection by eddy current thermography. *Journal of Nondestructive Evaluation*, 35(2), 2016.

Fast Simulation Approach Dedicated to Infrared Thermographic Inspection of Delaminated Planar Pieces

Almpion Ratsakou[1,a)], Christophe Reboud[1], Anastassios Skarlatos[1] and Dominique Lesselier[2]

[1]*CEA, LIST, Centre de Saclay, Gif-sur-Yvette F-91191, France*
[2]*Laboratoire des Signaux et Systèmes (UMR8506, CNRS-CentraleSupélec-Univ. Paris Sud), Université Paris-Saclay, 91192 Gif-sur-Yvette cedex, France*

[a)]Corresponding author: almpion.ratsakou@cea.fr

Abstract. In the present work, we propose a semi-analytical model based on the so-called truncated region eigenfunction expansion method, for the simulation of thermographic inspection. The problem is solved in the Laplace domain with respect to time, and the temperature distribution is approximated by its expansion on a tensor product basis. Configurations addressed by this model are stratified planar pieces affected by thin delamination flaws. Considered sources are lamps providing a thermal excitation at the surface of the inspected piece. The description of the delamination defects as thin air gaps between the piece layers proves to be equivalent with the introduction of a surface resistance to the heat flow, thus allowing their treatment via the applied modal approach without additional discretisation.

INTRODUCTION

Thermal/infrared non-destructive testing (T/INDT) techniques [1] have received growing attention in recent years thanks to their advantages, that is, fast, high resolution and contact-less, control, and benefiting form the technological progress in the infrared cameras and data acquisition equipment. The detection of irregularities is based on the principle that all bodies emit infrared radiation when their temperature is above 0 K. The emitted infrared radiation can be measured by infrared cameras, and the images are then analysed for the detection and characterization of flaws. Subsurface irregularities will affect the heat diffusion rate leading to a thermal contrast on the surface of the homogeneous work-piece. By analysing alterations or the contrast in the thermal pattern of the material surface, one can obtain information about subsurface flaws.

Simulation of TNDT procedures involves at a first step the solution of the heat conduction problem in the considered work-piece, with and without defects, in order to obtain the temperature distribution at the piece interfaces, which constitutes the measurement. The full solution to this problem can be obtained using a numerical technique like the finite elements method (FEM) or the finite integration technique (FIT). Nevertheless, in practical situations it is often meaningful to renounce the detailed information of the complete numerical solution in favour of fast analytical or semi-analytical approximations, which hold the essence of the thermal flow behaviour. A very popular, well-established approach is the so-called thermal quadrupoles method, where the original tree dimensional problem is approximated as a multilayer one dimensional problem (by ignoring the heat flow in the lateral layers directions) and modelled as a cascade of "quadrupoles" in analogy with the electrical network theory [2].

Should the lateral propagation be taken into account, the quadrupole approach can be extending by taking the Fourier transform of the solution along these directions and forming an one dimensional problem per spatial frequency. Mathematically speaking, this is equivalent with stating that the Fourier basis diagonalises the part of the operator standing for the lateral propagation, thus allowing us to treat the problem as a set of independent one dimensional problems. This approach is, however, not valid in case where defects are present since the Fourier basis is not an eigenbasis of the operator any more. In order to address this problem a more general approach should be followed.

Such an approach based on the artificial truncation of the computational domain, referred to in the literature as

45th Annual Review of Progress in Quantitative Nondestructive Evaluation, Volume 38
AIP Conf. Proc. 2102, 120004-1–120004-10; https://doi.org/10.1063/1.5099846
Published by AIP Publishing. 978-0-7354-1832-5/$30.00

the truncated region eigenfunction expansion (TREE), has been successfully applied in the electromagnetism for the solution of magnetostatic and low-frequency (eddy-current) problems [3, 4, 5, 6]. Defects can be modelled directly as part of the geometry like in [4, 5, 6], or indirectly by first applying the TREE method to construct the Green's function accounting for the geometry of the flawless piece and treating the defect as a perturbation by solving the appropriate integral equation [7, 8, 9].

In a previous work [10], a dedicated two-dimensional numerical solver based on FIT [11, 12] has been used for studying volumetric defects in planar multilayer media, consisting of steel and aluminium sheets. In this communication, the TREE method will be extended in order to treat arbitrarily shaped delamination defects in steel-aluminium multilayer specimens, like those of [10]. Delamination flaws are entirely confined between the structure layers and hence can be modelled as inter-layer resistance patches, making modal approaches like the TREE method applicable. The temporal part of the solution is treated as in the quadrupole method via the Laplace transform. The semi-analytical solutions developed for a number of case studies will be compared with the numerical results obtained via the COMSOL Multiphysics® simulation platform [13].

THEORETICAL DESCRIPTION OF THE PROBLEM

Classical heat conduction solutions have been summarized by Carslaw and Jaeger [14] in late 50s and are widely used for calculating the temperature field inside homogeneous or isotropic materials. In our case, a general heat diffusion model of a multi-layered structure, with respect to the $z-$direction, is described by the following expressions:

$$\frac{1}{a^{(i)}}\frac{\partial T^{(i)}(x,y,z,t)}{\partial t} = \frac{\partial^2 T^{(i)}(x,y,z,t)}{\partial x^2} + \frac{\partial^2 T^{(i)}(x,y,z,t)}{\partial y^2} + \frac{\partial^2 T^{(i)}(x,y,z,t)}{\partial z^2}, \qquad i = 1,\ldots,M \tag{1}$$

$$T^{(i)}\Big|_{t_0} = T_{in} \tag{2}$$

$$T^{(i)}\Big|_{z_j} = T^{(i+1)}\Big|_{z_j} \tag{3}$$

$$-k^{(i)}\left.\frac{\partial T^{(i)}}{\partial z}\right|_{z_j} = -k^{(i+1)}\left.\frac{\partial T^{(i+1)}}{\partial z}\right|_{z_j}. \tag{4}$$

Here $T^{(i)}$ is the temperature in the i-th region, M is the number of layers, T_{in} is the temperature of the work piece at the initial time t_0, $a^{(i)} = k^{(i)}/\left(\rho^{(i)}C_p^{(i)}\right)$ is the thermal diffusivity in the i-th region, $k^{(i)}$ is the thermal conductivity, $\rho^{(i)}$ is the material density, $C_p^{(i)}$ is the heat capacity and t is the time variable. The heat diffusion phenomenon is described by the Equation 1. Equation 3 and 4 describe the continuity of the temperature and the continuity of the thermal flux at the interface between layers i and $i+1$, respectively. For simplicity, our model consists of two thin metallic plates, above and below them thick layers of air will complete the physical configuration. In Fig. 1, a two dimensional projection on the $xz-$plane of the a general set-up is depicted.

The work piece is thermally excited by a flash lamp set above the work piece. This excitation is modelled in terms of an additional thermal flux J_e at the interface between the first and second layer of the model and perpendicular to that interface. The introduction of the source flux requires the modification of the flux continuity condition in Equation 4 as follows:

$$T^{(1)}\Big|_{z=0} = T^{(2)}\Big|_{z=0} \tag{5}$$

$$-k^{(1)}\left.\frac{\partial T^{(1)}}{\partial z}\right|_{z=0} = -k^{(2)}\left.\frac{\partial T^{(2)}}{\partial z}\right|_{z=0} + J_e. \tag{6}$$

Let us introduce some flaws in the model. These flaws will be modelled as very thin air gaps between the two metallic plates, *i.e.* the second and the third layer. By modelling the flaws as very thin with respect to the $z-$ coordinate, they can be represented by a thermal resistance $R(x,y)$ between the two layers. The effect of the flaws can be taken into account by modifying the continuity relation at the interface of the two layers. By applying the Fourier's law between the fictitious surfaces of the flaw we have the new continuity condition between the second and third layer

$$T^{(1)}\Big|_{z=-d_1} = T^{(2)}\Big|_{z=-d_1} - R(x,y)\left.\frac{\partial T^{(1)}}{\partial z}\right|_{z=-d_1} \tag{7}$$

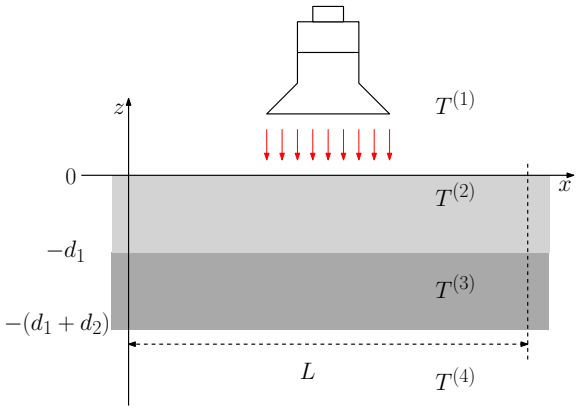

FIGURE 1. Two-dimensional illustration of a typical thermographic inspection consisting of a double-layered piece of two different materials illuminated by a flash lamp.

$$-k^{(1)}\left.\frac{\partial T^{(1)}}{\partial z}\right|_{z=-d_1} = -k^{(2)}\left.\frac{\partial T^{(2)}}{\partial z}\right|_{z=-d_1}. \tag{8}$$

THE TREE FORMULATION

The boundary value problem described by Equations 1 – 8 will be solved in the Laplace domain with respect to time. However, the solution of the problem with the TREE method requires the truncation of the solution domain. That is done with respect to $x-$coordinate and $y-$coordinate. This is physically valid if these limits are set far away from the region of interest or just at a distance large enough so as the flaws of the work-piece do not interfere with the boundaries. To truncate the solution domain we have to impose boundary conditions at $x = 0, x = L_x$ and $y = 0, y = L_y$. Dirichlet boundary conditions, see Equation 9 and 10, Neumann boundary conditions, see Equation 11 and 12, or even mixed boundary conditions can be used indifferently, an advantage of this method being the ability to handle a variety of boundary conditions.

$$T^{(i)}\Big|_{x=0} = T^{(i)}\Big|_{x=L_x} = 0 \tag{9}$$

$$T^{(i)}\Big|_{y=0} = T^{(i)}\Big|_{y=L_y} = 0 \tag{10}$$

or

$$\left.\frac{\partial T^{(i)}}{\partial x}\right|_{x=0} = \left.\frac{\partial T^{(i)}}{\partial x}\right|_{x=L_x} = 0 \tag{11}$$

$$\left.\frac{\partial T^{(i)}}{\partial y}\right|_{y=0} = \left.\frac{\partial T^{(i)}}{\partial y}\right|_{y=L_y} = 0. \tag{12}$$

In our case, we will apply Dirichlet boundary conditions in both directions.

The formal solution for the temperature field in the Laplace domain reads

$$T^{(1)} = \sum_{m=1}^{M}\sum_{n=1}^{N} C_{mn}^{(1)} e^{-\eta_{mn}^{(1)} z}\sin(\kappa_m x)\sin(\lambda_n y) \tag{13}$$

$$T^{(2)} = \sum_{m=1}^{M}\sum_{n=1}^{N}\left[C_{mn}^{(2)} e^{-\eta_{mn}^{(2)}(z+d_1)} + D_{mn}^{(2)} e^{\eta_{mn}^{(2)} z}\right]\sin(\kappa_m x)\sin(\lambda_n y) \tag{14}$$

$$T^{(3)} = \sum_{m=1}^{M}\sum_{n=1}^{N}\left[C_{mn}^{(3)}e^{-\eta_{mn}^{(3)}(z+d_1+d_2)} + D_{mn}^{(3)}e^{\eta_{mn}^{(3)}(z+d_1)}\right]\sin(\kappa_m x)\sin(\lambda_n y) \tag{15}$$

$$T^{(4)} = \sum_{m=1}^{M}\sum_{n=1}^{N} D_{mn}^{(4)}e^{\eta_{mn}^{(4)}(z+d_1+d_2)}\sin(\kappa_m x)\sin(\lambda_n y) \tag{16}$$

the discrete eigenvalues κ_m and λ_n being determined by the truncation conditions in the x and y direction, respectively, as follows:

$$\begin{aligned}\sin(\kappa_m L_x) &= 0, \quad \kappa_m = \frac{m\pi}{L_x}, \quad m \in \mathbb{Z}^* \\ \sin(\lambda_n L_y) &= 0, \quad \lambda_n = \frac{n\pi}{L_y}, \quad n \in \mathbb{Z}^*\end{aligned}$$

M and N being the truncation limits and $\eta_{mn}^{(i)}$ being calculated using the dispersion equation

$$\begin{aligned}-\kappa_m^2 - \lambda_n^2 + \eta_{mn}^2 - \frac{s}{a^{(i)}} &= 0 \\ \eta_{mn}^{(i)} &= \sqrt{\kappa_m^2 + \lambda_n^2 + \frac{s}{a^{(i)}}}.\end{aligned}$$

According to Equation 6, the excitation term is expressed by means of a given thermal flux $J_e(x, y)$ at the interface between the first and the second layer, at $z = 0$. Applying the Fourier's law, one obtains

$$J_e(x, y) = -k^{(1)}\frac{\partial T^{(e)}}{\partial z} \tag{17}$$

which using Equation 17 and substituting the expression for the temperature field from Equation 14 yields

$$J_e(x, y) = -k^{(1)}\sum_{m=1}^{M}\sum_{n=1}^{N}\eta_{mn}^{(1)}C_{mn}^{(e)}\sin(\kappa_m x)\sin(\lambda_n y) \tag{18}$$

If we assume that $J_e(x, y)$ has the form of a rectangular patch exceeding from x_1 to x_2 and from y_1 to y_2 with $0 < x_1 < x_2 < L_x$ and $0 < y_1 < y_2 < L_y$ the coefficients for the excitation term can be calculated explicitly according to

$$C_{mn}^{(e)} = -\frac{A}{k^{(1)}\eta_{mn}^{(1)}}\int_{y_1}^{y_2}\int_{x_1}^{x_2}\sin(\kappa_m x)\sin(\lambda_n y)\,\mathrm{d}x\,\mathrm{d}y \tag{19}$$

where A is the constant intensity of the source.

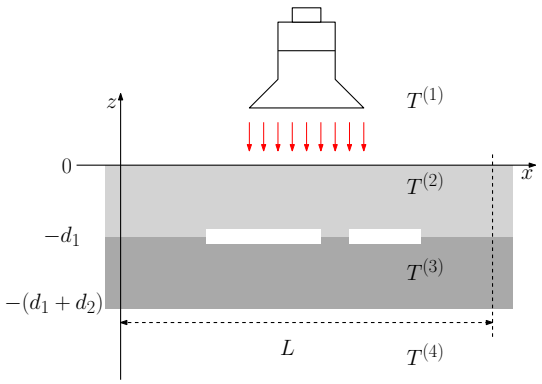

FIGURE 2. Sketch of a 2-layer medium with delaminations

At this point, we consider the same case of the double-layer medium but this time we assume that the contact between the two layers is imperfect in a sub-domain of their interface as depicted in Fig. 2. This kind of imperfect contact between the two layers can model a very thin delamination. In this case, the effect of the delamination can be taken into account by only modifying locally the continuity relation between the two layers. To be more specific, let us consider a very thin defect between two planar media as shown in Fig. 3, where $\mathcal{D}$ is the region of the delamination, Δz is the size of this area in the $z-$direction, S_a and S_b are two fictitious surfaces parallel to the interface between the two layers at a distance $\Delta z/2$ from it each. By applying the Fourier's law between the fictitious surfaces S_a and S_b one has

$$\begin{aligned} J_z &= -k_d \nabla T \\ J_z &= -k_d \frac{T^{(2)} - T^{(3)}}{\Delta z} \end{aligned}$$

which leads to

$$T^{(2)} - T^{(3)} = -R(x,y) J_z \tag{20}$$

where J_z is the heat flux in the $z-$direction and $R(x,y)$ represents the resistance between the two layers defined as

$$R(x,y) = \frac{\Delta z}{k_d}, \qquad (x,y) \in \mathcal{D}$$

inside the flaw domain $\mathcal{D} \in (0, L_x) \times (0, L_y)$ and valued to zero elsewhere. Here, Δz is the size of the delamination in the $z-$direction and k_d is the thermal conductivity of the flaw, which is air in our case.

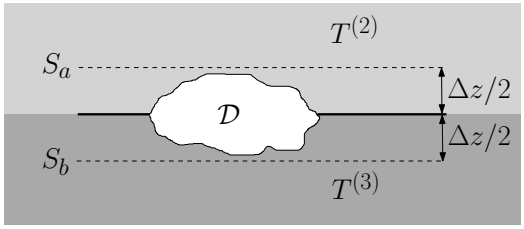

FIGURE 3. Modelling the delamination

We denote J_{z_2} and J_{z_3} as the heat flux for the second and third layer, respectively. Since $J_{z_2} = J_{z_3}$, by the continuity of the thermal flux at the interface, Equation 20 becomes

$$T^{(2)} - T^{(3)} = -\frac{\Delta z}{k_d} J_z \tag{21}$$

where $T^{(2)}$ and $T^{(3)}$ will be replaced by their series expressions.

The set of continuity relations is then written as a linear system of equations after the application of the Galerkin method. The result can be written in matrix form:

$$[\mathbf{A}][\mathbf{X}] = [\mathbf{B}] \tag{22}$$

where $\mathbf{X}$ contains the unknown coefficients C_{mn} and D_{mn}. The matrix $\mathbf{A}$ has to be numerically inverted in order to calculate the unknown coefficients. This matrix is a block tridiagonal matrix. The right hand side of the system, $\mathbf{B}$, is sparse as it differs from 0 only in the lines which correspond to interfaces where sources may be found, excitations or delaminations. By calculating the matrix $\mathbf{X}$ the solution of the problem can be numerically evaluated in the discretised space domain of interest using Equation 13–16. The results are the solution of the problem in the Laplace domain. The temperatures can be calculated in the time domain, by numerical inversion of the obtained solution in the Laplace domain.

For the inverse Laplace transformation the Stehfest's algorithm is used [15, 16], which is an improved variant of Gaver's method [17]. If $F(s)$ is the known Laplace transform of the function $f(t)$, evaluated at $s = a_j/t$ where

$a_j = j\ln(2)$, then an approximate value of this function at time t can be calculated as

$$f(t) \cong \frac{\ln(2)}{t} \sum_{J=1}^{N} V_j F\left(j\frac{\ln(2)}{t}\right). \tag{23}$$

The coefficients V_j are given by the following expression for an even value of N:

$$V_j = (-1)^{j+N/2} \sum_{k=Int((j+1)/2)}^{Min(N/2,j)} \frac{k^{N/2(2k)!}}{(N/2-k)!k!(k-1)!(j-k)!(2k-j)!}. \tag{24}$$

In this equation 'Int' designates the integer part of a real number and 'Min' the minimum of two numbers.

NUMERICAL RESULTS

The three-dimensional model has been tested for the two inspection scenarios depicted in Fig. 4, following the experimental configuration described in [18]. A flash lamp producing a heating power density of $Q = 10^6 W/m^2$ on the surface of the work-piece, is used for excitation. The flash has been modelled as a Dirac's delta function in time, whereas its spatial part is considered as uniform. The inspected material consists of two metallic plates of equal thickness, i.e. $d_1 = d_2 = 2.5$ mm. The top layer is a steel plate and the bottom one, an aluminium plate. The computational region has been truncated at $L_x = 50$ mm and $L_y = 50$ mm.

In the first configuration, shown on the left part of Fig. 4, a single rectangular delamination flaw is considered. The flaw dimensions are 10×10 mm in the $xy-$plane, and its thickness is taken equal to $d = 10^{-3}$ mm. The flaw is located at the centre of the plate. The spatial support of the source, flash lamp, is a square of 30 mm side, and it is also centred in the middle of the plate. In the second case, depicted on the right side of Fig. 4, the plate is affected by two rectangular flaws of different sizes, but of same thickness. The lateral dimensions of the defects in the $xy-$plane are 5×10 mm and 10×10 mm, respectively. The spatial support of the source in this case is a square of 45 mm centred in the middle of the plate, as in the first case.

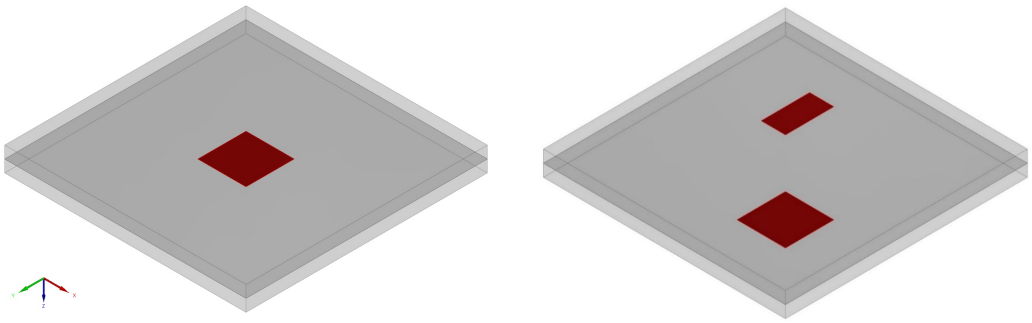

FIGURE 4. The three-dimensional configurations of the work-piece. *Left:* Single-flaw configuration including a $10 \times 10 \times 10^{-3}$ mm void inclusion centred between the two layers. *Right:* Multi-flaw configuration including a $10 \times 10 \times 10^{-3}$ mm and a $5 \times 10 \times 10^{-3}$ mm void inclusion between the two layers.

TABLE 1. Thermophysical properties of materials.

Bulk material	**Thermal conductivity** k $[W/mK]$	**Heat capacity** C_p $[J/kgK]$	**Density** ρ $[kg/m^3]$
Aluminium	237	897	2707
Steel	44.5	475	7850
Air	0.02454	1005	1.1843

In Fig. 5 and 6 the temperature distribution at the front and the rear surface is shown for the single-flaw configuration at 0.0408 and 0.2143 s, respectively. Fig. 7 and 8, show the same results for the second configuration. The two figures illustrated how the heat diffusion is affected by the presence of the flaw.

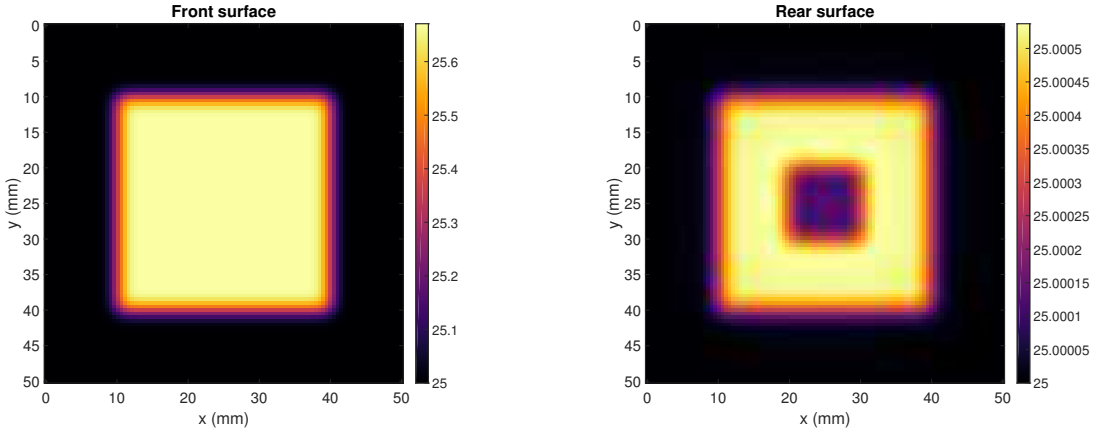

FIGURE 5. Simulated surface temperature field at time 0.0408 second for single-flaw configuration. *Left:* Top surface. *Right:* Bottom surface.

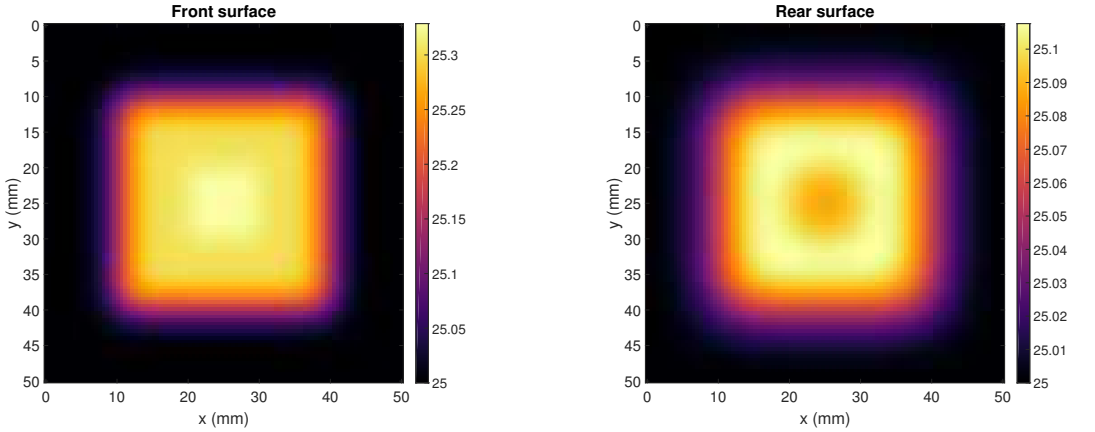

FIGURE 6. Simulated surface temperature field at time 0.2143 second for single-flaw configuration. *Left:* Top surface. *Right:* Bottom surface.

In order to proceed to a quantitative comparison of the above presented solution the same problem has been solved using a commercial numerical modelling software, the heat transfer module of COMSOL Multiphysics® [13]. The numerical solver of COMSOL Multiphysics® is based on the finite elements method using a time stepping technique.

The heat equation treated with the COMSOL Multiphysics® solver reads

$$\rho C_p \frac{\partial T}{\partial t} + \nabla \cdot \mathbf{q} = Q \tag{25}$$

where $\mathbf{q} = -\mathbf{k}\nabla T$. The source is described as surface condition at $z = 0$ as

$$-\mathbf{n} \cdot \mathbf{q} = Q_b \tag{26}$$

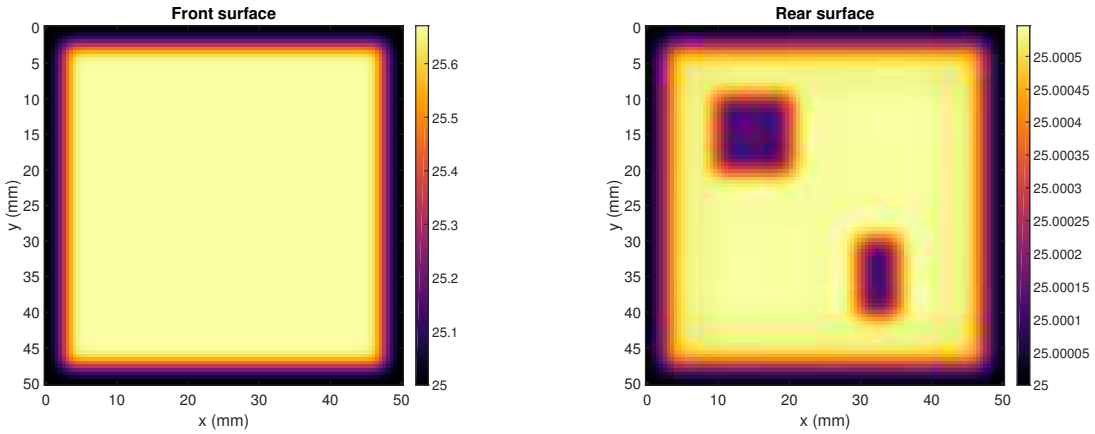

FIGURE 7. Simulated surface temperature field at time 0.0408 second for the multi-flaw configuration. *Left:* Top surface. *Right:* Bottom surface.

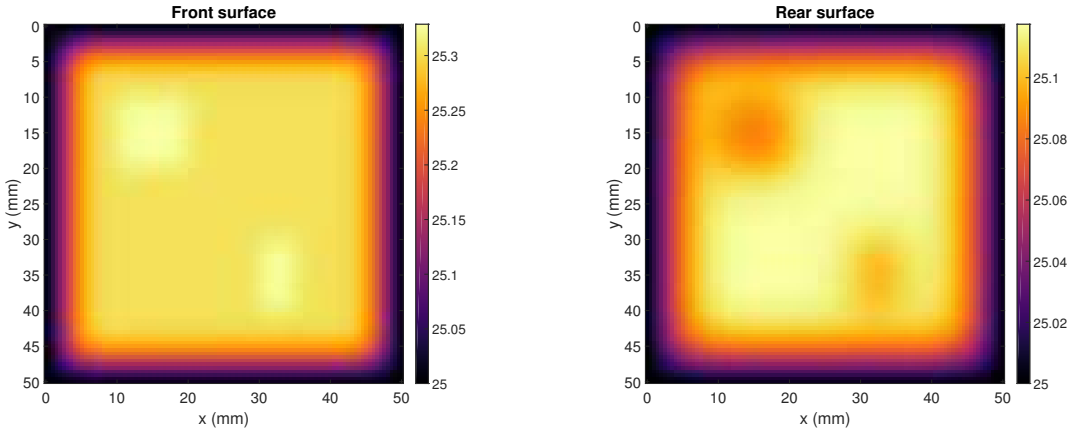

FIGURE 8. Simulated surface temperature field at time 0.2143 second for the multi-flaw configuration. *Left:* Top surface. *Right:* Bottom surface.

where $Q_b(t) = Q_0\delta(t-\tau)$, [W/m^2]. The defect is described as a thin layer of resistance $R_s = d_s/k_s$, where d_s is its thickness and k_s its thermal conductivity, modelled as a surface condition

$$-\mathbf{n}_d \cdot \mathbf{q}_d = -\frac{T_u - T_d}{R_s} \tag{27}$$

$$-\mathbf{n}_u \cdot \mathbf{q}_u = -\frac{T_d - T_u}{R_s} \tag{28}$$

where the subscript u stands for the upper layer and the subscript d stands for the down layer. The boundary conditions in x and y directions have been taken the same as in the TREE model. Due to the fact that the FEM method requires the definition of a closed box as solution domain, Dirichlet boundary conditions have been imposed in the z direction, at a sufficient distance from the domain of interest in order not to perturb the solution.

In Fig. 9, the TREE solution for the temperature time dependence at a distance of 0.5 mm from the centre of the front (on the left) and the rear (on the right) surface of the single-defect specimen is compared against the respective FEM results. Fig. 10 shows the same comparison for the second specimen. A very well agreement of both results is observed.

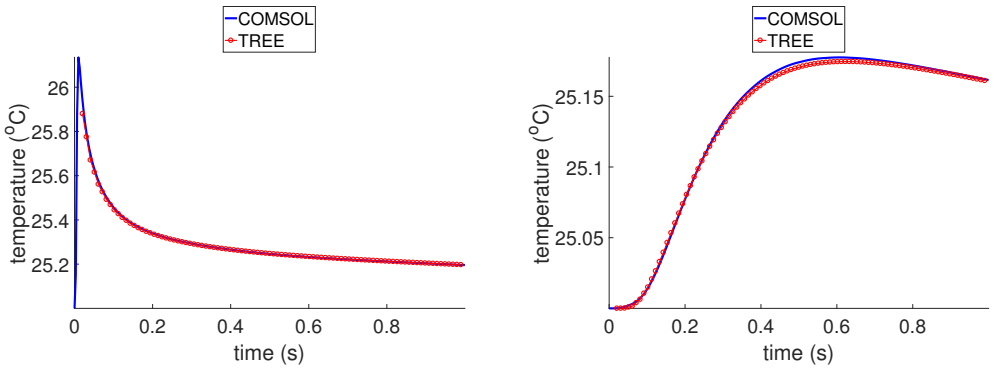

FIGURE 9. Simulated thermograms for the single-flaw model using COMSOL Multiphysics® and the TREE method obtained at the centre of the $xy-$plane and at a distance of $0.5mm$ from the surface of the plate. *Left:* Front face detection, *Right:* Rear face detection

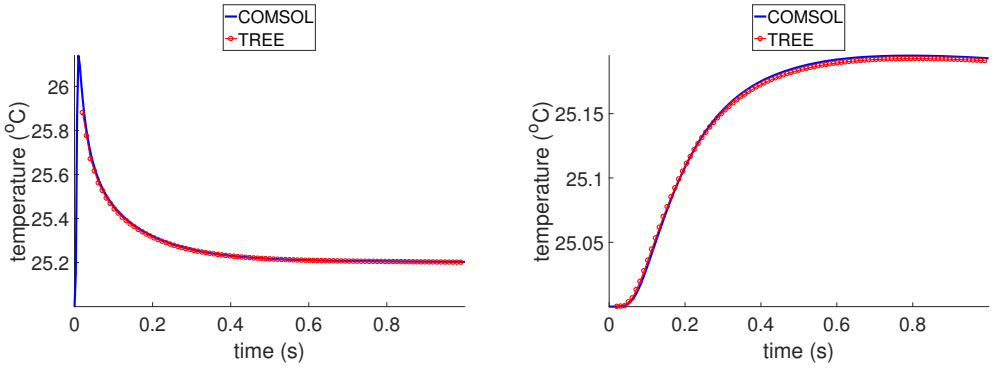

FIGURE 10. Simulated thermograms for the multi-flaw model using COMSOL Multiphysics® and the TREE method obtained at the centre of the $xy-$plane and at a distance of $0.5mm$ from the surface of the plate. *Left:* Front face detection, *Right:* Rear face detection

CONCLUSIONS

The proposed semi-analytical model can treat a wide range of problems in the field of TNDT involving canonical geometries, like stratified planar media. The model has been validated using a commercial FEM software, and the results are in good agreement.

Work is under way in order to include different thermal sources, such as an induction coil [10] in order to simulate a broad range of thermal inspection applications. In a further step, the herein presented semi-analytical model will be integrated in an inversion algorithm in order to provide estimations about the size and the thickness of the defect.

For the simulation of more general defect geometries, as for example pitting, stress corrosion cracking, etc., one must resort to the more general strategy involving an integral equation formalism like in [8, 9]. The development of a such solver lies in the broader perspectives of the current work.

REFERENCES

[1] X. P. V. Maldague and P. O. Moore, *Nondestructive Testing Handbook: Infrared and Thermal Testing*, Vol. 3 (The American Society for Nondestructive Testing, 2001).

[2] D. Maillet, S. André, J. C. Batsale, A. Degiovanni, and C. Moyne, *Thermal quadrupoles: soving the heat equation through integral transforms*, 1st ed. (John Willey & Sons, Inc., 2000).

[3] T. Theodoulidis and J. R. Bowler, IEEE Trans. Magn. **46**, 1034–1042April (2010).
[4] A. Skarlatos and T. Theodoulidis, Proc. R. Soc. London, Ser. A **470**June (2014), 10.1098/rspa.2014.0269.
[5] A. Skarlatos and T. Theodoulidis, IEEE Trans. Magn. **51**, p. 6201507September (2015).
[6] P. Vafeas, A. Skarlatos, T. Theodoulidis, and D. Lesselier, Math. Method. Appl. Sci. (in press).
[7] J. R. Bowler, T. Theodoulidis, and N. Poulakis, IEEE Trans. Magn. **48**, 4735–4746December (2012).
[8] R. Miorelli, C. Reboud, T. Theodoulidis, N. Poulakis, and D. Lesselier, IEEE Trans. Magn. **49**, 2886–2892June (2013).
[9] K. Pipis, A. Skarlatos, T. Theodoros, and D. Lesselier, IEEE Trans. Magn. **52**, p. 6200608April (2016).
[10] A. Ratsakou, C. Reboud, A. Skarlatos, and D. Lesselier, "Fast models dedicated to simulation of eddy current thermography," in *Electromagnetic Nondestructive Evaluation (XXI)*, Studies in Applied Electromagnetics and Mechanics, Vol. 43, edited by D. Lesselier and C. Reboud (IOS Press, Nieuwe Hemweg 6B, 1013 BG Amsterdam, Netherlands, 2018), pp. 175–182.
[11] T. Weiland, Int. J. Numer. Modell. **9**, 295–319 (1996).
[12] R. Marklein, Review of radio science **202**, 201–244 (1999).
[13] Comsol multiphysics, 2010.
[14] H. S. Carslaw and J. C. Jaeger, *Conduction of Heat in Solids*, 2nd ed. (Oxford University Press, 1986).
[15] H. Stehfest, ACM **13**, p. 4749 (1970).
[16] H. Stehfest, ACM **13**, p. 624 (1970).
[17] D. P. Gaver, Oper. Res. **14**, p. 444459 (1966).
[18] J. Roche and D. Balageas, "Common tools for quantitative pulse and step-heating thermography-part ii: experimental validation," in *The 12th International Conference on Quantitative InfraRed Thermography* (2014).

Model based characterisation of delamination by means of thermographic inspection

Almpion Ratsakou[1], Christophe Reboud[1], Anastassios Skarlatos[1] and Dominique Lesselier[2]

[1] CEA, LIST, Centre de Saclay, Gif-sur-Yvette F-91191, France
[2] Laboratoire des Signaux et Systèmes (UMR8506, CNRS-CentraleSupélec-Univ. Paris Sud), Université Paris-Saclay, 91192 Gif-sur-Yvette cedex, France

E-mail: almpion.ratsakou@cea.fr

Abstract. The objective of the work presented in this paper is to propose a fast and accurate approach for the characterisation of the delamination in single-layer metallic planar pieces using infrared thermography. This approach is based on a combination of pre-processing techniques and inversion. The inversion has been done in a reduced parameter space since the pre-processing phase gives us information about the location and the shape of the flaws in the transverse plane. The estimation of the flaws' parameters has been carried out by an iterative data fitting method involving a fast semi-analytical three-dimensional model. The robustness of the proposed approach is numerically assessed in presence of synthetic noisy data sets in different configurations.

1. Introduction

Non-destructive evaluation (NDE) techniques can be evaluated in terms of their capability to answer to two main questions: (i) detection and (ii) identification or characterisation of defects. The first question requires a qualitative answer of a binary nature. The second one refers to quantitative parameters, that is, once a defect is detected it has to be identified in terms of its parameters as size, location, nature, independently of the technique employed. This work particularly emphasizes the identification problem in thermal non-destructive testing (TNDT).

Active thermography [1] uses a thermal source in order to deposit heat in the target material creating a transient heat flow and, when finding defects, thermal contrast. The most common form of active thermography for material evaluation consists in using sources as flash lamps or lasers where a pulse of light instantaneously heats a surface and the resulting temperature is observed with a thermal camera. This technique is also known as pulsed thermography and has been extensively used as inspection technology for composite and layered structures. The detection can be on the same side as the heat source or on the opposite side, depending on the type of access to the sample. However, analysis and inversion of thermographic data tends to be challenging since the underlying heat conduction phenomenon is a diffusion process. As heat diffuses in time and space, temperature differences blur, the heat source becomes harder and harder to resolve and the contrast created by the flaws is lower.

Typical TNDT procedure results in a sequence of infrared (IR) images, obtained via an IR camera, that reflects the evolution of temperature in time. Mathematically, such a sequence can be regarded as a three-dimensional table of temperature values, with the dimensions being

space and time, $\mathbf{T}_{x,y,t}$. This recorded thermal response usually is degraded because of several factors. Uneven heating, variations of emissivity on the observed surface, optical distortions and noises of multiple nature significantly decrease the quality of the obtained thermal images. These factors limit the potential sensitivity of any method. Usually, the recorded signals are a subject of some signal processing like subtraction of the camera response when the piece under test is removed.

Several data processing techniques for reducing the amount of noise in thermal images and local storage requirements while improving the visibility of discontinuities have been proposed in the literature. These algorithms are either one-dimensional, being applied to pixel-based temperature evolutions in time, or two-dimensional, being applied to single images. Single IR images are normally filtered or segmented to reduce random noise or to analyse geometrical features of the areas of interest.

Much more information about defect parameters can be obtained by analysing the evolution of temperature in time. Therefore, most TNDT processing algorithms use pixel-based functions, which rely on one-dimensional diffusion models [2]. These models serve very well their purpose when one is trying to identify one defect at the time or defects located at a reasonable distance since the presence of one does not affect the temperature profile of the other. When the defects are located close to each other the usage of pixel-based functions, *i.e.* one dimensional models, fails to characterise those defects with an acceptable accuracy.

The usage of one dimensional models is not restricted only by the relative location of the defects but also by the depth of the defects. In situations where the defects are deeply buried in the material, or the material is too thick, the need of using a three-dimensional approach which will take into account the interaction between the defects and the occurred diffusion is of a significant importance. Yet, one cannot define a strict rule which will imply the limits of the one-dimensional model with respect to the mentioned parameters. The application of two or three-dimensional models in iterative inversion schemes is limited because of their excessive computational time since most of them are based on a numerical approaches [3].

In this work we propose a combination of pre-processing techniques and inversion to achieve an accurate characterisation of delamination-type flaws in metallic plates. We regularize the inverse problem by pre-processing the data, which brings information about the location and the shape of the flaws in the transverse plane. Thus, we are dealing with an easier problem since the size of the parameters is significantly reduced. Here we present the inversion problem by assuming that the pre-processing has been carried out, which will be presented in a future contribution. We use a fast, three-dimensional, semi-analytical direct model which is able to produce reliable data in cases of planar double-layered materials with embedded, rectangularly shaped in the transverse plane defects [4]. This semi-analytical direct model is based on an approach referred in the literature as the truncated region eigenfunction expansion (TREE) which has been successfully applied also in electromagnetics for the solution of magnetostatic and low-frequency (eddy-current) problems [5].

2. Methodology

A valuable answer to the characterisation problem can be given if one has at its disposal three essential elements:(i) a characterisation of the defect parameters in terms of the active parameters in the physical process used by the NDE technique, (ii) a direct model giving the expression of the measured quantity as a function of the active parameters of the defect and (iii) an inversion (or parameter estimation) technique that gives these parameters as a function of the measured physical quantities. In our case, the defect parameters are the physical parameters of the defect such as its location, its size and its thermal properties. The measured quantity is the temperature recorded as a time series at the surfaces of the sample. The theoretical value of the surface temperature $\mathbf{T}_{\text{surf}}$ will be provided by the aforementioned semi-analytical model

where the thermal characteristics of the sample are known.

In literature one can find different parameter estimation techniques depending on the nature of the parameters one is looking for. The depth profile reconstruction, the inverse problem, consists of set of attempts for fitting $\mathbf{T}_{\text{surf}}$ by trying all reasonable profiles. In the spatial domain the inverse scattering technique has been used to reconstruct both thermal conductivity and heat capacity depth profiles [6] and the conjugate gradient technique has been used to optimise the fit. In the time domain the effusivity depth profile has been reconstructed [7, 8] and the neural network approach has been used to find the best fit [9].

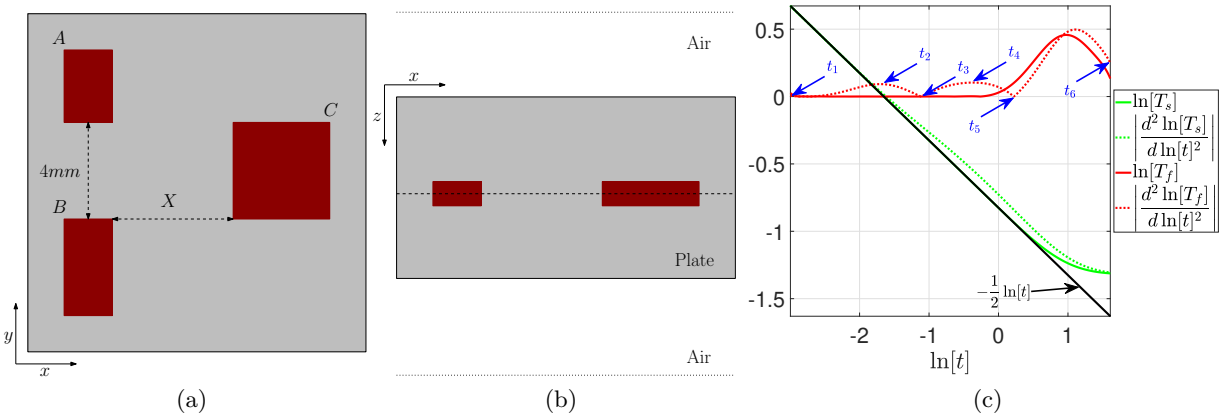

(a) (b) (c)

Figure 1: Sketch of the configuration in the xz–plane, (a) and in the xz–plane, (b). Thermograms in logarithmic scale for a sound area, T_s a flawed area, T_f and the absolute value of their second logarithmic derivatives.

In TNDT a successful characterisation of a subsurface defect consists of the knowledge of its location, its dimensions and its thermal properties. Our approach separates the characterisation of the defect in two stages: in the first stage, the localisation of possible defects and the reconstruction of their shapes in the xy–plane, see Fig. 1a, during the second stage, the estimation of their thickness and depth, see Fig. 1b, performed by using an iterative scheme.

2.1. Pre-processing

The temperature field inside anisotropic materials can be expressed mathematically by Eq. (1), where ρ, c represent the material density and heat capacity, respectively, κ_x, κ_y and κ_z represent the thermal conductivities in three principal directions. If the heating of the plate is instantaneous and on one side of the plate only, we can assume that the solution of temperature in flawless regions can be described by the one-dimensional heat equation $\frac{\partial T}{\partial t} = \alpha \frac{\partial^2 T}{\partial z^2}$, where $\alpha = \frac{\kappa}{\rho c}$ is the thermal diffusivity of the material. For an ideal pulse, heat flux uniformly applied to the surface of a semi-infinite solid, the temperature of the material at distance z from its surface is given by Eq. (2) where $\epsilon = \sqrt{\kappa \rho c}$ is the heat effusivity and Q is the energy supplied to the surface. The temperature at the surface of the sample it described by Eq. (3). From Eq. (3) is clear that the presence of any defect will be expressed as the deviation of the temperature decay curve from its expected values.

$$\rho c \frac{\partial T}{\partial t} = \kappa_x \frac{\partial^2 T}{\partial x^2} + \kappa_y \frac{\partial^2 T}{\partial y^2} + \kappa_z \frac{\partial^2 T}{\partial z^2} \tag{1}$$

$$T(z,t) = \frac{Q}{\epsilon\sqrt{\pi t}} e^{\frac{z^2}{4\alpha t}} \tag{2}$$

$$T(t) = \frac{Q}{\epsilon\sqrt{\pi t}} \tag{3}$$

To get rid of experimental noise, pre–processing like thermographic signal reconstruction (TSR) leads to high spatial and temporal detection resolution [10]. The assumption of TSR is identical with the assumption of Eq. (3), which can be rewritten in the logarithmic scale as $\ln\left(T_{\text{surf}}(t)\right) = \ln\left(\frac{Q}{\epsilon}\right) - \frac{1}{2}\ln\left(\pi t\right)$ and expanded into a polynomial series:

$$\ln\left(T_{\text{surf}}(t)\right) = a_0 + a_1\ln(t) + a_2\left[\ln(t)\right]^2 + \cdots + a_n\left[\ln(t)\right]^n . \tag{4}$$

where the logarithmic evolution of temperature at each pixel has been approximated by a n-degree polynomial function. This approximation compresses a thermographic sequence into $n+1$ frames of polynomial coefficients, removes high-frequency temporal noise and enhances the defect visibility. Reconstruction of the signals in the logarithmic scale and the computation of second time derivative using the polynomial approximation derives time frames which are smoother and suitable for defect detection. Such detection can be carried out by different image processing algorithms, such as the Canny edge detection algorithm, to define the location, shape and size in the xy–plane of the defects. The application of these algorithms is out of the scope of the present communication and it will be addressed in a future work.

The choice of the polynomial degree is a trade off between accuracy of the approximation, noise management and computational time. Here the choice has been made by studying the behaviour of the second time derivative of the signals in the logarithmic space and re-sampling in time. Initially we choose the time instances where the absolute value of the second time derivative is zero and those where its value reaches local maxima between the zeros, see Fig. 1c. The first and the last time instances are also added. For t_N chosen time instances the polynomial degree will be set to be $n = t_N - 1$. In our case, as illustrated by Fig. 1c the absolute value of the second logarithmic derivative is zero at the beginning of time and in two more instances. By adding the instances where local maxima occur and the last time instance one has six time instances. Thus, the polynomial degree is set to be $n = 5$. For the configuration depicted in Fig. 1, and using noisy signals, $SNR = 20$, obtained in reflection we present the reconstructed images, Fig. 2, at the first four chosen time instances.

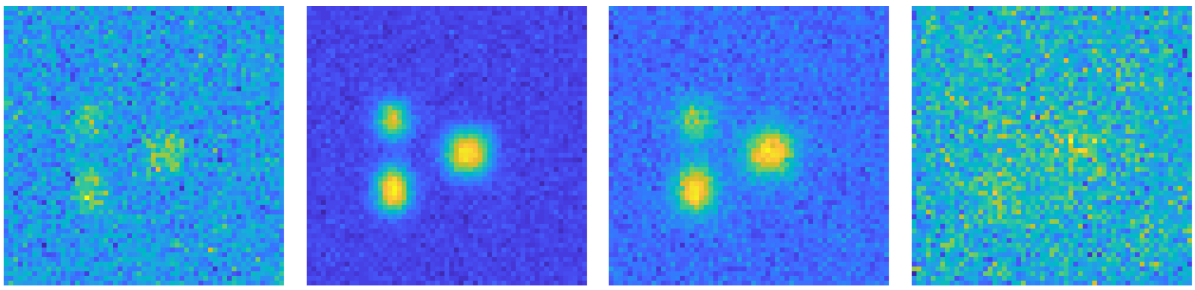

Figure 2: Reconstructed temperature field in the logarithmic scale for the first four chosen time instances, t_i, $i = 1, 2, 3, 4$.

2.2. Defect characterisation

In an inversion process, one usually minimizes a discrepancy between some experimental data, say u_d, and some model data, say u. The discrepancy function, also called cost or objective function, is often expressed as a norm of the difference between u_d and u. Most often, one uses the $L_2(\cdot)$ norm but since we are working with discrete data, the squared Euclidean norm is to

be used, $\mathcal{J} = f\left(||u - u_d||_2^2\right)$. The cost function is explicitly given in terms of u and minimized with respect to the parameters ψ, characterizing the flaws.

For the minimization problem the Levenberg–Marquardt method has been used [11]. This is an iterative method originally devised for solving non-linear least-square problems of parameter estimation but it has also been successfully applied to the solution of linear problems that are too ill-conditioned to permit the application of linear algorithms. The method decreases the ill-condition feature by using a "damping" parameter, $\ell \leq 0$, which may be adjusted at each iteration. Note that $\ell \to 0$ yields the Gauss-Newton algorithm while larger ℓ gives an approximation of the steepest descent gradient algorithm.

The forward model we use here models defects of delamination type as boundary conditions in a fictional interface inside the metallic plate. Thus, we are bounded to consider only flaws that are located at the same depth. The parameters to be estimated here are the depth at which the defects are located and their thickness. Thus, for the m detected flaws, the number of the unknown parameters will be $m + 1$, $\psi = (\psi_1, \psi_2, \ldots, \psi_{m+1})^{\mathrm{T}}$.

After applying TSR to the synthetic noisy data $\mathbf{T}_{\mathrm{surf}}$, we end up with a three-dimensional matrix, denoted $\mathbf{T}_{p_x,p_y,n+1}$, containing $n + 1$ frames of $p_x \times p_y$ elements with the coefficients of the n-degree polynomials as expressed in Eq. (4). For each pixel we reconstruct the temperature signals in the logarithmic scale by evaluating the polynomials at the, previously chosen, time instances t_i, $i = 1, 2, \ldots, n + 1$. The data to be fitted, denoted as u_d, is now the vectorised temperature in the logarithmic scale.

3. Experiment and result analysis

For the purpose of this research, the three-dimensional model [4] has been used to produce synthetic data, temperature signals, for the general configuration depicted in Fig. 1 . A grade 4340 steel plate with thermal conductivity $k = 44.5$ W/mK, heat capacity $C_p = 475$ J/kgK, density $\rho = 7850$ kg/m^3 and of thickness $d = 3$ mm is used. The steel plate has three well-defined air-filled defects, named A, B and C, to simulate delaminations of different thickness, $d_A = 3 \times 10^{-6}$ m, $d_B = 2 \times 10^{-6}$ m, $d_C = 1 \times 10^{-6}$ m and of different size $(2 \times 3$ mm), $(2 \times 4$ mm), $(4 \times 4$ mm), respectively. As an excitation term, a flash lamp depositing a heating power density of Q $= 10^4$ W/m^2 on the surface of the plate has been modelled as a Dirac's delta function in time, whereas its spatial distribution is considered as uniform.

To test the robustness of the inversion scheme versus the noise, the configuration depicted in Fig. 1 has been tested for different noise levels using recorded signals in reflection, in transmission and in both situations. The thickness of the top and bottom layer, for this configuration, is $d_1 = 1.5$ mm and $d_2 = 1.5$ mm, respectively. The distance of the defects A and B from the defect C, which has been indicated as X in Fig. 1a, for this reference case $X = 5$ mm. The parameters to be estimated are the thickness of the defects and the depth in which they are located, d_A, d_B, d_C and Z respectively.

The relative error of the estimation of the parameters is shown in Fig. 3 for each parameter as a function of SNR. As one can see, the estimation is highly depending on SNR but also on the used signals. That is, using the signals obtained in transmission, a better estimation can be achieved than using the signals in reflection. Yet the usage of both signals does not ensure a better estimation as one can see in Fig. 3a and in Fig. 3b where for SNR equal to 40 or 30 the estimation is not given with a smaller relative error as in the case of using only the signals recorded in transmission.

From Fig. 3 one can understand the nature of the estimated parameters and how their estimation can be affected by the signals used. From these graphs it is clear that the best estimation of the defects depth can be achieved by using both recorded signals, *i.e.* in reflection and transmission, and the worst one by using only the signals in transmission, see Fig. 3d. The

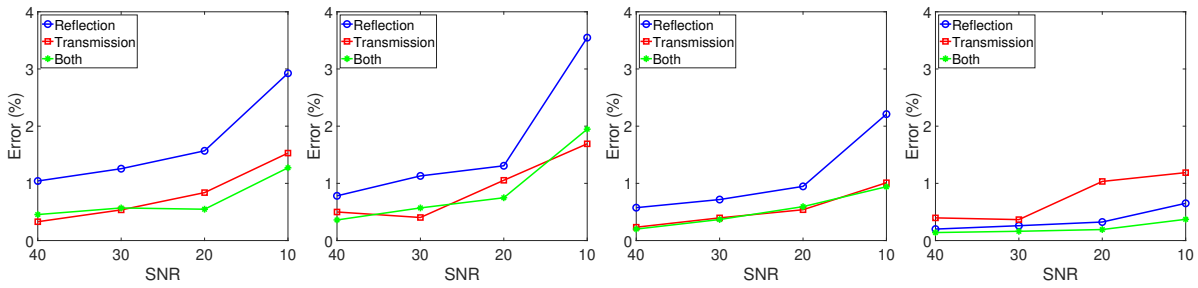

(a) d_A (b) d_B (c) d_C (d) Z

Figure 3: Relative error for the estimation of four parameters as a function of SNR.

latter is not true for the estimation of the defects' thickness as it is clear from Fig. 3(a),(b),(c) where the estimation is better using the signals in transmission than in reflection.

By using the configuration depicted in Fig. 1a as a reference, we want to test the performance of the inversion scheme in difficult situations. Such a situation can be when the defects are located close to the top or bottom surface of the plate. The depth of the defect, *i.e.* the distance of the defects from the upper surface of the plate, has been changed to 0.75 mm and 2.25 mm while the noise level has been kept constant, $SNR = 20$.

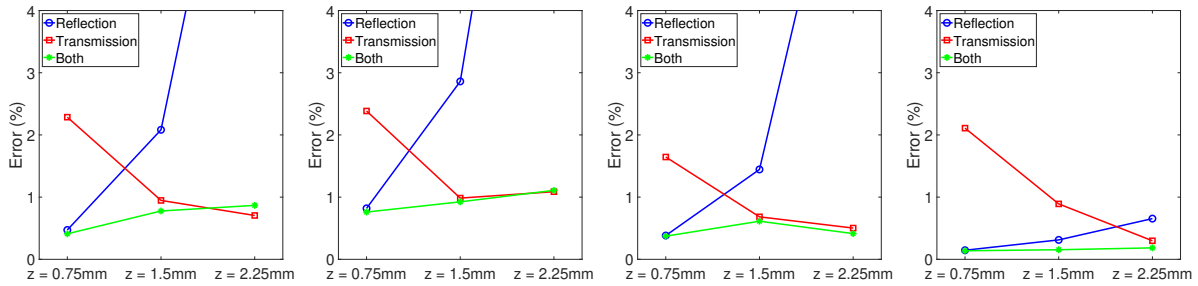

(a) d_A (b) d_B (c) d_C (d) Z

Figure 4: Relative error for the estimation of four parameters as a function of defects' depth.

The estimation of the parameters d_A, d_B and d_C is strongly affected by the depth of the defects as one can see in Fig. 4. For the configuration where the defect is deeply buried in the plate, $z = 2.25$ mm, the estimation of the thickness is very poor using the signals in reflection, relative error higher than 10%, but very accurate when using the signals in transmission. On the other hand, when the defects are close to the upper surface, the estimation accuracy is not significantly affected. As for the estimation of the defects' depth, for the buried defects the estimation accuracy is better using signals in transmission whereas in the case of the defects being close to the upper surface of the plate the estimation is better using signals in reflection. These results agree with the physics of the problem.

An interesting configuration where the advantages of using a three-dimensional forward model can be fully exploited is that of defects located close to each other. Keeping as reference the configuration depicted in Fig. 1a, we set up two new configurations by setting the distance of the defect named C from the other two to 2 mm and 0 mm respectively. The noise level has been kept constant, $SNR = 20$. In this kind of configurations, where the interaction between the defects is strong, the one-dimensional approaches fail to characterize accurately the defects. The advantage of using a three-dimensional model can be exemplified by Fig. 5 where one cannot find a strong link of the estimation accuracy and the defects' relative location in the xy-plane.

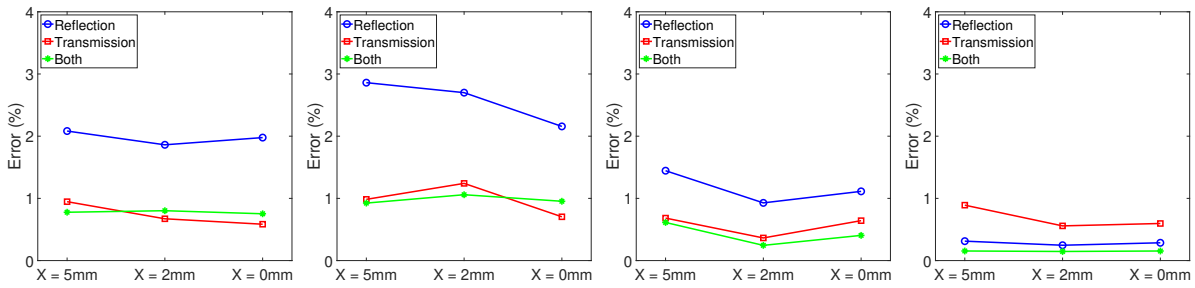

(a) d_A (b) d_B (c) d_C (d) Z

Figure 5: Relative error for the estimation of four parameters as a function of the relative distance X between to defects A, B and C.

4. Conclusions and perspectives

This contribution presented a model-based inversion strategy for thermographic characterisation of delamination in planar pieces. We choose to use here the Levenberg–Marquardt method where, as an iterative method, its performance is strongly linked to the forward model. In this work we use a three-dimensional semi-analytical model based in the TREE approach which is fast and accurate. Results of the inversion scheme, using synthetic noisy data, have been presented in the work for several cases.

In the future we intend to extend this work by considering more complex cases. Thus, the used froward model has to be enhanced. Flaws with more complex shapes in the transverse plane have to be introduced in stratified planar geometries for modelling delamination in composites. Surface defects, crack-type, will be introduced to the model using the Green function. Moreover, the application of signal processing tools as the Canny algorithm will be addressed in order to compute the transverse location and the shape of the flaws.

References

[1] Maldague X. Nondestructive evaluation of materials by infrared thermography. Springer Science & Business Media; 2012.
[2] Wysocka-Fotek O, Maj M, Oliferuk W. Use of pulsed IR thermography for determination of size and depth of subsurface defect taking into account the shape of its cross-section area. Archives of Metallurgy and Materials. 2015;60(2):615–620.
[3] Ratsakou A, Reboud C, Skarlatos A, Lesselier D. Fast models dedicated to simulation of eddy current thetmography. Studies in Applied Electromagnetics and Mechanics. 2018;43:175–182.
[4] Ratsakou A, Reboud C, Skarlatos A, Lesselier D. Fast simulation approach dedicated to infrared thermographic inspection of delaminated planar pieces. In: AIP Conference Proceedings. vol. 2102. AIP Publishing; 2019. p. 120004.
[5] Skarlatos A, Theodoulidis T. Calculation of the eddy-current flow around a cylindrical through-hole in a finite-thickness plate. IEEE Transactions on Magnetics. 2015;51(9):1–7.
[6] Vidberg H, Jaarinen J, Riska D. Inverse determination of the thermal-conductivity profile in steel from the thermal-wave surface data. Canadian Journal of Physics. 1986;64(9):1178–1183.
[7] Balageas D, Krapez JC, Cielo P. Pulsed photothermal modeling of layered materials. Journal of Applied Physics. 1986;59(2):348–357.
[8] Krapez JC. Thermal effusivity profile characterization from pulse photothermal data. Journal of Applied Physics. 2000;87(9):4514.
[9] Glorieux C, Li Voti R, Thoen J, Bertolotti M, Sibilia C. Depth profiling of thermally inhomogeneous materials by neural network recognition of photothermal time domain data. Journal of Applied Physics. 1999;85(10):7059–7063.
[10] Shepard SM, Beemer MF. Advances in thermographic signal reconstruction. In: Thermosense: Thermal Infrared Applications XXXVII. vol. 9485. International Society for Optics and Photonics; 2015. p. 94850R.
[11] Moré J. The Levenberg-Marquardt algorithm: implementation and theory. In: Numerical analysis. Springer; 1978. p. 105–116.

Bibliography

[1] G. Workman and P. Moore, *Nondestructive Testing Overview*, vol. 10 of *Nondestructive Testing Handbook*. American Society for Nondestructive Testing, 2012.

[2] X. Maldague and P. Moore, *Infrared and Thermal Testing*, vol. 3 of *Nondestructive Testing Handbook*. American Society for Nondestructive Testing, 2001.

[3] W. Herschel, "XIII. Investigation of the powers of the prismatic colours to heat and illuminate objects; with remarks, that prove the different refrangibility of radiant heat. To which is added, an inquiry into the method of viewing the sun advantageously, with telescopes of large apertures and high magnifying powers," *Philosophical Transactions of the Royal Society of London*, vol. 90, pp. 255–283, 1800.

[4] W. Herschel, "XV. Experiments on the solar, and on the terrestrial rays that occasion heat; with a comparative view of the laws to which light and heat, or rather the rays which occasion them, are subject, in order to determine whether they are the same, or different," *Philosophical Transactions of the Royal Society of London*, vol. 90, pp. 293–326, 1800.

[5] W. Beller, "Navy sees promise in infrared thermography for solid case checking," *Missiles and Rochets*, vol. 16, no. 22, pp. 1234–1241, 1965.

[6] D. R. Green, "Principles and applications of emittance-independent infrared nondestructive testing," *Applied Optics*, vol. 7, no. 9, pp. 1779–1789, 1968.

[7] J. B. J. Fourier, *Théorie Analytique de la Chaleur*. F. Didot, 1822.

[8] R. D. Parker, "Thermic balance or radiometer.," 1914. US Patent 1,099,199.

[9] G. A. Barker, "Apparatus for detecting forest fires," 1934. US Patent 1,959,702.

[10] P. Vernotte, "La mesure du coefficient d'arrachement thermique des isolants par la méthode du touchau," *Chaleur et Industrie*, vol. 208, pp. 331–338, 1937.

[11] E. Hendler, R. Crosbie, and J. Hardy, "Measurement of heating of the skin during exposure to infrared radiation," *Journal of Applied Physiology*, vol. 12, no. 2, pp. 177–185, 1958.

[12] R. Rudkin, R. Jenkins, and W. Parker, "Thermal diffusivity measurements on metals at high temperatures," *Review of Scientific Instruments*, vol. 33, no. 1, pp. 21–24, 1962.

[13] J. C. Jaeger and H. S. Carslaw, *Conduction of Heat in Solids*. Clarendon Press, 1959.

[14] A. A. Luikov and J. Hartnett, *Analytical Heat Conduction Theory*. Academic Press Inc., 1968.

[15] G. Carlomagno and P. G. Berardi, "Unsteady thermotopography in nondestructive testing," in *Proc. 3rd Biannual Exchange, St. Louis/USA*, vol. 24, p. 26, 1976.

[16] V. Vavilov and R. Taylor, "Theoretical and practical aspects of the thermal nondestructive testing of bonded structures," *Academic Press, Research Techniques in Nondestructive Testing*, vol. 5, pp. 239–279, 1982.

[17] D. L. Balageas, J. C. Krapez, and P. Cielo, "Pulsed photothermal modeling of layered materials," *Journal of Applied Physics*, vol. 59, no. 2, pp. 348–357, 1986.

[18] A. Mandelis, F. Funak, and M. Munidasa, "Generalized methodology for thermal diffusivity depth profile reconstruction in semi-infinite and finitely thick inhomogeneous solids," *Journal of Applied Physics*, vol. 80, no. 10, pp. 5570–5578, 1996.

[19] J. C. Krapez, X. Maldague, and P. Cielo, "Thermographic nondestructive evaluation: Data inversion procedures - Part II: 2-D analysis and experimental results," *Research in Nondestructive Evaluation*, vol. 3, no. 2, pp. 101–124, 1991.

[20] J. Krapez and D. Balageas, "Early detection of thermal contrast in pulsed stimulated infrared thermography," in *The 2cd International Conference on Quantitative InfraRed Thermography (QIRT 1994)*, vol. 94, pp. 1994–039, 1994.

[21] X. Maldague and S. Marinetti, "Pulse phase infrared thermography," *Journal of Applied Physics*, vol. 79, no. 5, pp. 2694–2698, 1996.

[22] X. Maldague, *Theory and Practice of Infrared Technology for Nondestructive Testing*. Wiley, 2001.

[23] A. B. Harman and C. H. Wang, "Improved design methods for scarf repairs to highly strained composite aircraft structure," *Composite Structures*, vol. 75, no. 1-4, pp. 132–144, 2006.

[24] K. B. Katnam, A. J. Comer, D. Roy, L. F. M. da Silva, and T. M. Young, "Composite repair in wind turbine blades: an overview," *The Journal of Adhesion*, vol. 91, no. 1-2, pp. 113–139, 2015.

[25] S. S. Pendhari, T. Kant, and Y. M. Desai, "Application of polymer composites in civil construction: A general review," *Composite Structures*, vol. 84, no. 2, pp. 114–124, 2008.

[26] A. M. Brandt, "Fibre reinforced cement-based (FRC) composites after over 40 years of development in building and civil engineering," *Composite Structures*, vol. 86, no. 1-3, pp. 3–9, 2008.

[27] S. Bagavathiappan, B. Lahiri, T. Saravanan, J. Philip, and T. Jayakumar, "Infrared thermography for condition monitoring–a review," *Infrared Physics & Technology*, vol. 60, pp. 35–55, 2013.

[28] C. Balaras and A. Argiriou, "Infrared thermography for building diagnostics," *Energy and Buildings*, vol. 34, no. 2, pp. 171–183, 2002.

[29] D. Hernandez-Contreras, H. Peregrina-Barreto, J. Rangel-Magdaleno, and J. Gonzalez-Bernal, "Narrative review: Diabetic foot and infrared thermography," *Infrared Physics & Technology*, vol. 78, pp. 105–117, 2016.

[30] W. Harizi, S. Chaki, G. Bourse, and M. Ourak, "Mechanical damage assessment of Glass Fiber-Reinforced Polymer composites using passive infrared thermography," *Composites Part B: Engineering*, vol. 59, pp. 74–79, 2014.

[31] X. Maldague, "Introduction to ndt by active infrared thermography," *Materials Evaluation*, vol. 60, no. 9, pp. 1060–1073, 2002.

[32] V. Feuillet, L. Ibos, M. Fois, J. Dumoulin, and Y. Candau, "Defect detection and characterization in composite materials using square pulse thermography coupled with singular value decomposition analysis and thermal quadrupole modeling," *NDT & E International*, vol. 51, pp. 58–67, 2012.

[33] A. A. Badghaish and D. C. Fleming, "Non-destructive inspection of composites using step heating thermography," *Journal of Composite Materials*, vol. 42, no. 13, pp. 1337–1357, 2008.

[34] N. Tabatabaei and A. Mandelis, "Thermal-wave radar: A novel subsurface imaging modality with extended depth-resolution dynamic range," *Review of Scientific Instruments*, vol. 80, no. 3, p. 034902, 2009.

[35] M. A. Omar and Y. Zhou, "A quantitative review of three flash thermography processing routines," *Infrared Physics and Technology*, vol. 51, no. 4, pp. 300–306, 2008.

[36] T. Li, D. P. Almond, and D. S. Rees, "Crack imaging by scanning pulsed laser spot thermography," *NDT & E International*, vol. 44, no. 2, pp. 216–225, 2011.

[37] S. Burrows, S. Dixon, S. Pickering, T. Li, and D. Almond, "Thermographic detection of surface breaking defects using a scanning laser source," *NDT & E International*, vol. 44, no. 7, pp. 589–596, 2011.

[38] X. Maldague, F. Galmiche, and A. Ziadi, "Advances in pulsed phase thermography," *Infrared Physics & Technology*, vol. 43, no. 3-5, pp. 175–181, 2002.

[39] B. Gao, L. Bai, W. L. Woo, G. Y. Tian, and Y. Cheng, "Automatic defect identification of eddy current pulsed thermography using single channel blind source separation," *IEEE Transactions on Instrumentation and Measurement*, vol. 63, no. 4, pp. 913–922, 2014.

[40] Y. He and R. Yang, "Eddy current volume heating thermography and phase analysis for imaging characterization of interface delamination in CFRP," *IEEE Transactions on Industrial Informatics*, vol. 11, no. 6, pp. 1287–12897, 2015.

[41] R. Yang and Y. He, "Eddy current pulsed phase thermography considering volumetric induction heating for delamination evaluation in carbon fiber reinforced polymers," *Applied Physics Letters*, vol. 106, no. 23, p. 234103, 2015.

[42] C. Xu, N. Zhou, J. Xie, X. Gong, G. Chen, and G. Song, "Investigation on eddy current pulsed thermography to detect hidden cracks on corroded metal surface," *NDT & E International*, vol. 84, pp. 27–35, 2016.

[43] N. J. Siakavellas, "The influence of the heating rate and thermal energy on crack detection by eddy current thermography," *Journal of Nondestructive Evaluation*, vol. 35, no. 2, 2016.

[44] Y. He, G. Y. Tian, M. Pan, D. Chen, and H. Zhang, "An investigation into eddy current pulsed thermography for detection of corrosion blister," *Corrosion Science*, vol. 78, pp. 1–6, 2014.

[45] P. Jäckel and U. Netzelmann, "The influence of external magnetic fields on crack contrast in magnetic steel detected by induction thermography," *Quantitative InfraRed Thermography Journal*, vol. 10, no. 2, pp. 237–247, 2013.

[46] B. Lahiri, S. Bagavathiappan, C. Soumya, V. Mahendran, V. Pillai, J. Philip, and T. Jayakumar, "Infrared thermography based defect detection in ferromagnetic specimens using a low frequency alternating magnetic field," *Infrared Physics & Technology*, vol. 64, pp. 125–133, 2014.

[47] A. Foudazi, A. Mirala, M. T. Ghasr, and K. M. Donnell, "Active microwave thermography for nondestructive evaluation of surface cracks in metal structures," *IEEE Transactions on Instrumentation and Measurement*, vol. 68, no. 2, pp. 576–585, 2019.

[48] U. Polimeno, D. P. Almond, B. Weekes, and E. W. J. Chen, "A compact thermosonic inspection system for the inspection of composites," *Composites Part B: Engineering*, vol. 59, pp. 67–73, 2014.

[49] C. Ibarra-Castanedo, M. Genest, S. Guibert, J.-M. Piau, X. P. V. Maldague, and A. Bendada, "Inspection of aerospace materials by pulsed thermography, lock-in thermography, and vibrothermography: a comparative study," in *Thermosense XXIX*, vol. 6541, p. 654116, 2007.

[50] P. Menner, C. Spiessberger, A. Gleiter, G. Busse, D. O. Thompson, and D. E. Chimenti, "Aerospace applications of lockin thermography with optical, ultrasonic and inductive excitation," in *AIP Conference Proceedings*, vol. 1211, pp. 525–532, American Institute of Physics, 2010.

[51] A. C. Tam and B. Sullivan, "Remote sensing applications of pulsed photothermal radiometry," *Applied Physics Letters*, vol. 43, no. 4, pp. 333–335, 1983.

[52] W. P. Leung and A. C. Tam, "Thermal diffusivity in thin films measured by noncontact single-ended pulsed-laser-induced thermal radiometry," *Optics Letters*, vol. 9, no. 3, p. 93, 1984.

[53] W. P. Leung and A. C. Tam, "Techniques of flash radiometry," *Journal of Applied Physics*, vol. 56, no. 1, pp. 153–161, 1984.

[54] N. P. Avdelidis, D. P. Almond, A. Dobbinson, and B. C. Hawtin, "Pulsed thermography : philosophy , qualitative quantitative analysis on aircraft materials & applications," *Proceedings of Vth International Workshop, Advances in Signal Processing for Non Destructive Evaluation of Materials*, p. 53, 2006.

[55] F. Mabrouki, M. Thomas, M. Genest, and A. Fahr, "Frictional heating model for efficient use of vibrothermography," *NDT & E International*, vol. 42, no. 5, pp. 345–352, 2009.

[56] R. I. Hickson, S. I. Barry, G. N. Mercer, and H. S. Sidhu, "Finite difference schemes for multilayer diffusion," *Mathematical and Computer Modelling*, vol. 54, no. 1-2, pp. 210–220, 2011.

[57] G. Andrés Restrepo and C. Humberto Loaiza, "New Method for Basic Detection and Characterization of Flaws in Composite Slabs through Finite Difference Thermal Contrast (FDTC)," *11th International Conference on Quantitative InfraRed Thermography*, 2012.

[58] J. G. Sun, "Pulsed thermal imaging measurement of thermal properties for thermal barrier coatings based on a multilayer heat transfer model," *Journal of Heat Transfer*, vol. 136, no. 8, 2014.

[59] R. Marklein, "The Finite Integration Technique as a general tool to compute acoustic, electromagnetic, elastodynamic and coupled wave fields," *Review of Radio Science*, 1999.

[60] M. N. Özışık, *Heat conduction*. John Wiley & Sons, 1993.

[61] K. D. Cole, J. V. Beck, A. Haji-Sheikh, and B. Litkouhi, *Heat Conduction Using Green's Functions*. CRC Press, 2010.

[62] A. Mandelis, *Diffusion-Wave Fields: Mathematical Methods and Green Functions*. Springer Science & Business Media, 2013.

[63] Y. Sun and I. S. Wichman, "On transient heat conduction in a one-dimensional composite slab," *International Journal of Heat and Mass Transfer*, vol. 47, no. 6-7, pp. 1555–1559, 2004.

[64] F. De Monte, "An analytic approach to the unsteady heat conduction processes in one-dimensional composite media," *International Journal of Heat and Mass Transfer*, vol. 45, no. 6, pp. 1333–1343, 2002.

[65] E. J. Carr and I. W. Turner, "A semi-analytical solution for multilayer diffusion in a composite medium consisting of a large number of layers," *Applied Mathematical Modelling*, vol. 40, no. 15-16, pp. 7034–7050, 2016.

[66] J. Padovan, "Generalized Sturm-Liouville Procedure for Composite Domain Anisotropic Transient Conduction Problems," *AIAA Journal*, vol. 12, no. 8, pp. 1158–1160, 1974.

[67] H. Salt, "Transient conduction in a two-dimensional composite slab—I. Theoretical development of temperature modes," *International Journal of Heat and Mass Transfer*, vol. 26, no. 11, pp. 1611–1616, 1983.

[68] H. Salt, "Transient conduction in a two-dimensional composite slab—II. Physical interpretation of temperature modes," *International Journal of Heat and Mass Transfer*, vol. 26, no. 11, pp. 1617–1623, 1983.

[69] M. Mikhailov and M. Özişik, "Transient conduction in a three-dimensional composite slab," *International Journal of Heat and Mass Transfer*, vol. 29, no. 2, pp. 340–342, 1986.

[70] B. V. Averin, D. I. Kolotilkin, and V. A. Kudinov, "Sturm-liouville problem for a differential equation of second order with discontinuous coefficients," *Journal of Engineering Physics and Thermophysics*, vol. 73, no. 4, pp. 735–740, 2000.

[71] L. Yan, A. Haji-Sheikh, and J. V. Beck, "Thermal Characteristics of Two-Layered Bodies With Embedded Thin-Film Heat Source," *Journal of Electronic Packaging*, vol. 115, no. 3, pp. 276–283, 1993.

[72] A. Haji-Sheikh and J. V. Beck, "Temperature solution in multi-dimensional multi-layer bodies," *International Journal of Heat and Mass Transfer*, vol. 45, no. 9, pp. 1865–1877, 2002.

[73] H. Levine, "Unsteady diffusion in a composite medium," *Quarterly Journal of Mechanics and Applied Mathematics*, vol. 52, no. 4, pp. 499–512, 1999.

[74] V. P. Kozlov and P. A. Mandrik, "Method of Summation-Integral Equations for Solving the Mixed Problem of Nonstationary Heat Conduction," *Journal of Engineering Physics and Thermophysics*, vol. 74, no. 2, pp. 477–486, 2001.

[75] V. P. Kozlov and P. A. Mandrik, "Solution of Mixed Contact Problems in the Theory of Nonstationary Heat Conduction by the Method of Summation-Integral Equations," *Journal of Engineering Physics and Thermophysics*, vol. 74, no. 3, pp. 632–637, 2001.

[76] G. Araya and G. Gutierrez, "Analytical solution for a transient, three-dimensional temperature distribution due to a moving laser beam," *International Journal of Heat and Mass Transfer*, vol. 49, no. 21-22, pp. 4124–4131, 2006.

[77] D. Maillet, S. André, J. Batesale, A. Degiovanni, and C. Moyne, *Thermal Quadrupoles: Solving the Heat Hquation Through Integral Transforms.* John Wiley & Sons Inc, 2000.

[78] S. M. Shepard, "Reconstruction and enhancement of active thermographic image sequences," *Optical Engineering*, vol. 42, no. 5, p. 1337, 2003.

[79] D. L. Balageas, J. M. Roche, F. H. Leroy, W. M. Liu, and A. M. Gorbach, "The thermographic signal reconstruction method: A powerful tool for the enhancement of transient thermographic images," *Biocybernetics and Biomedical Engineering*, vol. 35, no. 1, pp. 1–9, 2015.

[80] N. Rajic, "Principal component thermography for flaw contrast enhancement and flaw depth characterisation in composite structures," *Composite Structures*, vol. 58, no. 4, pp. 521–528, 2002.

[81] F. Wang, Y.-h. Wang, W. Peng, J.-q. Ji, J.-y. Liu, P. Xiao, and Y. Wang, "Independent component analysis enhanced pulse thermography for high silicon oxygen phenolic resin (HSOPR) sheet with subsurface defects," *Infrared Physics & Technology*, vol. 92, pp. 345–349, 2018.

[82] L. Cheng, B. Gao, G. Y. Tian, W. L. Woo, and G. Berthiau, "Impact Damage Detection and Identification Using Eddy Current Pulsed Thermography Through Integration of PCA and ICA," *IEEE Sensors Journal*, vol. 14, no. 5, pp. 1655–1663, 2014.

[83] R. Shrestha, Y. Chung, and W. Kim, "Wavelet transform applied to lock-in thermographic data for detection of inclusions in composite structures: Simulation and experimental studies," *Infrared Physics & Technology*, vol. 96, pp. 98–112, 2019.

[84] B. Gao, A. Yin, G. Tian, and W. Woo, "Thermography spatial-transient-stage mathematical tensor construction and material property variation track," *International Journal of Thermal Sciences*, vol. 85, pp. 112–122, 2014.

[85] T. Liang, W. Ren, G. Y. Tian, M. Elradi, and Y. Gao, "Low energy impact damage detection in CFRP using eddy current pulsed thermography," *Composite Structures*, vol. 143, pp. 352–361, 2016.

[86] Y. Laib dit Leksir, M. Mansour, and A. Moussaoui, "Localization of thermal anomalies in electrical equipment using Infrared Thermography and support vector machine," *Infrared Physics & Technology*, vol. 89, pp. 120–128, 2018.

[87] B. Gao, W. L. Woo, Y. He, and G. Y. Tian, "Unsupervised Sparse Pattern Diagnostic of Defects With Inductive Thermography Imaging System," *IEEE Transactions on Industrial Informatics*, vol. 12, pp. 371–383, feb 2016.

[88] U. Seidel, T. T. N. Lan, and H.-G. Walther, "Quantitative characterization of material inhomogeneities by thermal waves," *Optical Engineering*, vol. 36, pp. 376–390, 1997.

[89] T. T. N. Lan, U. Seidel, and H. G. Walther, "Theory of microstructural depth profiling by photothermal measurements," *Journal of Applied Physics*, vol. 77, no. 9, pp. 4739–4745, 1995.

[90] T. T. Lan, U. Seidel, H. G. Walther, G. Goch, and B. Schmitz, "Experimental results of photothermal microstructural depth profiling," *Journal of Applied Physics*, vol. 78, no. 6, pp. 4108–4111, 1995.

[91] C. Glorieux and J. Thoen, "Thermal depth profile reconstruction by neural network recognition of the photothermal frequency spectrum," *Journal of Applied Physics*, vol. 80, no. 11, pp. 6510–6515, 1996.

[92] J. Fivez and J. Thoen, "Thermal waves in materials with inhomogeneous thermal conductivity: An analytical approach," *Journal of Applied Physics*, vol. 79, no. 1996, pp. 2225–2228, 1998.

[93] J. F. Power, "Expectation minimum - a new principle of inverse theoretical characterization of expectation values," *Optical Engineering*, vol. 36, no. 2, pp. 487–503, 1997.

[94] J. Power, "A survey of current issues in inverse problem theory as applied to thermal wave imaging," in *AIP Conference Proceedings*, vol. 463, pp. 3–7, AIP, 1999.

[95] M. Munidasa, F. Funak, and A. Mandelis, "Application of a generalized methodology for quantitative thermal diffusivity depth profile reconstruction in manufactured inhomogeneous steel-based materials," *Journal of Applied Physics*, vol. 83, no. 7, pp. 3495–3498, 1998.

[96] R. Kolarov and T. Velinov, "Real-time depth profile reconstruction of the thermal conductivity of inhomogeneous solids," *Journal of Applied Physics*, vol. 83, no. 4, pp. 1878–1883, 1998.

[97] H. Vidberg, J. Jaarinen, and D. Riska, "Inverse determination of the thermal-conductivity profile in steel from the thermal-wave surface data," *Canadian Journal of Physics*, vol. 64, no. 9, pp. 1178–1183, 1986.

[98] J.-C. Krapez, "Thermal effusivity profile characterization from pulse photothermal data," *Journal of Applied Physics*, vol. 87, no. 9, p. 4514, 2000.

[99] C. Glorieux, R. Li Voti, J. Thoen, M. Bertolotti, and C. Sibilia, "Depth profiling of thermally inhomogeneous materials by neural network recognition of photothermal time domain data," *Journal of Applied Physics*, vol. 85, no. 10, pp. 7059–7063, 1999.

[100] J. V. Beck, B. Blackwell, and C. R. S. Clair Jr, *Inverse Heat Conduction: Ill-Posed Problems*. James Beck, 1985.

[101] M. Özışık and H. Orlande, *Inverse Heat Transfer: Fundamentals and Applications*. Taylor and Francis, New York, 2000.

[102] T. Theodoulidis and E. Kriezis, *Eddy Current Canonical Problems (with Applications to Nondestructive Evaluation)*. Tech Science Press, 2006.

[103] R. F. Harrington, *Field Computation by Moment Methods*. Wiley-IEEE Press, 1993.

[104] H. Stehfest, "Algorithm 368: Numerical inversion of Laplace transforms [D5]," *Communications of the ACM*, vol. 13, no. 1, pp. 47–49, 1970.

[105] H. Stehfest, "Remark on algorithm 368: Numerical inversion of Laplace transforms," *Communications of the ACM*, vol. 13, no. 10, p. 624, 1970.

[106] D. P. Gaver Jr, "Observing stochastic processes, and approximate transform inversion," *Operations Research*, vol. 14, no. 3, pp. 444–459, 1966.

[107] T. Weiland, "A discretization model for the solution of Maxwell's equations for six-component fields," *Archiv Elektronik und Uebertragungstechnik*, vol. 31, pp. 116–120, 1977.

[108] A. Ratsakou, C. Reboud, A. Skarlatos, and D. Lesselier, "Fast models dedicated to simulation of eddy current thermography," in *Electromagnetic Non-Destructive Evaluation* (D. Lesselier and C. Reboud, eds.), vol. 43, (Saclay, France), pp. 175–182, IOS Press, 2018.

[109] S. M. Shepard, "Advances in pulsed thermography," in *Thermosense XXIII* (A. E. Rozlosnik and R. B. Dinwiddie, eds.), vol. 4360, pp. 511 – 515, International Society for Optics and Photonics, SPIE, 2001.

[110] J. Canny, "A computational approach to edge detection," *IEEE Transactions on Pattern Analysis and Machine Intelligence*, vol. PAMI-8, no. 6, pp. 679–698, 1986.

[111] D.-J. Kroon, "Numerical Optimization of Kernel Based Image Derivatives," *Area*, no. December, 2009.

[112] N. Otsu, "A threshold selection method from gray-level histograms," *IEEE Transactions on Systems, Man, and Cybernetics*, vol. 9, no. 1, pp. 62–66, 1979.

[113] D. Sen and S. K. Pal, "Gradient histogram: Thresholding in a region of interest for edge detection," *Image and Vision Computing*, vol. 28, no. 4, pp. 677–695, 2010.

[114] A. S. Abutaleb, "Automatic thresholding of gray-level pictures using two-dimensional entropy," *Computer Vision, Graphics and Image Processing*, vol. 47, no. 1, pp. 22–32, 1989.

[115] R. Medina-Carnicer, R. Muñoz-Salinas, E. Yeguas-Bolivar, and L. Diaz-Mas, "A novel method to look for the hysteresis thresholds for the Canny edge detector," *Pattern Recognition*, vol. 44, no. 6, pp. 1201–1211, 2011.

[116] G. C. Onwubolu and B. Babu, *New Optimization Techniques in Engineering*, vol. 141. Springer, 2013.

[117] M. Minoux, *Mathematical Programming*. Wiley-Interscience Series in Discrete Mathematics and Optimization, Wiley-Interscience, New York, 1986.

[118] P. E. Gill, W. Murray, and M. H. Wright, *Practical Optimization*. Academic press, 1981.

[119] W. H. Press, S. A. Teukolsky, W. T. Vetterling, and B. P. Flannery, *Numerical Recipes 3rd Edition: The Art of Scientific Computing*. Cambridge University Press, 2007.

[120] R. Fletcher, *Practical Methods of Optimization*. John Wiley & Sons, 2013.

[121] W. C. Davidon, "Variable metric method for minimization," *SIAM Journal on Optimization*, vol. 1, no. 1, pp. 1–17, 1991.

[122] N. P. Avdelidis, C. Ibarra-Castanedo, X. Maldague, Z. P. Marioli-Riga, and D. P. Almond, "A thermographic comparison study for the assessment of composite patches," *Infrared Physics and Technology*, vol. 45, no. 4, pp. 291–299, 2004.

[123] J. Roche and D. Balageas, "Common tools for quantitative pulse and step-heating thermography-part ii: experimental validation," in *The 12th International Conference on Quantitative InfraRed Thermography (QIRT 2014)*, 2014.

[124] COMSOL AB, "Comsol multiphysics."

[125] D. L. Balageas, J.-M. M. Roche, F.-H. H. Leroy, W.-M. M. Liu, and A. M. Gorbach, "The thermographic signal reconstruction method: A powerful tool for the enhancement of transient thermographic images," *Biocybernetics and Biomedical Engineering*, vol. 35, no. 1, pp. 1–9, 2015.

[126] R. Miorelli, C. Reboud, T. Theodoulidis, N. Poulakis, and D. Lesselier, "Efficient modeling of ECT signals for realistic cracks in layered half-space," *IEEE Transactions on Magnetics*, vol. 49, no. 6, pp. 2886–2892, 2013.

[127] K. Pipis, A. Skarlatos, T. Theodoulidis, and D. Lesselier, "ECT-signal calculation of cracks near fastener holes using an integral equation formalism with dedicated Green's kernel," *IEEE Transactions on Magnetics*, vol. 52, no. 4, pp. 1–8, 2016.

ÉCOLE DOCTORALE
Sciences et technologies de l'information et de la communication (STIC)

Titre : Modélisation multi-physique de méthodes d'inspection par thermographie et imagerie rapide

Mots clés : Thermographie, Imagerie Multi-physique, Problèmes inverses, Contrôle non-destructif, Modélisation, Simulation

Résumé : L'inspection thermographique est une technique populaire de contrôle non destructif qui fournit des images de distributions de température sur de grandes étendues aux surfaces des pièces testées. Détecter les délaminations entre couches métalliques est le sujet ici. La simulation de ces inspections contribue en effet à compléter les études expérimentales, à évaluer les performances en termes de détection, et à être support d'algorithmes basés sur modèles. On se focalise sur un modèle semi-analytique basé sur un développement tronqué en fonctions propres par région. Le problème est résolu dans le domaine de Laplace en temps, et la distribution de température approximée par un développement sur une base produit tensoriel. Les sources considérées sont des lampes flash, mais aussi des sources courantes de Foucault. La description des délaminages sous forme de minces couches d'air se révèle équivalente à l'introduction d'une résistance superficielle au flux de chaleur permettant le traitement via l'approche modale. Des calculs complémentaires par des codes commercial (EFM) et interne (FIT) confirment l'exactitude. Puis une grande attention est donnée à l'imagerie et la détection. Une procédure en deux étapes est conçue: débruitage des signaux bruts et détection de tout éventuel défaut en utilisant une reconstruction de signal thermographique conduisant à une haute résolution spatiale et temporelle dans le plan transverse, complété par une détection de frontière, puis optimisation itérative, les résultats de la première étape étant utilisées pour la régularisation d'un schéma moindres carrés afin de caractériser épaisseurs et profondeurs. Tout ce qui précède est illustré par de nombreuses simulations numériques dans des conditions proches de l'application.

Title : Multi-physical modeling of thermographic inspection methods and fast imaging

Keywords : Thermography, Multi-physical imaging, Inverse problems, Nondestructive testing, Modeling, Simulation

Abstract : Thermographic inspection is a popular nondestructive testing (NdT) technique that provides images of temperature distribution over large areas at surfaces of tested workpieces. Detecting delaminations between metallic layers is the subject here. Simulation of these inspections complement experimental studies, evaluate performance in terms of detection and support model-based algorithms. A semi-analytical model based on a truncated region eigenfunction expansion for simulation of thermographic inspection is focused onto. The problem is solved in the Laplace time domain, and the temperature distribution approximated by expanding it on a tensor product basis. Considered sources are lamps providing thermal excitation but may also be eddy current sources. The description of the delaminations as thin air gaps between the workpiece layers proves to be equivalent with the introduction of surface resistance to the heat flow, enabling treatment via the applied modal approach. Complementary computations by commercial (FEM) and in-house (FIT) codes confirm the accuracy of the developments. Then, attention is paid on imaging and detection. A two-step procedure is devised, first denoising of raw signals and detecttion of possible defects using a thermographic signal reconstruction leading to high spatiotemporal resolution in the transverse plane, completed by proper edge detection, second the results of the first step are used for the regularization of a least-square scheme to characterize thicknesses and depths. All the above is illustrated by comprehensive numerical simulations in conditions close to practice.

Université Paris-Saclay
Espace Technologique / Immeuble Discovery
Route de l'Orme aux Merisiers RD 128 / 91190 Saint-Aubin, France